EFFECT OF COMPOSITION ON THE MAGNETIC AND ELASTIC PROPERTIES OF SHAPE MEMORY Ni-Mn-Ga

A Thesis

Presented in Partial Fulfillment of the Requirements for

the Degree Master of Science in the

Graduate School of The Ohio State University

By

Aayush Malla, B.E.

* * * * *

The Ohio State University

2003

Master's Examination Committee:

Dr. Marcelo J. Dapino, Adviser

Dr. Mark E. Walter

Approved by

———————————————

Adviser
Department of Mechanical
Engineering

ABSTRACT

The growing interest in ferromagnetic shape-memory Ni-Mn-Ga for implementation in actuator applications originates from the fact that this class of materials exhibits large strains when driven by a magnetic field. Large bidirectional strains up to a theoretical 6% are produced in these materials by twin boundary motion as martensite variants rotate to align respectively parallel or perpendicular to applied magnetic fields or stresses. These strains represent a significant improvement over piezoelectric and magnetostrictive materials. This thesis reports on experimental measurements conducted on Ni-Mn-Ga cylindrical rods subjected to uniaxial stresses and uniaxial magnetic fields which were applied collinearly along the magnetic easy axis direction of the rods. To this end, a test apparatus was developed which consists of a water-cooled solenoid actuator and a loading fixture. Despite the lack of a readily recognizable mechanism for reversible deformations, bidirectional strains as large as 6400 ppm (0.64%) were observed, or three times the saturation magnetostriction of Terfenol-D. The thesis presents room-temperature data on magnetization hysteresis, strain versus field and peak strain versus stress curves collected over a range of stresses between 0-65 MPa. From the latter set of curves, blocking force values are estimated as those for which the strain is 1% of the maximum strain (strain at zero-load). Additionally, the strain behavior under cyclic compressive stress at different DC field levels is explored from which the change in Young's modulus of elasticity is

discussed. A concise literature review is also included which discusses some models on martensitic variant rearrangement and the the subsequent development of magnetization and magneto-strain equations. The results illustrate the sensitivity of material behavior with respect to composition at different driving conditions and offer insight on the choice of material compositions at which maximum actuation performance is achieved.

ACKNOWLEDGMENTS

VITA

March 6, 1978 ....Born - Kathmandu, Nepal

2001 ....B.E. Mechanical Engineering, Indian
Institute of Technology

2001-present ....Graduate Reasearch Associate,
The Ohio State University.

PUBLICATIONS

Research Publications

A. Malla, M. Dapino, T. Lograsso, D. Schlagel, "Effect of Composition on the Magnetic and Elastic Properties of Shape-Memory Ni-Mn-Ga". *Proceedings of SPIE Smart Structures and Materials 2003*, Paper no.: 5053-29, Mar. 2003.

FIELDS OF STUDY

Major Field: Smart Materials and Structures

TABLE OF CONTENTS

Page

LIST OF TABLES

LIST OF FIGURES

CHAPTER 1

INTRODUCTION

1.1 Background

Extremely large magnetic field induced strain of 6% have been measured in ferro-magnetic shape memory alloys (FSMA's) in the nickel-manganese-gallium (Ni_2MnGa) system. Such strain represents an order of magnitude improvement over piezoelectric materials (0.1%) and magnetostrictive materials such as Terfenol-D (0.24%), and is the largest among all existing active materials. Despite their ferromagnetic properties, the strain generated by FSMA's does not originate from Joule magnetostriction, that is magnetic moment rotation, but is due to the reorientation of martensitic variants. Indeed, cooling below the characteristic martensite start temperature M_s produces a cubic to tetragonal transformation and a corresponding twin-variant structure. Over a certain compositional range, the martensite structure is tetragonal with c/a=0.94, thus the theoretical relative strain obtained from this structure is approximately 6%. The high temperature austenite Heusler phase exists over wide compositional ranges, centered on Ni_2MnGa, over which the magnetic properties and martensite transfor-mation temperature vary continuously. Furthermore, depending on the composition,

several different martensite structures have been reported. These variations in properties have been compiled onto the compositional map shown in Fig. 1.1,[10] which plots saturation magnetization, Curie temperature and martensite start temperatures. It has been speculated, based on a minimum saturation magnetization of 60 emu/g and martensite transformation temperatures above 300K, that compositions within the shaded region would exhibit the largest magnetic-field induced strains. Experimentally, alloys lying just to the right and above the shaded region have been found to exhibit the largest magnetic field-induced strains [10].
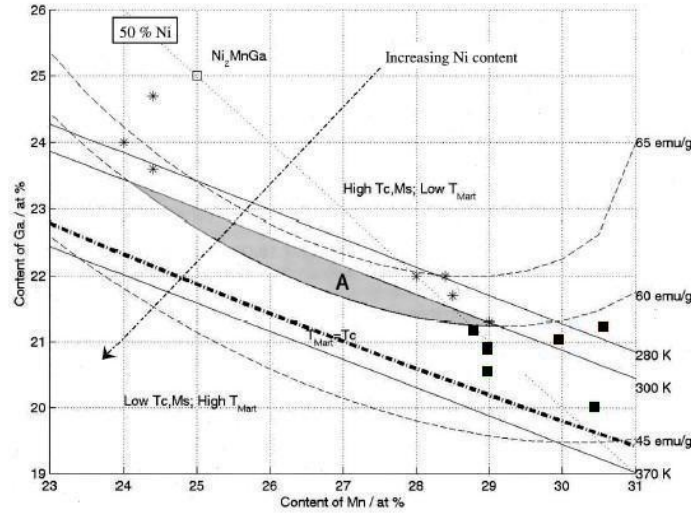
Figure 1.1: Compositional map for Ni-Mn-Ga ferromagnetic shape memory alloys, taken from Jin et al.[10]. The square symbols show the compositions examined in this thesis.

Either magnetic fields or stresses can be used to bias FSMA's toward one martensite variant or the other, which results in twin boundary motion and ensuing deformations as variants rotate to align respectively parallel or perpendicular to the field

2

or stress direction. Bidirectional deformations are obtained through field or stress rotation, or more typically, by driving these materials with an alternating uniaxial magnetic field oriented orthogonal to a fixed uniaxial stress as shown in Fig. 1.2(a). The significance of Ni_2MnGa for actuator applications lies in its broader bandwidth compared to conventional thermally activated shape memory materials. However, the orthogonal drive configuration required for bidirectional actuation dictates the use of electromagnets ("C" cores) for application of the magnetic field, thus leading to designs which are bulky, heavy and narrow band.

In this investigation, the response of alloys whose compositions are lower in Ga and higher in Mn than those believed to exhibit largest field-induced strains is experimentally studied and analyzed. More importantly, in the experiments presented here, a uniaxial stress and uniaxial magnetic field were applied *collinearly* along the magnetic easy axis direction of the samples, contrary to the conventional perpendicular arrangement, as illustrated in Fig. 1.2(b). Despite the lack of a readily recognizable mechanism for bidirectional twin boundary motion, reversible strains as large as 6380 ppm (0.64%) are demonstrated. These reversible field-induced strains are too large to result from Joule magnetostriction (typically only 250 ppm for these alloys) nor can they be explained by the existing martensite variant reorientation models. Furthermore, contrary to the conventional processing practice of material training through field cycling and thermal treatments, these large strains were observed in samples tested as cast. The significance of the experimental data presented in this paper is that a collinear drive configuration facilitates the use of solenoids for field actuation, as opposed to electromagnets as is conventionally the case (Fig. 1.2(a)). Solenoids

3

present several advantages over electromagnets including significantly reduced size and weight as well as broader frequency bandwidth.
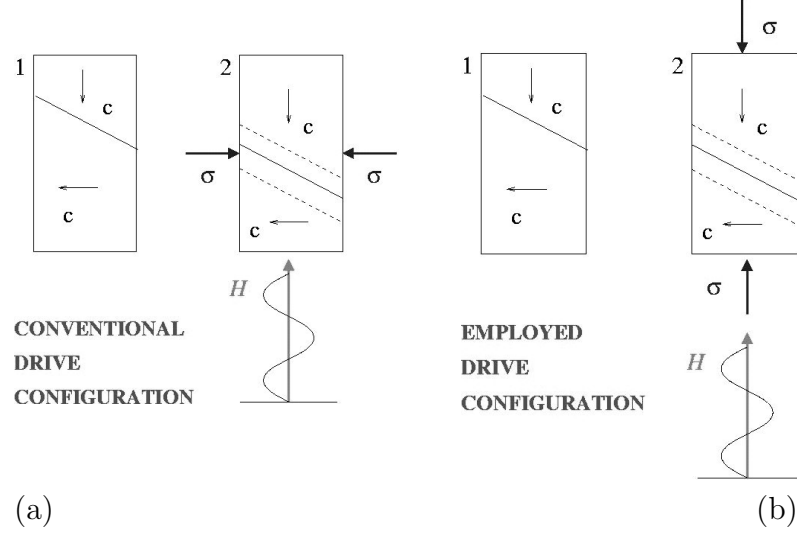
Figure 1.2: (a) Electromagnet-based drive configuration. (b) Solenoid-based drive configuration employed in the thesis.

Despite the small changes in composition between the alloys investigated here and those showing the largest magnetic field-induced strains, significant and profound differences are apparent between the two. It has been recently reported that the room temperature structure of the martensite phase at higher Mn content is orthorhombic (c/a=1.1) rather than tetragonal [19]. A second and perhaps more significant property of the samples investigated here is that the shape memory martensite transformation temperatures are nearly coincident with the ferromagnetic ordering temperature, suggesting a coupled magneto-structural transformation which may be responsible for the observed reversible strains. Coupled transitions, known to exist in rare-earth-silicon-germanium compounds [19], result in extraordinary magnetic responses including

large magnetostriction, where application of a magnetic field drives the structural change from a paramagnetic austenite phase to a ferromagnetic martensite phase. This structural change is fully reversible when the magnetic field is removed.

In order to gain a fundamental understanding and ultimately develop constitutive models of the magnetoelastic and thermoelastic behavior exhibited by these alloys, the dependence of the magnetic and physical properties on the composition and structural characteristics of the shape memory transformation must be elucidated. This investigation represents the first step toward that end. Attention is focused on the strain and magnetization behavior of alloys with varying parent material composition centered on $Ni_{49.56}Mn_{29.59}Ga_{20.85}$ under quasistatic fields of amplitude 8.1 kOe (650 kA/m). The ability of these alloys to produce mechanical work is evaluated through strain measurements at constant stress for a range of compressive stresses between 0-65 MPa, in which the upper limit is high enough to reduce the magnetic-induced strain to 1% of the free (unloaded) magnetic-induced strain. Dynamic experimental results presented in [5] involving broadband frequency response behavior in the dc-20 kHz range and elastic moduli calculations from resonant response under various bias fields, suggest the presence of a ΔE effect similar to that observed in Terfenol-D when Ni-Mn-Ga alloys are driven by a collinear magnetic field-stress pair. Furthermore, stiffness calculations shown in [5] suggest that solenoid-driven Ni-Mn-Ga alloys could exhibit significantly higher stiffness than those previously measured employing conventional electromagnet tests (30 GPa versus 7 GPa.)

1.2 Overview of Smart Materials

Active or "smart" materials constitute a class of materials that can react with a change in dimensional, electrical, elastic, magnetic, thermal or rheological properties to external stimuli such as heat, electric or magnetic field, stress and light. In most operating regimes, smart materials have the ability to recover the original shape and properties when the external driving input is removed which makes them suitable candidates for use in actuator and sensor applications. Smart materials can be broadly categorized into several classes based on the type of driving input and the phenomenon by which the response is produced: piezoelectric, electrostrictive, magnetostrictive, electrorheological and magnetorheological, shape memory, and ferromagnetic shape memory.

Piezoelectric materials are one of the most popular active materials. These materials produce mechanical strain (0.1%) [7] when voltage is applied across them (converse effect) and produce electric charge with the application of an applied surface strain (direct effect). This bidirectional energy transduction makes these materials attractive for actuation as well as sensing. Electrostrictive materials are similar to piezoelectric materials with slightly better strain capability but very sensitive to temperature. Unlike piezoelectric materials in which the strain and polarization are linearly related, electrostrictives generate strains which are proportional to the square of the polarization [2]. Electrorheological and magnetorheological fluids exhibit reversible changes in rheological properties (apparent viscosity, plasticity and elasticity) when respectively subjected to an electric or magnetic field. Upon application of either an electric or magnetic field, the micron sized particles become polarized and align themselves with the applied field resulting in a chain-like structure which limits the movement

of the fluid. These fluids have been extensively used in damping applications, and more recently, for actuation. Magnetostrictive materials generate strains as large as 0.24% [3] due to the alignment of magnetic domains along the direction of the applied magnetic field. Because magnetostriction is a material property, it does not degrade over time as can be the case with piezoelectric and electrostrictive materials which tend to depolarize when exposed to cyclic stresses or temperature changes.

Because FSMA's exhibit austenite-martensite phase transitions like shape memory alloys (SMA's), a detailed description of SMA's is provided next. A thorough discussion of FSMA's is provided in Section 1.4.

Shape memory alloys (SMA's) produce large reversible strains when subjected to heat and stress. These alloys can return to their original shape when the driving input is removed, thus behaving as though there were a "memory" of their original state. These materials undergo a phase transformation from a high temperature austenitic state to a low temperature martensitic state with the application of stress at which state the deformations occur. The materials then recover the original undeformed shape through the application of heat. The mechanism by which these materials strain is twin-boundary motion, as illustrated in Fig. 1.3.

The first discovery of shape memory effect was made in 1932 with gold-cadmium alloys and later with copper-zinc (brass) alloys in 1938. The interest in shape memory alloys increased tremendously after the discovery of a series of nickel titanium alloys by researchers at the Naval Ordinance Laboratory. Nitinol (**Ni**ckel **Ti**tanium-**N**aval **O**rdinance**L**aboratory) is one of the first shape memory alloys subjected to commercial applications. As aforementioned, heat and stress were subjected to bring out the
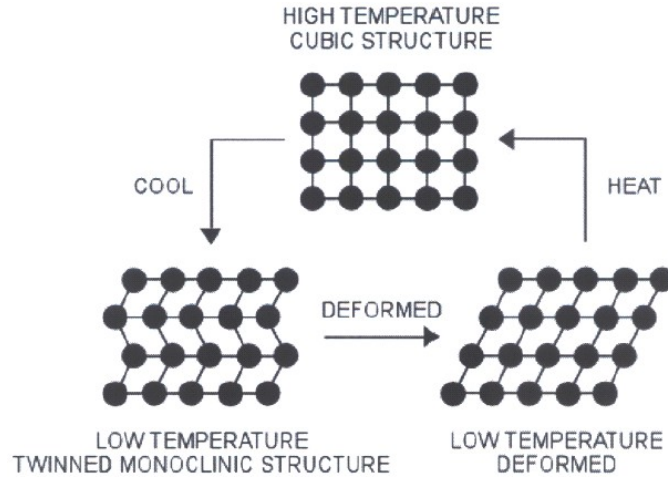
Figure 1.3: Phase transformation schematic.

shape memory effect in Nitinol. However, the fact that heating is carried out internally (electrically) which poses the problem of finite time required for shape change response, Nitinol could not find a wide use in applications demanding fast response and efficient driving methods.
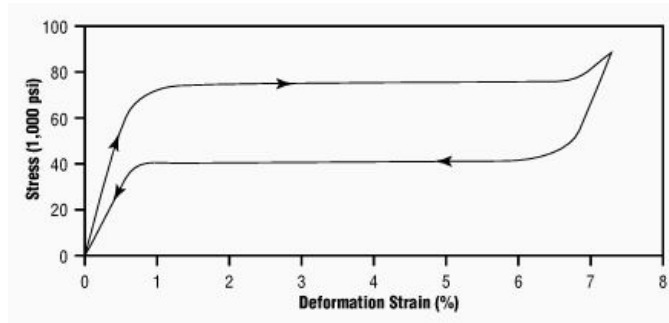
Figure 1.4: Typical loading and unloading behavior of superelastic NiTi.

All shape memory alloys exhibit appreciable hysteresis when subjected to a compressive stress or heat. There are four characteristic temperatures that play a role in the explanation of the austenite-martensite phase transformation through application of heat and thus, in the shape memory effect. These temperatures are illustrated in Fig. 1.5 for a typical shape memory alloy. The figure shows the volume fraction of martensite structure formed with the decrease in temperature. The austenite is the high temperature phase and the martensite is the low temperature phase. Upon heating the material in the martensite state, the austenite phase starts at A_s and is completed at temperature A_f. Similarly, cooling of the pure-austenite material leads to the start M_s and subsequent completion of the transformation at temperature M_f. It is noted that the transformation process exhibits significant hysteresis.
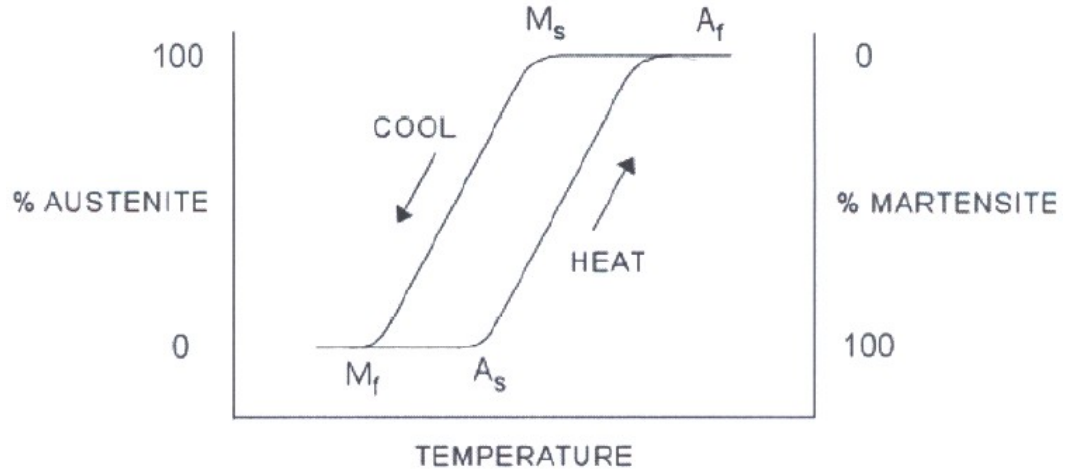
Figure 1.5: Phase transformation schematic showing the martensite volume fraction.

Fig. 1.6(a) shows the curve for strain produced against compressive stress for a shape memory alloy below M_f, i.e., when the material is completely in the martensitic

9

phase. There are two elastic regions, but a low elastic modulus region or a detwinning region exists in between, where large strain is produced. In this region, the material becomes very soft. The shape memory effect is concerned with the detwinning region where large reversible strains are possible when a suitable stress-field pair is employed.
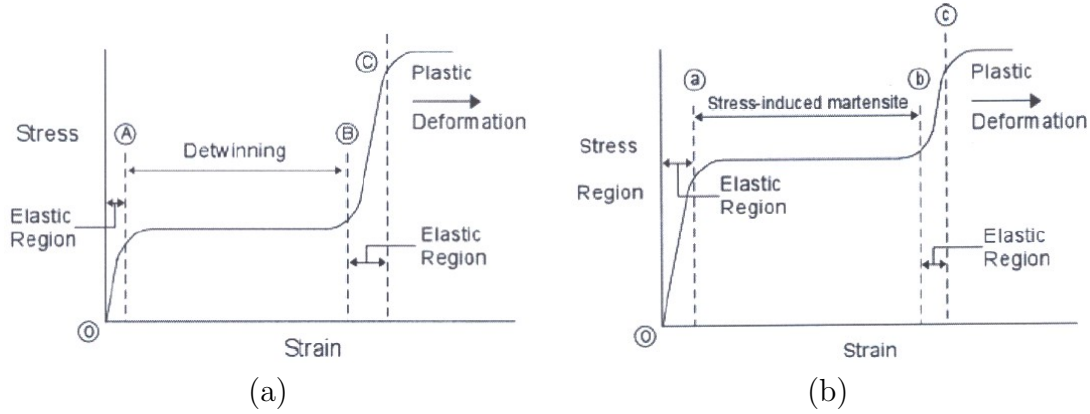
Figure 1.6: (a) Stress vs strain behavior in the martensite phase, below M_f and (b) stress vs strain behavior in the austenite phase, above A_f.

The martensite state can also exist at a temperature beyond A_f when enough stress is applied. Fig. 1.6(b) shows the nature of the strain produced through the application of compressive stress at a temperature above A_f. It is seen that a region of low modulus of elasticity exists, similar to the detwinning region in the martensite phase stress-strain curve. This region is known as the stress-induced martensite region, and in this region the material exhibits a martensitic behavior. This effect facilitates the use of SMA wires in applications in which the wires deform when stress is applied, that is they become soft in the stress induced martensite region, and spring

10

back to the original shape when heated, in which the material returns to the stiff high
temperature austenite phase.
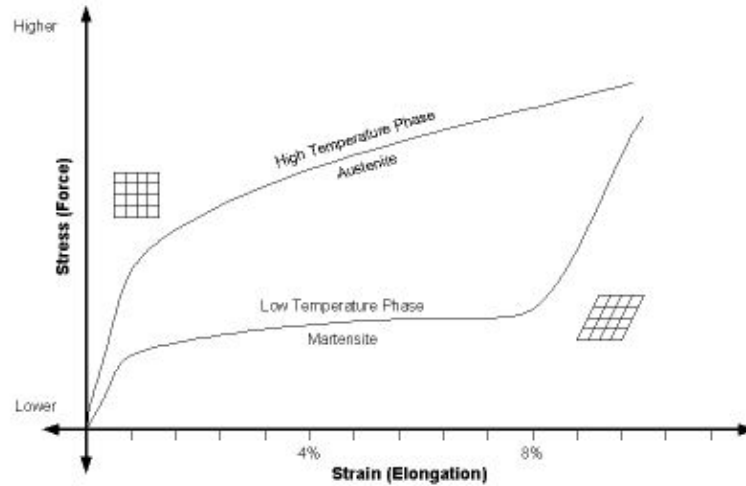
Figure 1.7: Comparison of the stress vs strain curve for the austenite and martensite
phases of a typical shape memory alloy.

1.3 Crystal Structure

Crystalline materials are made up of many atoms that are positioned in specific
arrays that define a unique crystal structure. The atomic arrays in crystals are de-
scribed with respect to a three dimensional net of straight lines the intersections of
which are points of a space lattice, i.e., a geometrical abstraction which is useful as a
reference in describing and correlating symmetry of physical crystals.

An important characteristic of a space lattice is that every point has identical
surroundings which means the grouping of lattice points about any given point is
identical to the grouping about any other point in the lattice. As illustrated in

11

Fig. 1.8 and Table 1.1, there are fourteen space lattices or fourteen different ways in which points can be configured in space so that each point has identical surroundings. The unit cell is used to specify a given arrangement of points in a space lattice with a set of coordinate axes chosen to have an origin at one of the lattice points.

System	Parameters	Interaxial angles
Triclinic	$a \neq b \neq c$	$\alpha \neq \beta \neq \gamma$
Monoclinic	$a \neq b \neq c$	$\alpha = \gamma = 90° \neq \beta$
Orthorhombic	$a \neq b \neq c$	$\alpha = \beta = \gamma = 90°$
Tetragonal	$a = b \neq c$	$\alpha = \beta = \gamma = 90°$
Cubic	$a = b = c$	$\alpha = \beta = \gamma = 90°$
Hexagonal	$a = b \neq c$	$\alpha = \beta = 90°, \gamma = 120°$
Rhombohedral	$a = b = c$	$\alpha = \beta = \gamma \neq 90°$

Table 1.1: The crystal systems [20].

The crystal system is defined using indices for planes and directions. Miller indices are used to define planes and a specific method exists for obtaining such indices. Indices for planes are put in round brackets and a family of equivalent planes is denoted by placing the indices within braces. For example, the set of cube faces can be represented as $\{100\}$ which represents the family $(100), (010), (001), (\bar{1}00), (0\bar{1}0), (00\bar{1})$, in which the bar above an index number represents the negative sign. The direction indices are denoted by placing them in square brackets and the family of such equivalent directions is represented by putting the indices in carets. Fig. 1.9 summarizes the steps to find the Miller indices for planes and the indices for directions.
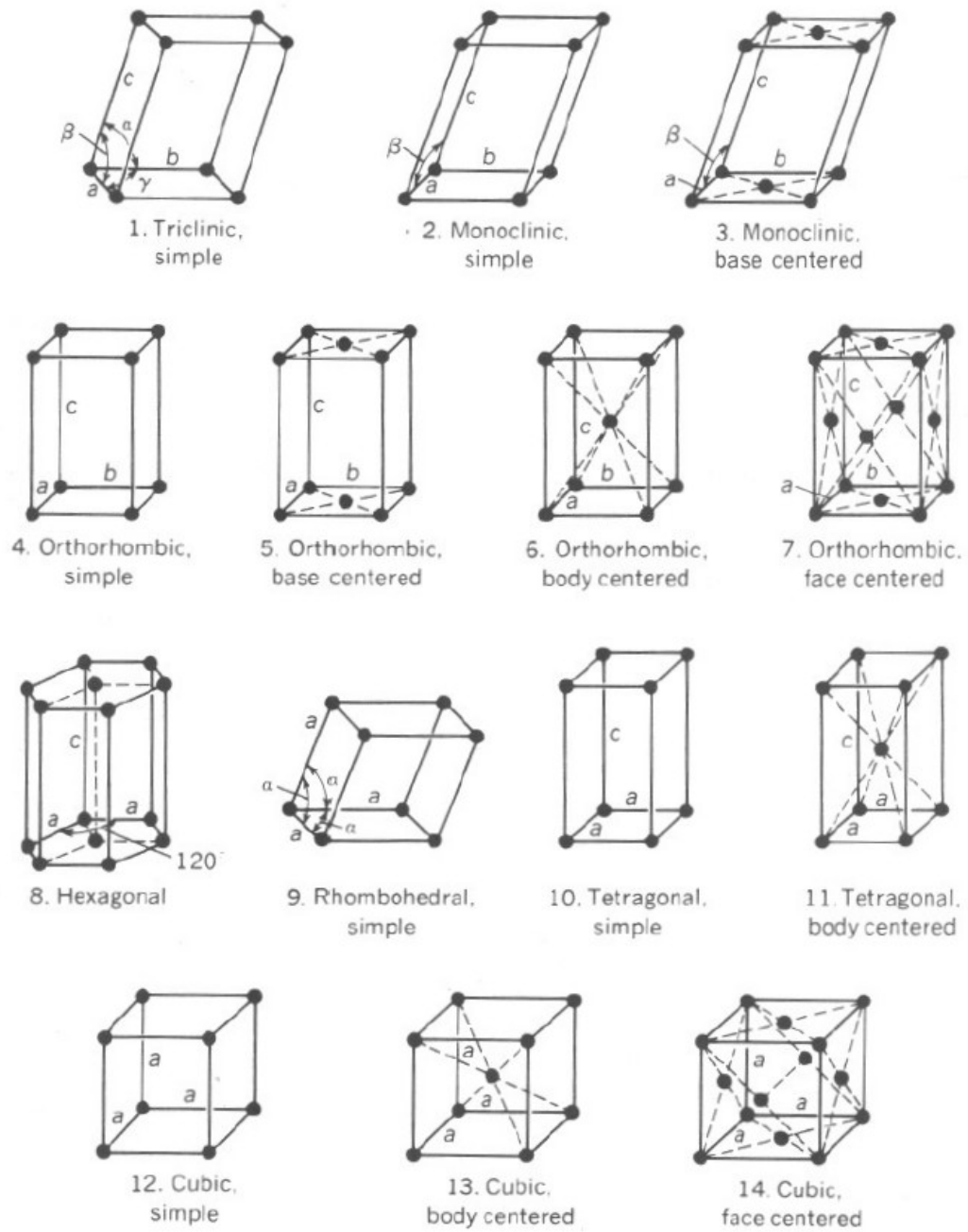
Figure 1.8: The fourteen Bravais lattices represented by their unit cells [20].
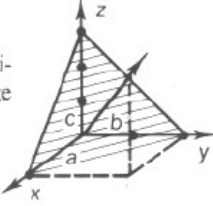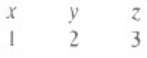
Procedure	Plane			Direction		
Intercept or projection on crystal axes (multiple or fraction of edge distance, i.e., lattice parameter)	x 1	y 2	z 3	x 1	y 2	z 3
Reciprocal of intercept	1	$\frac{1}{2}$	$\frac{1}{3}$		—	
Smallest integers with same ratio	6	3	2	1	2	3
Indices	(632) (Miller indices)			[123] (Direction indices)		
Generalized indices	(hkl)			$[uvw]$		
Indices of family or set of equivalents	$\{632\}$			$\langle 123 \rangle$		
Generalized indices	$\{hkl\}$			$\langle uvw \rangle$		

Figure 1.9: Summary for finding the indices for lattice planes and directions [20].

1.3.1 Magnetic Anisotropy

Materials can be anisotropic with respect to their electrical, magnetic, thermal, elastic or other properties, and most practical materials exhibit some degree of anisotropy. Now we focus the attention on magnetic anisotropy as it plays a fundamental role in the explanation of FSMA behavior. Every space lattice has a set of easy axes along which the magnetization is favored. This means that there are certain directions in the space lattice that are defined with respect to some coordinate axis origin, along which the magnetic domains become aligned when a magnetic field is applied. When a magnetic field is applied in a certain direction, the magnetic moments align along the easy axes that are closest to the direction of the applied magnetic field. The other directions along which the magnetic moments do not become aligned

as easily are known as the hard axes. The magnetization reaches its saturation value in a comparatively lower applied field along an easy axis as compared to the hard axis. This type of preference for certain axes to get magnetized more easily than the others is termed as the magnetic anisotropy which is equivalent to saying that the material does not have the same magnetic properties in all the different directions.

From Fig. 1.10(a)-(b), it is seen that $\langle 111 \rangle$ and $\langle 100 \rangle$ respectively are easy axes of magnetization of nickel and iron because the magnetization reaches the saturation value at lower magnetic field values for these axes. The energy associated with the magnetization along definite axes is known as the magnetic anisotropic energy. The magnetic anisotropy energy can be expressed in terms of the anisotropic constant K. A first approximation in writing the one-constant anisotropy equation for cubic
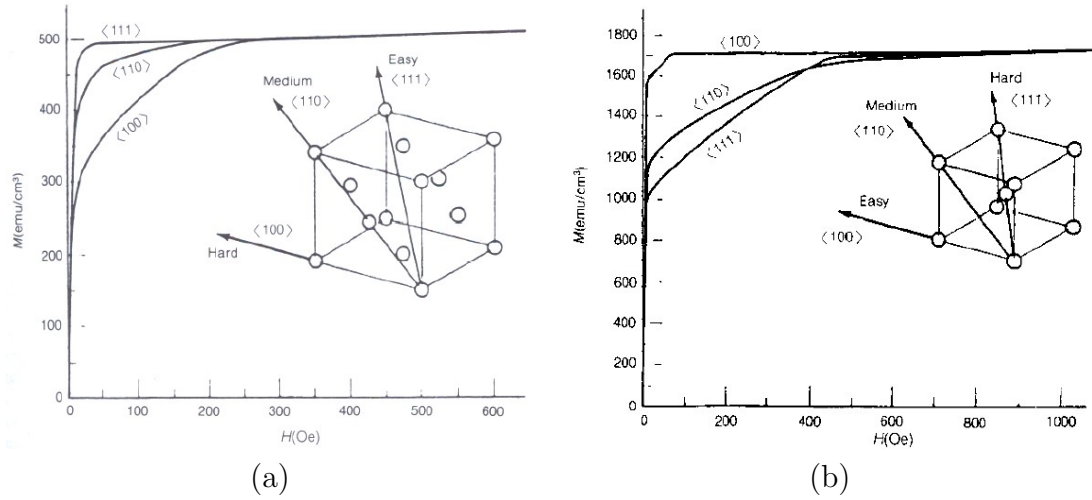
Figure 1.10: (a) Magnetization curves for nickel along the three axes $\langle 100 \rangle$, $\langle 110 \rangle$, $\langle 111 \rangle$. (b) Magnetization curves for iron along the three axes $\langle 100 \rangle$, $\langle 110 \rangle$, $\langle 111 \rangle$.

anisotropy can be expressed as

$$E_a = K_1(\cos^2\theta_1\cos^2\theta_2 + \cos^2\theta_2\cos^2\theta_3 + \cos^3\theta_3$$

where θ_1, θ_2, θ_3 are the angles which the magnetization makes relative to the three crystal axes.

1.4   Ferromagnetic Shape Memory Ni-Mn-Ga

The problem of slow thermally-induced phase transformation response exhibited by the nickel-titanium alloys has been addressed with the discovery of ferromagnetic shape memory alloys such as iron-palladium (Fe-Pd) and nickel-manganese-gallium (Ni-Mn-Ga). These compounds exhibit large strains as large as 6% [15]when activated by a magnetic field. The advantage of being driven by a magnetic field is that the response time is substantially reduced, thus enabling higher bandwidths than those possible through thermally-activated phase transformations. Ferromagnetic shape memory alloys have the potential to deform in different modes depending on the configuration of the magnetic field-stress pair. Although currently the emphasis is placed on the field-induced strain along the longitudinal axis of slender strips or rods, Fig. 1.11 shows the different modes of material deformation that are possible for these materials.

Ferromagnetic shape memory Ni_2MnGa has a cubic Heusler structure in the high temperature austenitic phase, as shown in Fig. 1.12(a). Upon cooling through the the martensite start temperature M_s, this alloy undergoes a cubic-to-tetragonal shape change as shown in Fig. 1.12(b). In Fig. 1.12, the Ga atoms are positioned at the corners and at the center of each face of the cubic lattice, the Mn atoms are located
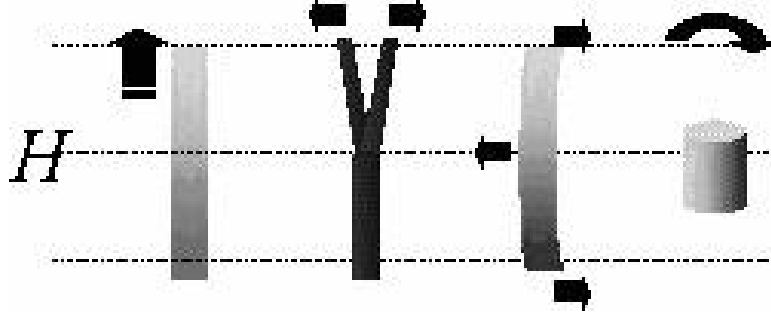
Figure 1.11: Possible forms of FSMA deformation.

at the midpoint of each edge and the Ni atoms are present at the body center of each of the four sub-cubic structures. At the martensite start temperature, the cubic lattice structure of the austenite phase contracts along the [100] direction and expands along the other two, as shown in Fig. 1.13. Cubic symmetry permits the formation of three tetragonal variants depending on which axis contracts. A typical martensitic microstructure consists of a mixture of these three variants in which two adjacent variants meet at one of the two possible well-defined interfaces called twin planes. While each of these variants has a unique orientation defined by its c-axis, which is the axis of symmetry, the martensitic phase is essentially a polycrystalline state composed of variable volume fractions of the three variants.

The ferromagnetic shape memory effect refers to either the reversible field-induced austenite-martensite transformation (as observed in Nitinol), or the rearrangement of martensitic variants by an applied field leading to an overall change of shape. As mentioned in Section 1.2, the Ni-Mn-Ga shape memory alloys are driven by magnetic fields at a martensitic state such that the latter phenomenon is favored. Each variant has a strong uniaxial magnetic anisotropy in which the easy axis is aligned with the
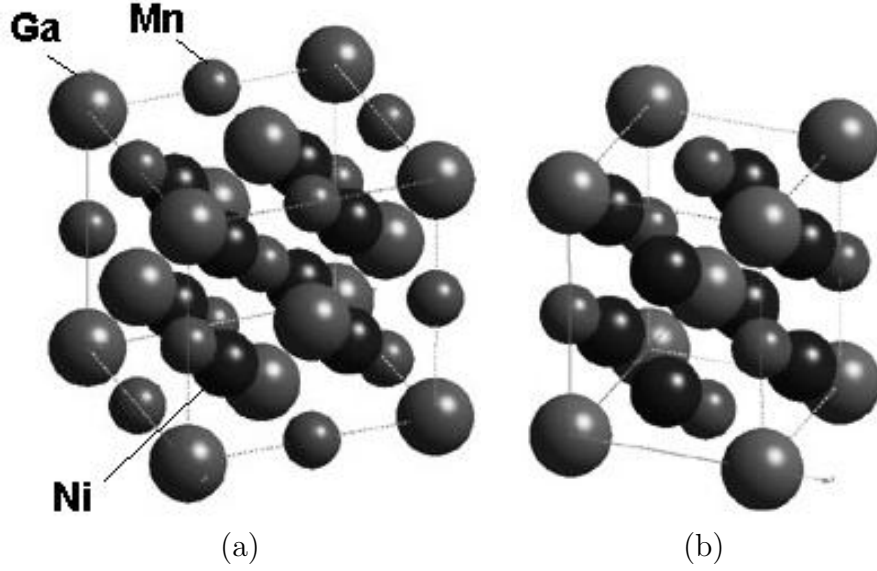
Figure 1.12: (a) Cubic Heusler structure of Ni_2MnGa in austenitic state and (b) Tetragonal martensitic variant structure.

c-axis and the easy axes of the neighboring twin bands are nearly perpendicular to each other. Therefore, an orthogonal magnetic field pair or an orthogonal magnetic field-stress pair can be used to bias the material toward one or another martensitic variant leading to large bidirectional deformations.

Fig. 1.14 shows the schematic of the field-induced rearrangement of the martensitic variants due to the action of a magnetic field. Before the application of the field, the variants have different magnetization directions perpendicular to one another. After the application of the field, the variant with initial magnetization direction parallel to the applied field direction grows at the expense of the other variant. This phenomenon is further illustrated in Fig. 2.14. The bar on the left represents a sample in zero field consisting entirely of single martensite twin variant (which may be formed through the application of an orthogonal compressive stress), with magnetization axis along the
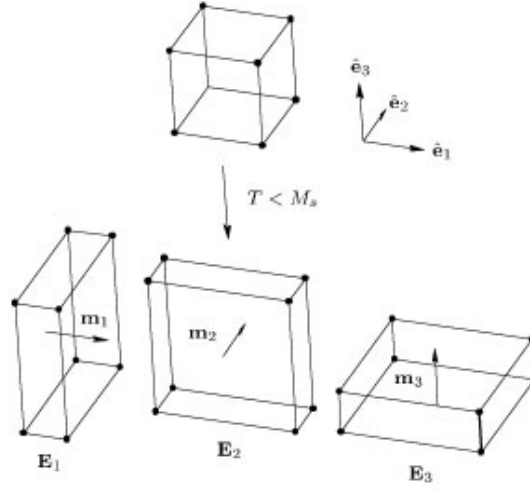
Figure 1.13: Tetragonal variant structures and associated magnetizations.

short white line and described by the grey region. As a transverse magnetic field H_1 is applied to the sample (middle), orthogonal twin variants with their magnetization axis in a preferential direction to H_1 start to appear, described by the dark colored region. When the field is further increased to H_2 (right), the preferentially oriented twins (dark) continue to grow at the expense of other twin variants (grey), resulting in an extension along the length of the material since the $a > c$.

1.5   Magnetism Fundamentals

The experimental setup and measurement techniques used in the course of the research heavily rely on the fundamentals of magnetism and ferromagnetic materials. The following sections will provide a basic review of the foundations of magnetism with relevance to the idea developed in the thesis.
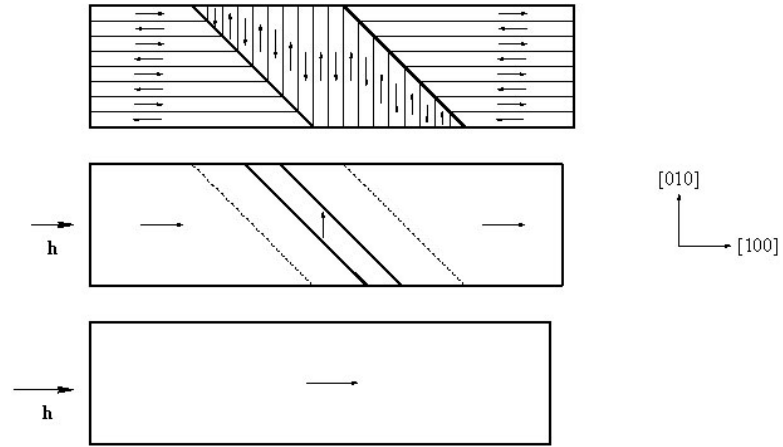
Figure 1.14: Schematic showing the increase of the favorable variant due to applied magnetic field.
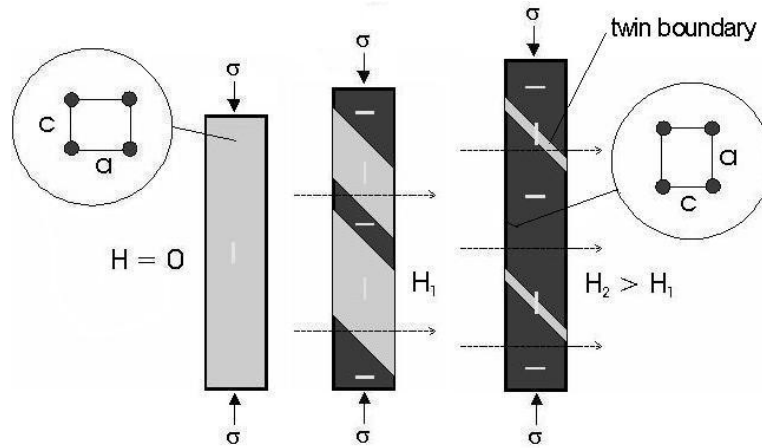
Figure 1.15: Increase of the favorable variant due to applied magnetic field and the change in the associated crystal orientation.

1.5.1 Magnetic Field

A magnetic field is produced by an electrical charge in motion. For this reason, current and magnetic field are closely related. The generation of a magnetic field in a volume of space changes the energy in the volume giving rise to an energy gradient which produces a force. The torque on a compass needle is one the most familiar effects of the force due to a magnetic field. Magnetic field is also produced by permanent magnets. The magnetic field produced by a permanent magnet is not due to electrical current but due to the permanent magnetization caused by the orbital motion and spin of the electrons in the magnet.

The magnetic field is a vector quantity which means it has a defined direction in addition to a magnitude. The direction of the magnetic field is shown in Fig. 1.16 for different wire arrangements and for a permanent magnet. The direction of a magnetic field is customarily defined by the right hand rule in which the thumb indicates the direction of current and the direction of the curl of the rest of the fingers gives the direction of the magnetic field.

1.5.2 Magnetic Field Intensity

The Biot-Savart law makes it possible to calculate the magnetic field intensity at a point generated by an electric field,

$$dvec{H} = \frac{1}{4\pi r^2} i d\vec{l} \times \vec{u}$$

where i is the current flowing in elemental length $d\vec{l}$ of a conductor, r is the radial distance, $\vec{u}$ is a unit vector along the radial direction towards the point where the field intensity is being calculated and $\vec{H}$ is the contribution to the magnetic field at a distance r to the current element $i\vec{l}$.
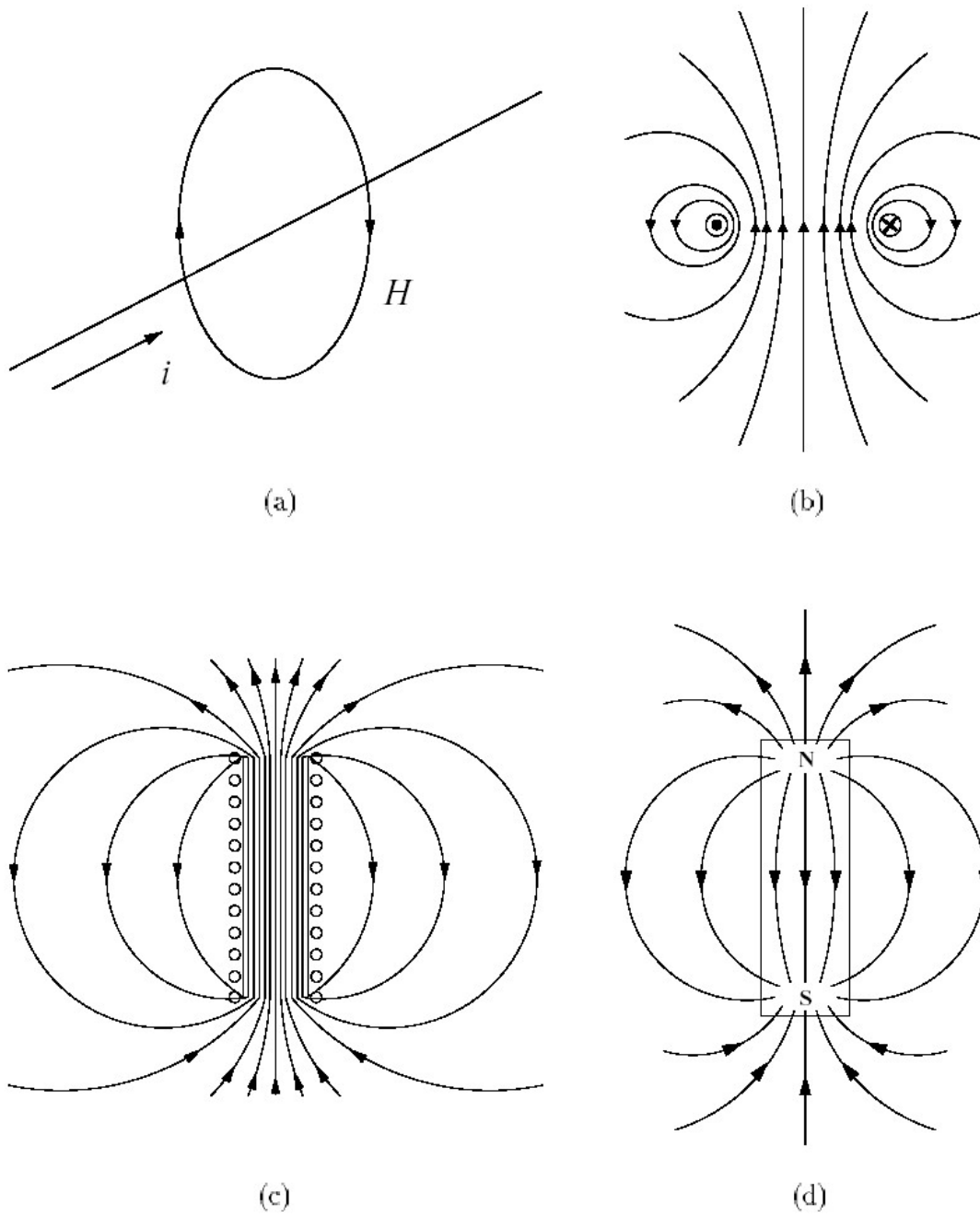
Figure 1.16: Magnetic field lines in a (a) straight conductor (b) singular circular loop (c) solenoid (d) permanent magnet [4].
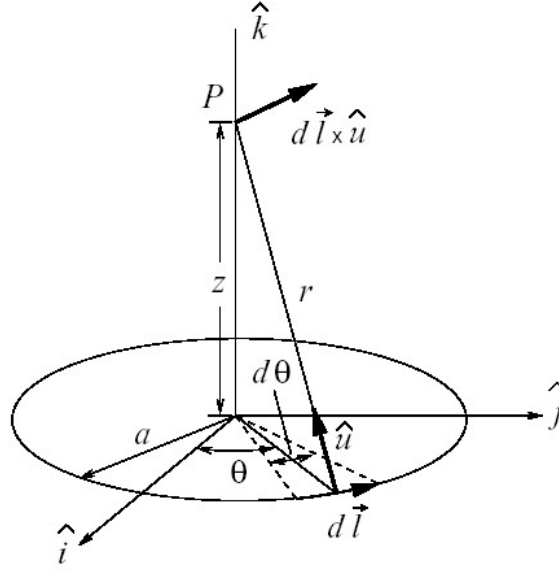
Figure 1.17: Magnetic field generated by a single circular coil showing the application of the Biot-Savart law [4].

The Biot-Savart law or equivalently, the Ampère law can be used to calculate the field intensities produced by coils in transducers as a part of a closed magnetic circuit. Fig. 1.17 shows the application of the Bio-Savart law to calculate the field intensity at a point on the axis of a circular current-carrying coil.

Magnetic field due to a thin solenoid of finite length

The magnetic field at a distance x from the center of a thin solenoid of finite length L, number of windings N, diameter D and carrying a current i is given by

$$H = \frac{Ni}{L} \left[\frac{(L + 2x)}{2\left[D^2 + (L + 2x)^2\right]^{1/2}} + \frac{(L - 2x)}{2\left[D^2 + (L - 2x)^2\right]^{1/2}} \right]$$

At the center of the solenoid $x=0$ and hence,

$$H = \frac{Ni}{L} \left[\frac{L}{\left[L^2 + D^2\right]^{1/2}} \right]$$

23

For an infinitely long solenoid, $L \gg D$ and $[L^2 + D^2]^{1/2} = L$. So,

$$H = \frac{Ni}{L} = ni$$

The fields generated by solenoids are dipole fields.

Magnetic field due to a thick solenoid of finite length

Thick solenoid coils of short length and greater number of turns are used in actuators to produce high field strength. Thick solenoids are used in applications that require higher field strength with lower current flowing through the coils. In the case of thick solenoids, the inner and outer radii are distinct and , therefore, the calculation of the magnetic field is not as straightforward as for thin ones.

If L be the length of the solenoid, r_1 the radius of the inner windings and r_2 the radius of the outer windings, then two parameters α and β can be defined describing the geometrical properties of the solenoid.

$$\alpha = \frac{r_2}{r_1} \tag{1.1}$$

$$\beta = \frac{L}{2r_1} \tag{1.2}$$

The field generated by such a thick solenoid is then a function of α, β and the coil current i. The magnetic field intensity at the center of the solenoid was given by Montgomery [14],

$$H_o = F(\alpha, \beta) f(i, r_1, r_1) \tag{1.3}$$

where $F(\alpha, \beta)$ and $f(i, r_1, r_1)$ are known as the field factor and the current factor and are given by

$$F(\alpha, \beta) = \beta \left[arcsinh(\alpha/\beta) - arcsinh(1/\beta) \right] \tag{1.4}$$

$$f(i, r_1, r_1) = \frac{Ni}{L} \frac{r_1}{r_2 - r_1} \tag{1.5}$$

24

The expression for the magnetic field can also be written in a slightly different but equivalent form as

$$H_o = \frac{Ni}{r_1} \frac{F(\alpha, \beta)}{2\beta(\alpha - 1)}$$

All of the above equations for the magnetic field are very general and can be shown to simplify to a more familiar expression in the limiting case $r_1 = r_2$ when

$$H_o = Ni \frac{1}{(4r^2 + L^2)^{1/2}}$$

so that when $L \to 0$, $H_o \to Ni/2r$ and as $L \to \infty$, $H_o \to Ni/2L$.

1.5.3   Magnetic Induction and Magnetic Flux

Magnetic induction or magnetic flux density $\vec{B}$ is a vector quantity that signifies the response of a medium to the applied magnetic field $\vec{H}$. All media respond to a magnetic field with some induction. This response can be quantified with the introduction of a quantity known as permeability μ which is dependant on the type of medium. Hence, one of the most used relation in magnetism follows,

$$\vec{B} = \mu \vec{H} \tag{1.6}$$

However, permeability is not a constant quantity in most ferromagnetic media but a multi-valued entity dependant on the intensity of the field as well as on stress and temperature regimes. Therefore, a similar quantity known as the differential permeability is more often used for calculation purposes which is given by

$$\mu' = \frac{dB}{dH} \tag{1.7}$$

The permeability of any medium is expressed in terms of the permeability of free space μ_o which has a value of $4\pi \times 10^{-7}$H/m. Hence, the relative permeability is given

by

$$\mu_r = \frac{\mu}{\mu_o} \tag{1.8}$$

The magnetic flux density can also be defined as the magnetic flux $\vec{\phi}$ passing through a unit area of the medium and the magnetic flux crossing a differential area can be defined by

$$\vec{\phi} = \int_S \vec{B} dS$$

Since magnetic induction is also the flux density, it can be defined by the following relation,

$$B = \frac{\phi}{A} \tag{1.9}$$

where A is the cross sectional area of the medium through which the magnetic flux lines are passing.

1.5.4 Electromagnetic Induction

Electromagnetic induction is the phenomenon by which electromotive force is induced when the magnetic flux linking an electrical circuit changes. Faraday and Lenz were the early two investigators of this effect and there are two laws of electromagnetic induction as a consequence of their work. Faraday showed that the voltage induced in an electrical circuit is proportional to the rate of change of magnetic flux linking the circuit. Lenz's law states that the induced voltage is in a direction which opposes the change of flux producing it.

The two fundamental laws of electromagnetic induction allow the calculation of the magnetic induction in a medium. The induced e.m.f. due a changing flux in a coil is given as

$$V = -N\frac{d\phi}{dt} \tag{1.10}$$

26

where N is the number of turns of the coil. From equations (1.9) and (1.10), the following result follows

$$V = -NA\frac{dB}{dt}$$

which can be written to get the more useful relation

$$B = -\frac{1}{NA}\int V\,dt \tag{1.11}$$

This is the general equation used for measuring the magnetic flux density of a medium due to the change in magnetic flux passing through it and forms the basis for stationary sensing coil measurements for magnetic induction.

1.5.5 Magnetic Dipole and Magnetic Moment

In magnetism, magnetic dipole is equivalent to electric dipole in electricity. Magnetic dipole generates a magnetic dipole moment in a current loop of area A carrying current i which is given by $m = iA$. The torque on a magnetic dipole of moment m in a magnetic induction B is given by,

$$\vec{\tau} = \vec{m} \times \vec{B}$$

and in free space the above equation reduces to,

$$\vec{\tau} = \mu_o\vec{m} \times \vec{H}$$

This means that the magnetic induction $\vec{B}$ tries to align the dipole so that the magnetic moment $\vec{m}$ lies parallel to the induction or alternatively, it can be considered that $\vec{B}$ tries to align the current loop so that the field produced by the current loop is parallel to it. The energy of the dipole moment $\vec{m}$ in the presence of magnetic

induction $\vec{B}$ assuming no frictional losses will be,

$$E = -\vec{m} \cdot \vec{B}$$

which gives the following result in free space

$$\vec{\tau} = \mu_o \vec{m} \times \vec{H}$$

The magnetic dipole moment can be thought of as a moment created due to two hypothetical magnetic poles of dipole strength p that are separated by a distance l and is expressed as,

$$\vec{m} = pl$$

In the Sommerfeld convention, the pole strength is defined in terms of the magnetic flux Φ emanating from a single magnetic pole and is given by $p = \Phi / \mu_o$.

1.5.6 Magnetization

The magnetization of a medium is defined as the magnetic moment developed per unit volume. It is generated due to the resultant (uncompensated) spin and orbital angular momentum of the electrons within the solid.

$$\vec{M} = \frac{\vec{m}}{V}$$

Taking the simple case of a bar magnet with magnetic flux $\vec{\Phi}$ at the center and, dipole length l and cross sectional area A, the magnetic moment $\vec{m}$ is given by $\vec{m} = \vec{\Phi} l / \mu_o$. The magnetization can then be expressed in the form

$$
\begin{aligned}
\vec{M} &= \frac{\vec{\Phi}}{\mu_o A} \\
&= \frac{\vec{B}}{\mu_o}
\end{aligned}
\tag{1.12}
$$

28

The above relation is valid only in the case where there are no conventional electric currents present to generate an external magnetic field and so $\vec{B}=\mu_o\vec{M}$. It is seen that the total magnetic induction is comprised of the contribution from the both magnetic field $\vec{H}$ and magnetization $\vec{M}$.

It is useful to define one more term known as the technical saturation magnetization M_s and complete saturation magnetization M_o. If a material has n magnetic dipoles per unit volume of magnetic moment m, then the magnetic moment per unit volume of the material when all the moments are aligned parallel is termed the saturation magnetization M_o which is equal to the product of n and m. There is a good distinction between the technical saturation magnetization and the complete saturation magnetization. In brief, it can be stated that technical saturation magnetization is achieved when the material is converted to a single magnetic domain, however, at higher magnetic fields, the magnetization increases gradually beyond the technical saturation value which results due to the spontaneous magnetization within a single domain and this is known as forced magnetization or complete magnetization.

1.5.7   Relation between B, H and M

The magnetic induction in a medium is due to the combined effect of the applied magnetic field and magnetization and the relation is defined as a vector sum of these as follows,

$$\vec{B} = \mu_o(\vec{H} + \vec{M}) \tag{1.13}$$

The above equation relating the three basic magnetic quantities is true under all circumstances.

1.5.8 Permeability and Susceptibility

The permeability of a medium signifies the magnitude of magnetic induction developed per unit magnetic field applied. The relation can be defined by,

$$\mu = \frac{B}{H} \tag{1.14}$$

which follows from equation 1.6.

The susceptibility is defined as the magnitude of magnetization generated per unit magnetic field applied and is given by,

$$\chi = \frac{M}{H} \tag{1.15}$$

Like permeability μ, susceptibility χ is not a constant quantity since M is a non-linear function of the field in most cases and the more useful quantity differential susceptibility may be expressed as,

$$\chi' = \frac{dM}{dH}$$

From equations (1.8), (1.13) and (1.15), we arrive at the following relation between susceptibility and relative permeability.

$$\mu_r = \chi + 1$$

1.5.9 Piezomagnetic Coefficient

The piezomagnetic coefficient in shape memory alloys is equivalent to the piezo-electric coefficient in piezoelectric materials. In piezoelectric materials, it quantifies the magnitude of strain produced in a certain direction per unit electric field applied in the same direction or in two other perpendicular directions when external stresses

on the material are constant. The converse effect in piezoelectric materials is the generation of strain due to the combined effect of external stress and electric field and the direct effect is the generation of charge due to the same two inputs. The converse and direct effects in piezoelectric materials can be represented by,

$$S_i = (s_{ij})_E T_j + (d_{im})_T E_m \tag{1.16}$$

where S_i is the total strain produced in direction i, $(s_{ij})_E$ is the strain produced in direction i due to stress in direction j at constant electric field, T_j is the applied stress in direction j, $(d_{im})_T$ is the strain produced in direction i due to the electric field applied in direction m and E_m is the electric field applied in direction m.

$$D_m = (q_{mi})_E T_i + (\varepsilon_{mk})_T E_k \tag{1.17}$$

where D_m is the total charge produced in direction m, $(q_{mi})_E$ is the charge produced in direction m due to stress in direction i at constant electric field, T_i is the applied stress in direction i, $(\varepsilon_{mk})_T$ is the charge produced in direction m due to the electric field applied in direction k and E_k is the electric field applied in direction k.

In the case of shape memory alloys, there is no direct effect and only the converse effect is present. The piezomagnetic coefficient $(d_{im})_T$ in shape memory effect can be defined as the strain produced in direction i per unit magnetic field applied in direction m at constant external stress. The total strain in shape memory alloys subjected to a stress and magnetic field is expressed in the same way as that for piezoelectric materials except that the magnetic field term replaces the electric field term in equation (1.18). The total strain may be expressed as,

$$S_i = (s_{ij})_E T_j + (d_{im})_T H_m \tag{1.18}$$

where H_m is the magnetic field intensity applied in direction m and $(d_{im})_T$ is the associated piezomagnetic coefficient. The piezomagnetic coefficient is simply the slope of the strain versus magnetic field curve and may have different values for increasing and decreasing fields and can be mathematically expressed as,

$$d_{im} = \frac{\partial e_i}{\partial H_m} \qquad (1.19)$$

1.5.10 Magnetic Hysteresis and Anhysteretic Magnetization

Hysteresis is a non-linear property of magnetic materials and is the irreversibility of a magnetic state of a material that is induced by an applied magnetic field so that the material does not show the same behavior in a complete cycle of increasing and decreasing fields. The result is a sigmoid shaped hysteresis loop that encloses a certain area in the plot. The magnetic state of a magnetic material due to the applied magnetic field is quantified by the magnitude of the magnetic induction in the material. The magnetic induction value is not the same at the same magnetic field for one complete cycle of increasing and decreasing fields. Fig. 1.18(a) shows the magnetic hysteresis loop of a typical ferromagnetic material.

Different parameters are used to characterize hysteresis curves. The complete saturation magnetization as mentioned in Section 1.5.6, M_o gives the upper limit to the magnetization that can be achieved but at temperatures well below the Curie temperature, the technical saturation can be used. When a previously unmagnetized ferromagnetic material is subjected to a magnetic field, the magnetic induction increases in a non-linear manner with the applied field. When the field is decreased, the induction does not follow the same path that it had for the increasing field, the latter value of induction being greater in magnitude for the same magnitude of the applied
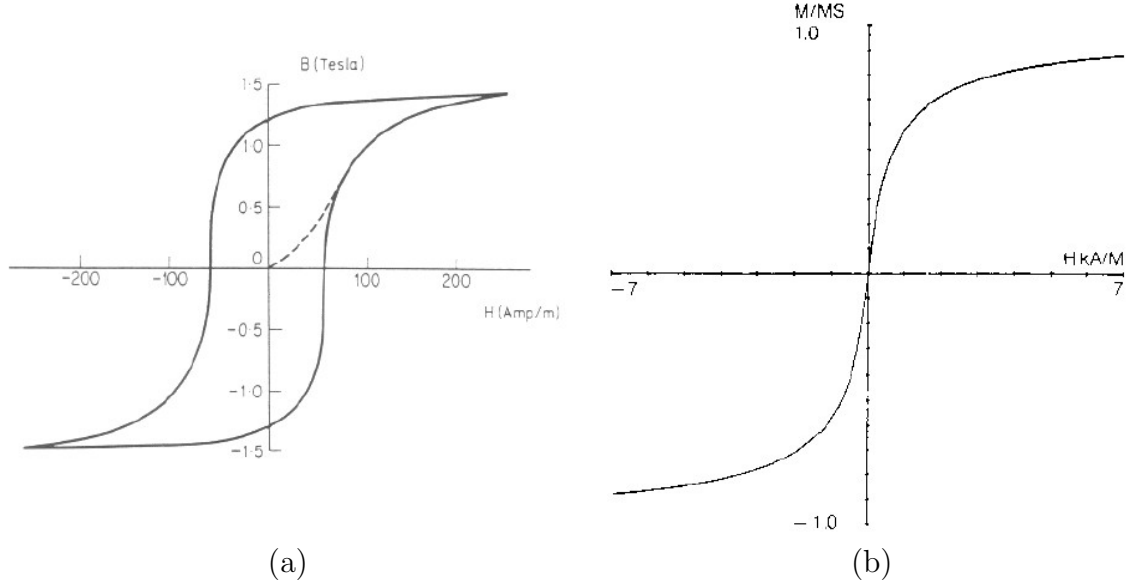
Figure 1.18: (a) A typical hysteresis loop of a ferromagnetic material (b) Anhysteretic magnetization curve [8].

field. This results in a hysteresis loop and the area enclosed by such a loop represents the energy loss due to the irreversible magnetic states induced in the material. From the hysteresis curves of ferromagnetic materials, it is seen that there is always a remanent induction B_r that remains in the material even when the magnetic field is completely removed. The remanent induction is of the same magnitude in both increasing and decreasing fields. Using equation (1.13) for $H=0$,

$$B_r = \mu_o M_r \tag{1.20}$$

where M_r is the remanent magnetization.

There is a distinction between the terms remanence and remanent induction or magnetization. Remanence is the value of either the remaining induction or magnetization when the field has been removed after the magnetic material has been magnetized to saturation whereas remanent induction or magnetization is the remaining induction or magnetization value when the field has been removed after magnetizing to an arbitrary level. The remanence is , therefore, the upper limit for all remanent inductions or magnetizations.

Material	$(\mu_r)_{max}$	B_s(T)	H_c(A/m)	W_H(J/m^3)
Purified iron	180000	2.15	4	30
Iron	5000	2.15	80	500
Iron(4%Si)	7000	1.97	40	350
45 Permalloy	25000	1.6	24	120
Hipernik	70000	1.6	4	22
78 Permalloy	100000	1.07	4	20
Permendur	5000	2.45	160	1200
2V Permendur	4500	2.4	160	600

Table 1.2: Magnetic properties of high-permeability ferromagnetic materials [8].

Another important parameter is the coercivity or the coercive field H_c which is the reverse field that has to be applied to reduce the magnetization to zero and is strongly dependant on the condition of the sample such as heat treatment or deformation. Like remanence, there is a distinction between coercivity and coercive field. The former is used to describe the magnetic field required to reduce the magnetization to zero from saturation and the latter describes the magnetic field needed to reduce the magnetization to zero from an arbitrary level. The coercivity becomes an upper limit for all values of coercive fields. Table 1.2 shows some parameters that can be

extracted from hysteresis loops of selected ferromagnetic materials where B_s and W_H are the saturation magnetic induction and hysteresis loss respectively.

The suitability of ferromagnetic materials for applications is determined principally from characteristics shown by their hysteresis loops. Hysteresis loops are carefully studied in the design of transformers and electromagnets. Broadly speaking, there are two reasons for the generation of hysteresis. Imperfections in the form of dislocations or impurity elements in a material cause an increase in energy loss during magnetization process due to a kind of internal friction which gives rise to hysteresis. Magneto-crystalline anisotropy is another mechanism that gives rise to hysteresis. In anisotropic solids, certain crystallographic axes are favored by the magnetic moments which prefer to align in these directions leading to a lower energy state. The magnetic moments can be dislodged from their original direction by application of a magnetic field which makes them jump to crystallographically equivalent axes that are closer to the field direction and of lower energy. This results in discontinuous and irreversible rotation of the magnetic moments which leads to a kind of switching action. If the hypothesis that hysteresis is caused by the imperfections is accepted then a material without imperfections and dislocations would develop a magnetic induction that would be a single valued function of the magnetic field and the magnetization curve would be reversible as shown in Fig. 1.18(b). The FEMM3.2 software uses anhysteretic magnetization data for finite element simulations.

1.5.11 Demagnetizing Field and Field Correction

The fact that the magnetization M and the magnetic field H point in opposite directions inside a magnetized material of finite dimensions, due to the magnetic

dipole moment, a demagnetizing field H_d may be defined whenever magnetic poles are created in a material. The demagnetizing field may be detected during hysteresis measurements on finite length samples when the applied field is reduced to zero but the measured field is negative due to remanent magnetization.

Geometry	Aspect ratio (l/d)	Demagnetization factor (N_d)
Toroid	-	0
Long cylinder	-	0
Cylinder	20	0.00617
Cylinder	10	0.0172
Cylinder	8	0.02
Cylinder	5	0.04
Cylinder	1	0.27
Sphere	-	0.333

Table 1.3: Demagnetization factors for various sample geometries [8].

Fig. 1.19 shows the demagnetization effects in a bar magnet. A point should be made that the magnetic field and induction lines are identical outside the material but inside they are quite different and even point in opposite directions. The demagnetizing field depends only on the magnetization in the material(pole strength) and the shape of the specimen (pole separation determined by sample geometry). The following expression can be given for the demagnetizing field

$$H_d = N_d M$$

where N_d is the demagnetization factor that is calculated solely from the sample geometry and is a dimensionless quantity if M and H are measured in A/m.

The magnitude of internal magnetic field experienced by the specimen is always less than the applied external field due to the demagnetization field that arises The
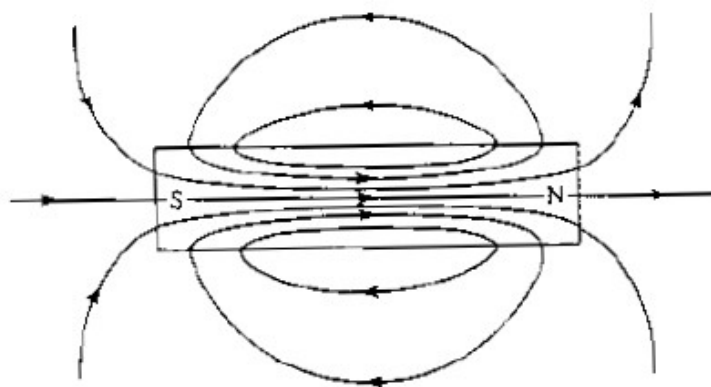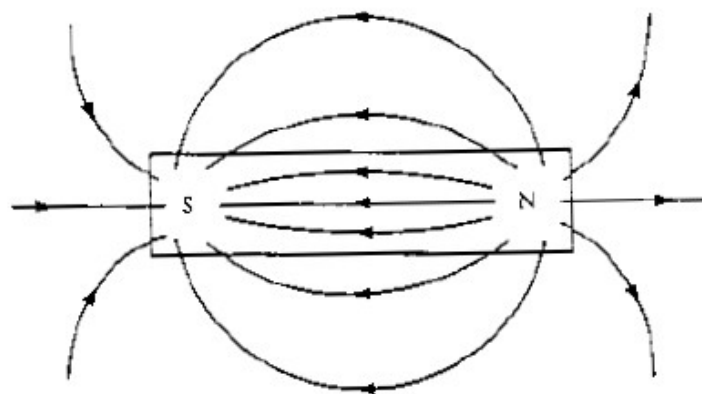
Figure 1.19: Magnetic field H both inside and outside a bar magnet as shown in the top and magnetic induction B both inside and outside a bar magnet [8].

correction for the demagnetization field is achieved as follows,

$$H_{in} = H_{app} - N_d M$$

1.5.12   Eddy Currents

Eddy currents are local currents generated due to any time varying flux in the core of the material which also contribute to the non linearity of the B-H curve. Due to the time varying flux in the material, a voltage is induced and resulting in a current flow which is dependant on the resistivity of the material. Eddy currents dissipate energy in the form of heat which results in an energy loss from the system.Eddy currents are reduced by selecting high resistivity core materials or by laminating the core, introducing tiny, discontinuous air gaps between core gaps. Eddy currents may not be a pose a problem of energy loss for magnetostatic analysis but even for quite low frequencies of varying flux, the effect may be significant.

1.5.13   Units in Magnetism

There are three different units currently used in magnetism and several other which are derivatives of these three. The three units are the Gaussian or CGS system and two MKS unit systems, the Sommerfield convention and the Kennelly convention. The following table summarizes the units of the most common magnetic quantities.

Further, the following important conversion factors are always used with field and induction calculations.

$$1 \text{ Oersted} = (1000/4\pi) \text{ A/m} = 79.58 \text{ A/m}$$

$$1 \text{ Gauss} = 10^{-4} \text{ Tesla}$$

$$1 \text{ emu/cm}^3 = 1000 \text{ A/m}$$

Quantity	Symbol	SI (Sommerfield)	SI (Kennelly)	EMU (Gaussian)
Field	H	A/m	A/m	oersteds
Induction	B	Tesla	Tesla	Gauss
Magnetization of magnetization	M	A/m	-	emu/cc
Intensity	I	-	Tesla	-
Flux	ϕ	Weber	Weber	Maxwell
Moment	m	Am^2	Weber meter	emu
Pole strength	p	Am	Weber	emu/cm
Field equation	-	$B = \mu_o(H + M)$	$B = \mu_o H + I$	$B = H + 4\pi M$
Energy of moment (in free space)	-	$E = -\mu_o m H$	$E = -mH$	$E = mH$
Torque on moment (in free space)	-	$\tau = \mu_o m \times H$	$E = m \times H$	$E = m \times H$

Table 1.4: Principal unit systems currently used in magnetism [8].

1.5.14 Maxwell's Equations

The differential forms of the laws of electromagnetics are known as Maxwell's equations (1831-1879). These laws are the consequences of the work of Gauss, Ampere and Faraday. Maxwell's own contribution lies in the concept of displacement currents which can be realized in the high frequency domain of the electromagnetic wave propagation in materials. Maxwell's equations may be summarized as follows:

$$\nabla \cdot \vec{B} = 0 \qquad \text{(Conservation of flux)}$$

$$\nabla \cdot \vec{D} = q \qquad \text{(Gauss law for electric flux)}$$

$$\nabla \times \vec{H} = \vec{J} + \frac{\partial \vec{D}}{\partial t} \qquad \text{(Maxwell's generalization of Ampère's law)}$$

$$\nabla \times \vec{E} = -\frac{\partial \vec{B}}{\partial t} \qquad \text{(Faraday's law of induction)}$$

where $\vec{J}$ is the surface current density and q is the charge density.

The first equation is the Gauss law for the conservation of magnetic flux and it mathematically represents the fact that the magnetic flux lines always form a closed loop. This fact can be readily observed when iron filings form a pattern around a permanent magnet. The third equation takes a special form in magneto-solid mechanics problems which deal with low frequencies. The wavelength associated with wave solutions in such problems is much longer. The displacement current term $\frac{\partial D}{\partial t}$ is, therefore, small for low frequencies and the Maxwell equation reduces to the steady state Ampere's circuital law (quasistatic approximation) , $\nabla \times \vec{H} = \vec{J}$ which in the integral form may be expressed as

$$\oint_{\partial\Omega} \vec{H} d\vec{l} = Ni \tag{1.21}$$

where N is the number of current carrying conductors in the domain Ω with boundary $\partial\Omega$, each carrying a current of i Amperes. In the case of a long thin solenoid, equation (2.11) reduces to the simple form $H = Ni/L$.

The last equation of Maxwell is just a reinterpretation of Faraday's law of electromagnetic induction and it signifies that the curl of the electric field is determined by the rate of change of magnetic induction. The induced potential is said to oppose the change in magnetic flux and hence, the negative sign. Maxwell's last equation is the same as equation (1.11).

CHAPTER 2

REVIEW OF CONCEPTS DEVELOPED FOR UNDERSTANDING THE NI-MN-GA MAGNETOSTRAIN EFFECT

2.1 Introduction

This chapter presents a literature review of existing martensite reorientation models which are focused on the estimation of magnetization and strain in FSMA's. A brief outline was provided in Section 1.4 regarding the nucleation of variants and twin boundary motion in the tetragonal martensitic structure. The review discussed in this chapter concentrates on free energy expressions for magnetization and strain in accordance with the tetragonal martensitic structure. In the presence of external stress, models have been extended to explain the orthogonal field-stress pair effect which is different from the collinear field-stress drive configuration employed in the research presented in this thesis. The measurements reported here have demonstrated field-induced reversible strains as large as 6400 ppm (0.64%) despite the lack of a readily recognizable mechanism for the observed effect. Some of the reviews presented in this chapter provide a general overview of magneto-strain effects which help to draw preliminary ideas on explaining the phenomena being measured. The more detailed

magnetization and strain modeling aspects stem from the change in crystallographic geometries and ensuing change in magnetic properties in presence of magnetic fields.

2.2   Martensite Reorientation Models

On nucleation of the martensitic region within the parent austenitic phase, the strain can be compensated by slip or by formation of strained twin variants separated by twin boundaries, because these mechanisms minimize the total strain energy between the martensitic region and the untransformed surroundings. Twin boundary motion is thought to be an easier deformation mode than slip in ordered alloys since slip involves breaking of more bonds.

The model proposed in [17] model takes into account both phase boundary motion and twin boundary motion. Nevertheless, the giant field-induced strains in the martensitic state of Ni-Mn-Ga are associated with twin boundary motion driven by the Zeeman energy difference ΔM·H, where ΔM is the magnetization differential across the boundary and H is the magnetic field. The model therefore, includes the effect of magnetic anisotropy within the martensitic twins and assumes that the sample is planar and is composed of only two variants. The model considers three regimes with respect to the strength of the magnetocrystalline anisotropy energy K_u in the martensitic phase which are presented in terms of dimensionless field parameters $h_e = M_s H / C e_0^2$ and $h_a = M_s H / 2 K_u$. Here, M_s is the saturation magnetization, C is the effective stiffness, H is the field and e_0 is the transformation strain. The term ha is the ratio of Zeeman energy to the crystal anisotropy energy. The three regimes are $h_a \ll 1$, $h_a \gg 1$ and $h_a \approx 1$. When $h_a \ll 1$, the effect of the applied magnetic field is to move the twin boundaries as opposed to the rotation of magnetization within
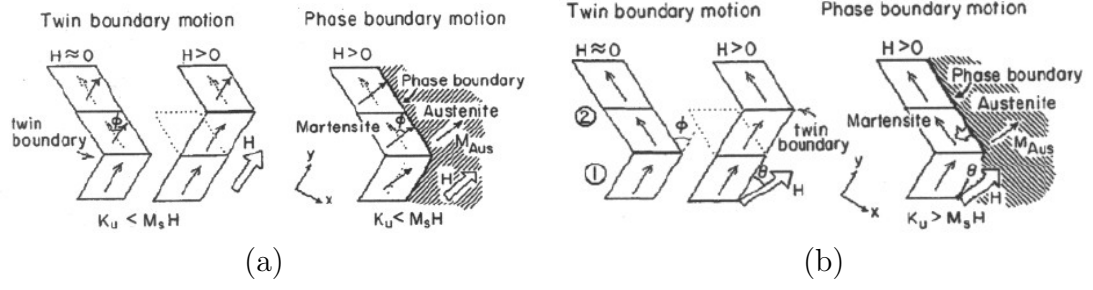
Figure 2.1: Mechanism for twin boundary motion and phase boundary motion when the martensitic anisotropy is (a)weaker than the Zeeman energy and (b) stronger than the Zeeman energy (austenite phase still has low anisotropy) [17].

the unfavorably oriented twins and the anisotropy of the variants remain unchanged. The driving pressure for twin boundary motion is the free energy density difference across the twin boundary. When $h_a \gg 1$, magnetic saturation is easily achieved even in weak fields due to the rotation of M_s and no strain due to twin boundary motion is expected. If $h_a \approx 1$ then the magnetization and strain depend on both h_e and h_a.

For the strong anisotropy case $h_a \ll 1$, the magnetic free energy density after partial twin boundary motion is given by,

$$g_{mag} = -M_s H \left[f_1 \cos \theta + f_2 \cos(\theta + \phi) \right] + A(\phi/\delta)^2 \tag{2.1}$$

where f_1 and f_2=1-f_1 are the volume fractions of the two twin variants as shown in Fig. 2.1. Here, A is the exchange stiffness constant and δ is the length over which the magnetization rotates from one twin variant to the other and is the larger of the domain wall thickness δ_{dw} or the twin boundary thickness δ_{tb}. Since achieving a single variant state is rarely possible, the change in energy due to twin boundary motion will not depend strongly on the exchange term and can thus be omitted. However, an elastic energy term must be considered since twin boundary motion occurs at the

43

expense of the elastic energy. Such term may have the form

$$g_{elastic} = \frac{1}{2}Ce_0^2(f_1^2 + f_2^2 + 2f_1f_2\cos\phi) \tag{2.2}$$

where C is the elastic stiffness constant against which the twin boundary motion occurs and e_0 is the strain associated with the transformation. Assuming an equal volume fraction of the two types of variants before the twin boundary motion, f_1 and f_2 can be written as $f_1=1/2+\delta f$ and $f_2=1/2-\delta f$ where δf is the fraction of the unfavorable variants that change into the favorable ones. Hence, $\delta f=0$ defines the initial state and one of the minimum energy states. If a mechanical bias stress is applied before the application of a magnetic field, $f_1 \neq f_2 \neg 1/2$ since the mechanical bias stress would try to convert the variants into a single variant with the crystallographic easy axes oriented in the direction of the applied stress. The total magnetic and elastic energy is given by combining equations (2.1) and (2.2),

$$\begin{aligned} g_{total} &= -M_sH\left[(\frac{1}{2}+\delta f)\cos\theta + (\frac{1}{2}-\delta f)\cos(\theta+\phi)\right] \\ &+ \frac{1}{2}Ce_0^2\left[\frac{1}{2}+2\delta f^2 + (\frac{1}{2}-2\delta f^2)\cos\phi\right]. \end{aligned} \tag{2.3}$$

Equation (2.3) is then minimized to get the equilibrium fractional twin-boundary displacement. The final equations developed for magnetization and strain are,

$$\begin{aligned} m &= \frac{M}{M_s} = \frac{1}{2}\left(u_+ + \frac{p_-^2}{v_-}h_e\right) \\ \epsilon_x &= \frac{e_x}{e_0} = \frac{\sin\varphi}{2v_-}(v_- - u_-h_e) \\ \epsilon_y &= \frac{e_y}{e_0} = \frac{1}{2}(v_+ + u_-h_e) \end{aligned} \tag{2.4}$$

where $u_\pm=\cos\theta \pm \cos(\theta+\phi)$ and $v_\pm=1\pm\cos\phi$. These equations show that the magnetization and field-induced strain are linear with H.

In the case where $h_a \approx 1$, Zeeman pressure is exerted on the twin boundaries before the magnetization rotates into the direction of the applied field and at higher fields, after significant rotation of the magnetization in the field direction has occurred, the Zeeman pressure on the twin boundaries decreases to the value of the anisotropy energy difference across the interface. For this case, the total free energy is given by,

$$g_{total} = -(f_1 + f_2 \cos \psi) M_s H + \frac{1}{2} C e_0^2 (\frac{1}{2} + 2\delta f^2) + f_2 K_u \cos^2 \psi \qquad (2.5)$$

where ψ is the angle between the magnetization of the unfavorably oriented variant and the applied field. Equation (2.5) includes the elastic energy and magnetic anisotropy energy in the unfavorably oriented twin variant, in addition to the Zeeman energy. Equation (2.5) is minimized with respect to δf and ψ and the equations for magnetizationa and strain are given by,

$$
\begin{aligned}
m &= \frac{1}{2} \left[1 + h_a + h_e(1 - h_a) \left(1 - \frac{h_a}{2} \right) \right] \\
\epsilon_x &= \frac{1}{2} \left[1 - h_e \left(1 - \frac{h_a}{2} \right) \right] \\
\epsilon_y &= \frac{1}{2} \left[1 + h_e \left(1 - \frac{h_a}{2} \right) \right]
\end{aligned}
\qquad (2.6)
$$

Equation (2.6) infers linear behavior at weak fields and a negative curvature at higher fields. A more general equation regarding the free energy for two variants was given by O'Handley [18],

$$g = -M_i H + K_u \sin^2 \theta_i + \sigma e + \frac{1}{2} C e^2 \qquad (2.7)$$

where i corresponds to either variant 1 or 2. Equation (2.7) is the same as relation (2.5) except for the additional term due to the applied external stress that is orthogonal to the applied field direction. Minimization of the free energy with respect to

the twin boundary displacement ∂f and the angle θ, yields the following expression
for the strain

$$e(H) = e_0 \delta f = \frac{M_s H(1 - h_a) + K_u h_a^2 - \sigma e_0}{C e_0}.$$

(2.8)

Equation (2.8) shows that at small h_a, the field-induced strain is positive linear in H
and can be shifted towards negative values by applied stresses. It is seen that greater
strain is achieved with lower effective stiffness and transformation strain.

Likhachev and Ullakko [13] have employed a thermodynamic consideration of
the mechanical and magnetic properties and the basic mechanical state equation
including magnetic field effect is directly derived from a general Maxwell relation.
They have shown that the magnetic field-induced deformation is directly related to
the strain dependance of magnetization. The basics of this derivation is presented
here in brief. The following state equations can be written as a representation of
both the mechanical and magnetic properties of such materials which comes from the
general thermodynamic principles,

$$\sigma = \sigma(\varepsilon, h)$$

(2.9)

$$m = m(\varepsilon, h)$$

(2.10)

where equation (2.9) reflects the mechanical properties through stress-strain equation
in presence of the magnetic field and equation (2.10) gives the magnetization value
as a function of the applied magnetic field and strain. ¿From Maxwell's rule, the
dependency between the two state equations can be shown as,

$$\frac{\partial}{\partial h} \sigma(\varepsilon, h) = -\frac{\partial}{\partial \varepsilon} m(\varepsilon, h)$$

(2.11)

Integrating the above equation over the magnetic field from $h = 0$ at a fixed strain
gives an important representation of the mechanical state equation including magnetic

field effects,

$$\sigma = \sigma_o - \frac{\partial}{\partial \varepsilon} \int_0^h m(\varepsilon, h) dh \qquad (2.12)$$

Equation (2.12) represents the external stress as being balanced in equilibrium by the pure mechanical stress $\sigma_o = \sigma(\varepsilon, 0)$ resulting from the mechanical deformation of the material in absence of the magnetic field and the additional magnetic field-induced stress. If the external stress is zero, then the magnetic field-induced strain or the shape memory effect may be shown by,

$$\sigma_o(\varepsilon) = \frac{\partial}{\partial \varepsilon} \int_0^h m(\varepsilon, h) dh \qquad (2.13)$$

The truncated Taylor's series for equation (2.13) gives a linearized solution as follows,

$$\varepsilon_{msm}(h) = \left(\frac{d\sigma_o}{d\varepsilon} \right)^{-1} \frac{\partial}{\partial \varepsilon} \int_0^h m(\varepsilon, h) dh \qquad (2.14)$$

Equation (2.14) can be used when ε is lesser than martensitic lattice tetragonal distortion value $\varepsilon_o = 1\text{-}c/a$. The martensite state of Ni_2MnGa is thought to be a variable volume fraction of tetragonal variants in absence of external applied stress. When magnetic field is applied in a direction parallel to the easy axis of one of the variants, the other two variants get magnetized along the hard axis, i.e not the tetragonal easy axis of symmetry. A simple illustration is given in Fig. 2.2(a). The variant with the easy axis parallel to the magnetic field is called the axial variant and the two other variants are called transverse variants. The difference in magnetization for the two types of variants is shown in Fig. 2.2(b) where a higher field value is required for magnetization of the transverse variants.

The model developed by Likhachev and Ullakko treats the multi variant twinned martensitic state as a composite material consisting of an easy magnetization area
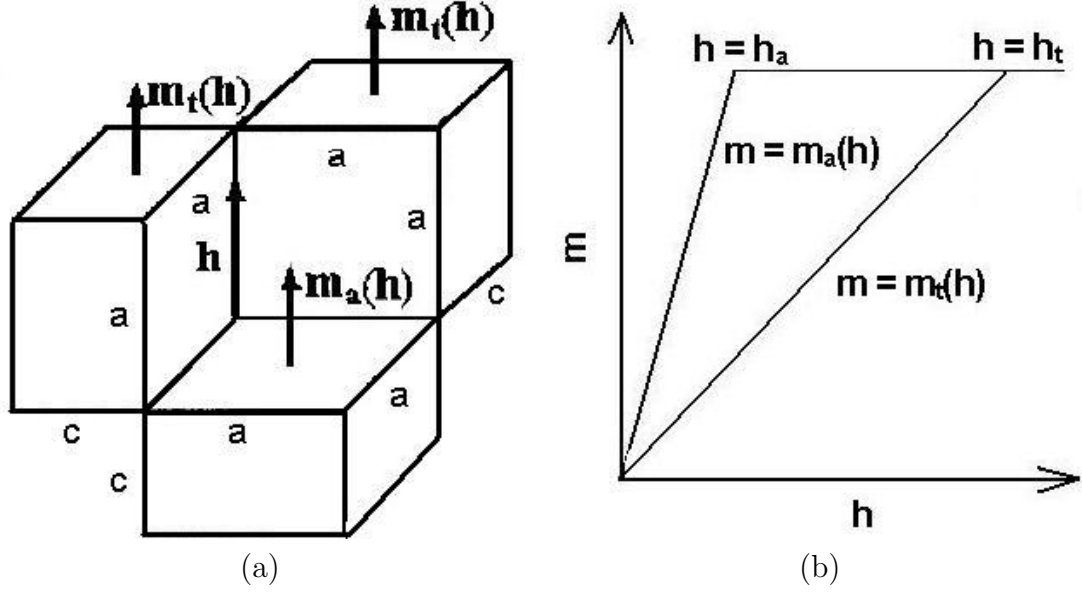
Figure 2.2: (a) A simple three dimensional representation of the crystallographic tetragonal variants in the martensitic phase and (b) magnetization along the axial and transverse directions [13].

occupied by axial type twins and hard magnetization region comprising the transverse twin variants. This is the fundamental concept behind the model developed henceforth. If x is the total volume fraction of the axial variants and accordingly, $(1 - x)$ is the volume fraction of the transverse variants, the magnetization of the material and the strain along the axial direction may be written as,

$$m(x, h) = xm_a(h) + (1 - x)m_t(h) \tag{2.15}$$

$$\varepsilon = x\varepsilon_a^0 + (1 - x)\varepsilon_t^0$$

$$= \frac{3}{2}\varepsilon_0(x - \frac{1}{3}) \tag{2.16}$$

where the suffix a and t refer to the axial and transverse variants. $\varepsilon_a^0 = \varepsilon_0$ and $\varepsilon_t^0 = -(1/2)\varepsilon_0$ represent the relative tetragonal distortion of the martensite crystal lattice along the tetragonal easy axis and the two transverse directions respectively. For

48

the samples of Ni_2MnGa (cubic phase: a=5.822A and tetragonal phase: a=b=5.90A, c=5.44A) experimented by Likachev and Ullakko, ε_0=5.4%. The magnetization can be written as a function of the macroscopic strain as follows after eliminating the volume fractions,

$$m(\varepsilon, h) = \left\{\frac{1}{3}m_a(h) + \frac{2}{3}m_t(h)\right\} + \frac{2}{3}\frac{\varepsilon}{\varepsilon_0}\{m_a(h) - m_t(h)\} \qquad (2.17)$$

The second term on the right side of equation (2.17) gives the strain dependance of magnetization. From equations (2.14) and (2.17), we arrive at the following equation for the strain,

$$\varepsilon_{msm}(h) = \frac{2}{3}\left(\varepsilon_0\frac{d\sigma_o}{d\varepsilon}\right)^{-1}_{\varepsilon=0}\int_0^h \{m_a(h) - m_t(h)\}\,dh \qquad (2.18)$$

From equation (2.18), it is seen that the strain is dependant both on the initial slope of the stress-strain curve (obtained from the mechanical compression test in absence of the magnetic field) and the magnetic anisotropy. It can be inferred that in absence of magnetic anisotropy, the deformation effect would also vanish. From Fig. 2.2(b), it is seen that saturation of magnetization is obtained at a field $h=h_t$ above which $m_a(h)=m_t(h)=m_{sat}$. So, the value of strain corresponding to saturation of magnetization can be expressed in the form,

$$\varepsilon_{sat}^{msm} = \frac{1}{3}\left(\varepsilon_0\frac{d\sigma_0}{d\varepsilon}\right)^{-1}_{\varepsilon=0}(h_t - h_a)m_{sat} \qquad (2.19)$$

which follows from Equation 2.18. The maximum strain in the axial direction in which the magnetic field is applied is given by,

$$\varepsilon_{max} = \frac{1}{3}\left(\varepsilon_0\frac{d\sigma_0}{d\varepsilon}\right)^{-1}_{\varepsilon=0}h_t m_{sat} \qquad (2.20)$$

Fig. 2.3(a) shows the plot for normalized strain $\varepsilon/\varepsilon_{max}$ against the normalized magnetic field h/h_{max} for different values of the magnetic anisotropy constant $k=h_a/h_t$.

49
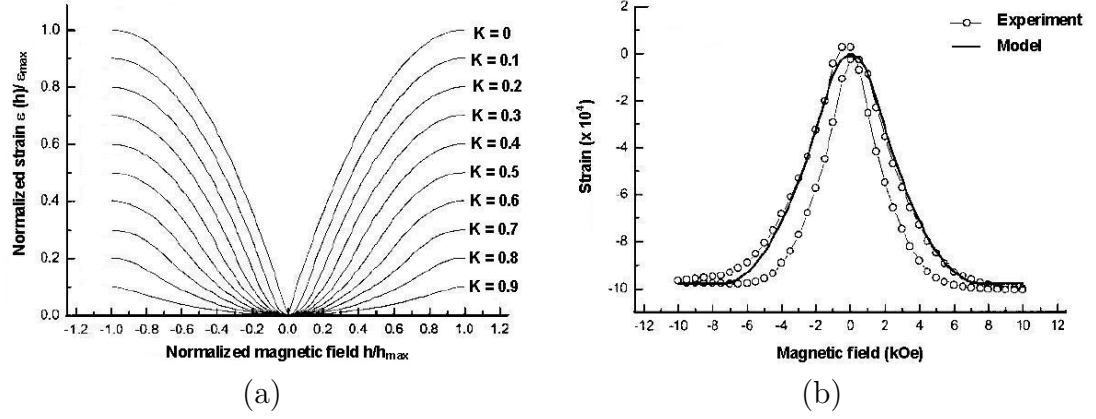
Figure 2.3: (a) Magnetic anisotropy effect on the strain versus magnetic field behavior based on the model predictions (b) Comparison between the model and the experimental result for the magnetostrain effect [13].

It is seen that as $k=1$,i.e, the manetic anisotropy becomes weaker, the strain reduces to zero. Similarly, $k=0$ implies that h_a has a very low value as compared to h_t so that m_a achieves the the saturation level m_{sat} immediately and remains at that constant value during the magnetization process. This is a case of strong anisotropy due to the greater difference between the magnetizations of the axial and transverse variants. A point is made at this point that the linear field behavior predicted through some earlier models [17] is directly connected with the assumption of complete saturation magnetization of the axial type twin variants. However, in the model developed by Likhachev and Ullakko, such an assumption is only valid in the limit $h \rightarrow 0$. Fig. 2.3(b) shows the comparison of the magnetostrain effect between the experimental data obtained by the authors and their model. At low fields $h < h_a$, the magnetostrain predicted by the model has a parabolic nature which resembles the experimental data. This type of parabolic behavior at very low fields is not accounted for in O'Handley's model.

A further development on this model was made by Likhachev and Ullakko [12] where the twin boundary motion responsible for the large magnetostrain effects were related with the magnetic driving force. O'Handley refers to this driving force as the force due to Zeeman energy difference. From equation (2.20), it is seen that a lower twinning stress value would enhance the field-induced strain of the material. Likhachev and Ullakko observed that Ni-Mn-Ga samples with a very low compressive twinning stress in the range of 2-3 MPa along the [100] axis that is required to transform the multi variants into a single variant state, showed giant field-induced strain. This implies that the samples have to be soft. The twinning stress value is an important quantity that influences the capability of the magnetic driving force to actuate twin boundary motion.
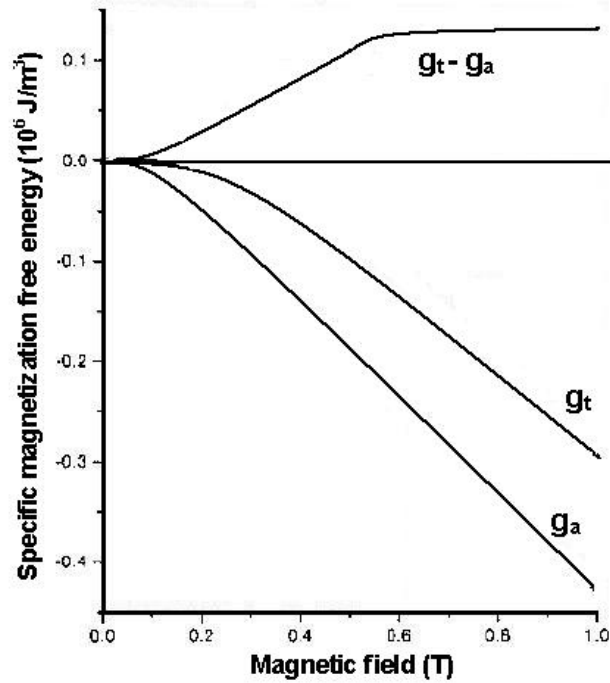
Figure 2.4: Magnetic anisotropy of $Ni_{48}Mn_{30}Ga_{22}$ and field dependance of magnetization free energies for easy and hard magnetization directions.

51

The free energy curves for the axial and transverse variants are shown in Fig. 2.4. The magnetization free energies as a function of the applied magnetic field can be calculated as follows,

$$g_a(h) = -\int_0^h m_a(h)dh$$
$$g_t(h) = -\int_0^h m_t(h)dh \tag{2.21}$$

The total magnetization free energy can be written in the same form as for strain and magnetization based on the volume fraction of the martensite variants.

$$g(x, h) = xg_a(h) + (1 - x)g_t(h) \tag{2.22}$$

It is seen that the magnetization free energy for the axial variants is less than that for the transverse variants and since a minimum energy state is always preferred, there must exist a force within the microstructure so that the axial variant grows at the expense of the transverse variants. This is easily understood by substituting x=1 in equation (2.22). From the general thermodynamic rule, the magnetic driving force moving twin boundaries along their normal directions is given by,

$$
\begin{aligned}
f_{mag}(h) &= -\left[\frac{\partial}{\partial x}g_{mag}(x, h)\right]_h \\
&= g_t(h) - g_a(h) \\
&= \int_0^h (m_a(h) - mt(h))dh \tag{2.23}
\end{aligned}
$$

Equation (2.23) implies that a non-zero magnetic driving force is possible due to the uniaxial magnetic anisotropy of Ni-Mn-Ga and is quantified by the difference of the magnetization free energies between the different twin variants. Fig. 2.5 shows the schematic of the martensitic twinned microstructure with the white and and gray area indicating the region of the axial and transverse variants respectively. The magnetic
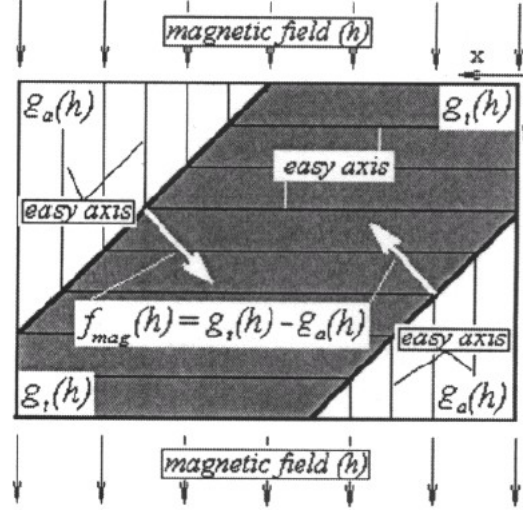
Figure 2.5: Two dimensional representation of two variant twin microstructure, easy magnetization axes alignment and magnetic driving force responsible for twin boundary motion in an applied magnetic field.

field is applied in the vertical direction. The magnetic driving force is responsible for moving the twin boundaries in a direction normal to the boundaries reducing the volume fraction of the transverse variants and at the same time increasing the volume fraction of the axial variants. This is termed as the growing of the favorable variant with the expense of the unfavorable ones. From equation (2.23) the maximum magnetic driving force is achieved when $h \rightarrow \infty$ which is equal to the uniaxial magnetic anisotropy K_u. So,

$$h \rightarrow \infty, f_{mag}(h) \longrightarrow K_u = \int_0^\infty (m_a(h) - mt(h))dh \qquad (2.24)$$

A maximum magnetic driving force value of 0.13 MPa was obtained at $h > 0.8T$ for $Ni_{48}Mn_{30}Ga_{22}$. The normal mechanical driving force as a function of the applied stress is given by,

$$f_{mech}(\hat{\sigma}) = \hat{\varepsilon}_0 \hat{\sigma} = \varepsilon_0(\sigma_{xx} - \sigma_{yy}) \qquad (2.25)$$

where $\hat{\varepsilon}_0$ is the strain matrix associated with the twinning transformation between two single variants of the martensitic phase. In the planar reference system as shown in Fig. 2.5, it is represented by a diagonal matrix as follows:

$$\begin{pmatrix} \varepsilon_0 & 0 & 0 \\ 0 & -\varepsilon_0 & 0 \\ 0 & 0 & 0 \end{pmatrix}$$

where $\varepsilon_0 = 1 - c/a$ is the twinning transformation value which can be estimated from the martensitic phase lattice parameters. For the Ni-Mn-Ga sample tested, $a = b = 0.594$ nm and $c = 0.562$ nm which gives $\varepsilon_0 = 5.79\%$. Some universality rules have been opted to calculate the macroscopic twinning strain as a function of the driving force. The macroscopic strain is taken to be some universal function dependant only on the driving force value irrespective of the physical source of the force. In the case of planar twinning, both non-zero components of the strain may be written as a single universal function that is dependant on the normal driving force as follows:

$$\varepsilon_{yy} = -\varepsilon_{xx} = \varepsilon'(f)$$

The mechanical and magnetic strains can then be represented as

$$\varepsilon_{yy}^{mec}(\hat{\sigma}) = -\varepsilon_{xx}^{mec}(\hat{\sigma}) = \varepsilon'(\hat{\varepsilon}_0 \hat{\sigma}) \tag{2.26}$$

$$\varepsilon_{yy}^{mag}(\hat{\sigma}) = -\varepsilon_{xx}^{mag}(\hat{\sigma}) = \varepsilon'(g_t(h) - g_a(h)) \tag{2.27}$$

In the case of uniaxial compressive stress ($\varepsilon_{xx} = \varepsilon_{zz} = 0$, $\varepsilon_{yy} = -\varepsilon$) the mechanical and magnetic strains will take equal values only if the corresponding mechanical and magnetic driving forces are equal which results in,

$$\sigma = \sigma_{mag}(h) = \varepsilon_0^{-1}(g_t(h) - g_a(h)) = \varepsilon_0^{-1} \int_0^h (m_a(h) - m_t(h))dh \tag{2.28}$$

54

and hence,

$$\hat{\varepsilon}^{mag}(h) = \hat{\varepsilon}^{mec}(\sigma_{mag}(h)) \tag{2.29}$$

Equation (2.29) allows the calculations for the magnetic field-controlled strains using the corresponding mechanical testing data. The deformation effect of the applied magnetic field is equivalent to the uniaxial compressive stress applied and this equivalent magnetic stress $\sigma_{mag}(h)$ can be computed from equation (2.28). For the sample of interest, the maximum magnetic equivalent stress that can be developed is about 2.25 MPa. This value can then be compared to the twinning stress from the mechanical compression test data which does not exceed 2.5 MPa. Since a maximum compressive strain of 5.79% is achieved at this twinning stress, the magnetic stress value is enough to achieve strains up to about 5%.

Simple Fermi-like distribution function given by equation (2.30) was used as an appropriate fitting basis for the analytic interpolation of the mechanical testing results.

$$\hat{\varepsilon}^{mec}_{\pm}\sigma = \varepsilon_0 \left\{ 1 + exp \left(\frac{\pm \sigma_0 - \sigma}{\Delta \sigma} \right) \right\}^{-1} \tag{2.30}$$

where $\pm$ denotes the loading and unloading curves respectively, σ_0 and $\Delta \sigma$ are the characteristic stress parameters associated with the start ($\sigma_s = \sigma_0 - 2\Delta\sigma$) and finish ($\sigma_f = \sigma_0 + 2\Delta\sigma$) twinning stress values.

Fig. 2.6(a) shows the results of equation (2.30) along with the fit from the experimental data and Fig. 2.6(b) shows the magnetostrain effect. The strain corresponding to each value of the applied magnetic field is obtained using equations (2.28) and (2.29). The magnetic stress value is computed using the magnetization data for the axial and transverse variants at each value of the applied magnetic field. As discussed
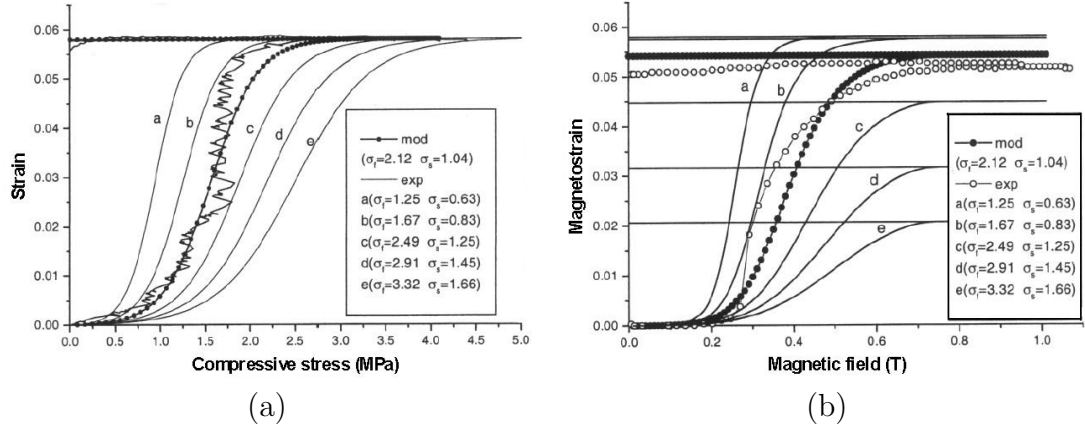
Figure 2.6: (a) Strain-stress behavior of $Ni_{48}Mn_{30}Ga_{22}$ from model calculations and experimental data (b) Magnetostrain effect from model calculations and experimental data [12].

before, the magnetic equivalents stress produces the same amount of strain as the applied stress. The mechanical strains corresponding to the applied mechanical stress would also correspond to the equivalent magnetic stress and hence to the respective values of the applied magnetic field finally resulting in Fig. 2.6(b).

The discussion presented above does not take into account the reversibility of the field-induced strain in the Ni-Mn-Ga shape memory alloys and the phenomenon of field induced-strain was explained through the idea of equivalent magnetic stress that is generated due to the applied magnetic field. It was observed that the material did not show appreciable reversible strains for an applied cyclic magnetic field in absence of an applied external stress. The large magnetostrains produced would not serve much in technical applications if they are irreversible. Likhachev, Sozinov and Ullakko [11] explored the possibility of reversible field-induced extensional strains through the application of orthogonal magnetic field-stress pair. The total field-induced strain is always the maximum in case of zero applied magnetic field but the magnitude of the

reversible component of strain is always the highest at some optimal stress and not at zero stress. The external stress is used for biasing the material toward a single variant so that the easy tetragonal axis is parallel to the direction of the applied stress. In the presence of an external stress, equation (2.29) takes the form,

$$\hat{\varepsilon}^{mag}(h) = \hat{\varepsilon}^{mec}(\sigma_d(h)) \tag{2.31}$$

where $\sigma_d(h)=\sigma_{mag}(h)-\sigma$ is the total driving stress and σ is the applied external compressive stress. During extension, of the material, the external stress opposes the equivalent magnetic stress. Fig. 2.7 shows the reversible field-induced strains in absence of an external stress and at 1.5 MPa. It is seen that the reversible component of strain at 1.5 MPa is higher though the magnitude of the total strain is less than that at zero field. An external stress of 1.37 MPa produces a maximum reversible strain of 3.56% for the composition of the specimen used by the authors.

This model cannot explain the phenomenon observed in the dls samples subjected to collinear field-stress pair in this thesis since the samples show maximum reversible strain in the absence of external stress which decreases sharply with increasing stress. Henry's [6] results on field-induced strain in $Ni_{49.8}Mn_{28.5}Ga_{21.7}$ obtained through orthogonal AC magnetic field actuation show the presence of an optimum external stress at which maximum reversible strain is achieved. At a field of about 6.28 kOe (500 kA/m), a maximum extensional strain of 2.5% was obtained at 1.85 MPa and the strain is largely blocked at 3.8 MPa.

2.3 Different Martensite Structures and Comparative strains

The explanation in the preceding paragraphs confirm a direct dependance of the magnitude of field-induced strain on the mechanical compression test data. The
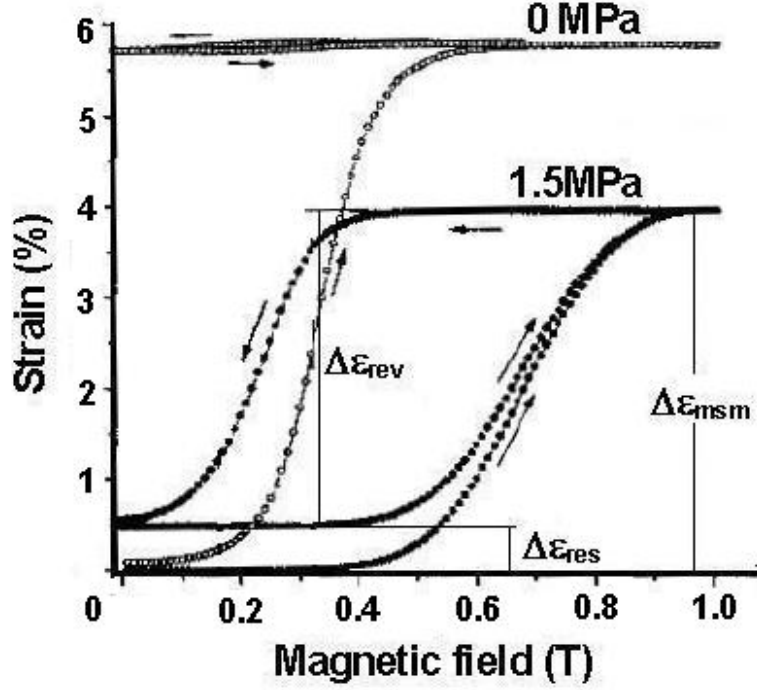
Figure 2.7: Strain vs field curves predicted by the model [11].

amount of field-induced strain depends on the start (σ_s) and finish (σ_f) twinning stress from the mechanical compression test data. Based on this, three categories of strain may be established with respect to $\varepsilon_0 = 1\text{-}c/a$ [22]:

1) Super-large strain effect($\varepsilon_{msm} = \varepsilon_0$) if $\sigma_{mag} > \sigma_f$.

2) Large strain effect ($\varepsilon_{msm} < \varepsilon_0$) if $\sigma_s < \sigma_{mag} < \sigma_f$.

3) Very small strain ($\varepsilon_{msm} \ll \varepsilon_0$) if $\sigma_s > \sigma_{mag}$.

Up to now three different types of martensitic structures have been found in the Ni-Mn-Ga shape memory alloys. They are the tetragonal five layered modulated (5M), orthorhombic seven layered modulated (7M) and tetragonal nonlayerd (T) with the
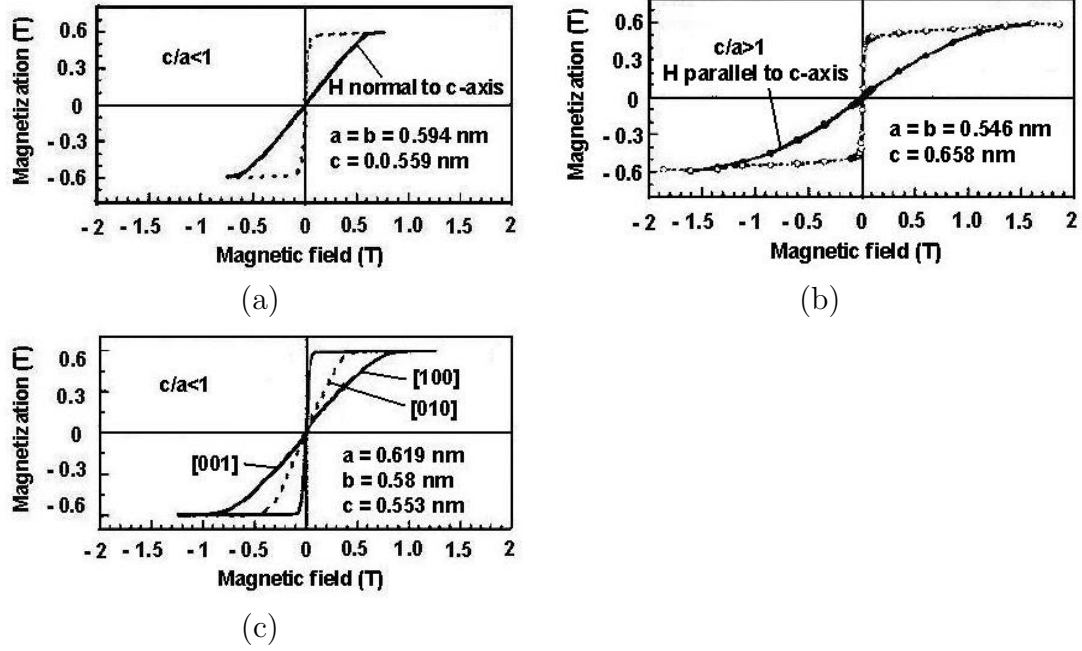
Figure 2.8: Magnetization curves for different martensite phases: (a) Five layered tetragonal phase (5M) (b) Non-layered tetragonal phase (T) (c) Seven layered orthorhombic phase (7M) [21].

lattice properties $c/a <1$, $c/a >1$ and $a > b > c$ respectively. Fig. 2.8 shows the magnetization curves for the three types of martensite structures. In all the three cases, it is seen that the shortest crystallographic axis is the easy axis of magnetization. In the seven layered tetragonal structure, two anisotropy constants exist which can be computed by calculating the area between the easiest axis of magnetization curve and the two hard axes magnetization curves. The magnetic equivalent stress has a maximum value of $\sigma_{mag} = \epsilon_0^{-1} K_u$ and can never exceed this saturation value.

In the tetragonal 5M martensite, $(\sigma_{mag})_{max} = 2.6$ MPa for an applied field of the order 1.1T and from the mechanical compression tests, $\sigma_f \leq 2.5$ MPa. The stress

due to the applied field is, therefore, completely capable of overcoming the maximum twinning stress and produce a super-large 5.8% magnetostrain effect. In the orthorhombic 7M martensite, $(\sigma_{mag})_{max} \approx 1.56$ MPa which is in between $\sigma_s = 1.9$ MPa and $\sigma_f = 1.1$ MPa and as a result only large strain of 9.5% is achieved [21]. Similarly, in the tetragonal nonlayered phase, estimated $(\sigma_{mag})_{max} = 1.1$ MPa is considerably low compared to the twinning stress range of 12-20 MPa and a very small magnetostrain effect of less than 0.02% is observed.

CHAPTER 3

MATERIAL PREPARATION AND EXPERIMENTAL FIXTURE

This investigation demonstrates for the first time the feasibility of obtaining large bidirectional strains from Ni-Mn-Ga alloys driven under a collinear magnetic field-stress pair, as opposed to the conventional perpendicular configuration. Existing martensite reorientation models suggest that the collinear field-stress configuration drives boundary motion in an irreversible fashion since tetragonal martensite has the same easy magnetic and stress axes. While the exact nature of the phenomena observed in this investigation is not completely understood, in order to gain a fundamental understanding and ultimately be able to develop constitutive models of the magnetoelastic and thermoelastic behavior exhibited by these alloys, the dependence of the magnetic and physical properties on the composition and structural characteristics of the ferromagnetic shape memory transformation must be elucidated. The results presented here provide a first step toward that end by presenting room-temperature magnetization and strain measurements for Ni-Mn-Ga alloys centered on $Ni_{49.56}Mn_{29.59}Ga_{20.85}$ under large quasistatic fields and varied compressive stresses.

Samples for this investigation were prepared at the Materials Preparation Center of the Ames Laboratory (DOE) in Ames, Iowa. Details regarding preparation procedures and sample compositions are provided in Section 3.1. The implementation of the collinear field-stress configuration was done by means of a test bed consisting of water-cooled solenoid transducer and a compressive loading fixture. The remainder of the chapter provides details on the construction and calibration of this test fixture. Detailed drawings of the different transducer and fixture parts are provided in Appendices A-C.

3.1   Sample Preparation and Properties

Six cylindrical samples of various parent phase compositions were tested. Each sample was prepared as follows. Appropriate quantities of high purity nickel, manganese and gallium were cleaned and arc melted several times under an argon atmosphere. The buttons were remelted and the alloy drop cast into a chilled copper mold to ensure compositional homogeneity throughout the ingot. The crystal was grown from the as-cast ingot in an alumina Bridgman style crucible which was heated to 1350°C under a pressure of 1.3×10^{-4} Pa to degas the crucible and charge. After melting, the chamber was backfilled to a pressure of 2.76×10^5 Pa with high purity argon to eliminate gas pockets and to minimize the amount of manganese evaporation from the melt during the crystal growth. The ingot was held at 1350°C for 1 hour to allow thorough mixing before withdrawing the sample from the heat zone at a rate of 5 mm/hr.

Cylindrical samples measuring 0.25" (6.35 mm) in diameter were extracted from the crystal boule by electric discharge milling, and their composition measured along

the longitudinal axis by energy dispersive microanalysis. Because the composition is known to vary along the boule axis with Mn content increasing and Ga content decreasing in the growth direction, the tested samples were taken from the top and bottom of each boule for maximum compositional variation within each boule. Table 3.1 shows the compositions in percentage by atomic weight for the different samples while Tables 3.2 and 3.3 show the characteristic temperatures for the tested samples.

Sample	Mn	Ni	Ga	e/a*	Length (inches)	Density (gm/cc)
dls-1-136-1	28.7	50.0	21.3	7.648	0.883	7.886
dls-1-125-4	30.60	48.10	21.30	7.951	1.025	7.44
dls-1-61-1	29.98	48.99	21.03	7.629	0.954	7.88
dls-1-42-1	30.40	49.54	20.06	7.684	0.840	8.15
dls-1-42-2	28.91	50.52	20.57	7.693	0.842	8.16
dls-1-42-3	28.97	50.20	20.84	7.673	0.851	8.07

*e/a =(7Mn+10Ni+3Ga)

Table 3.1: Compositions in percentage by atomic weight of nickel, manganese and gallium for the six samples tested in the study.

3.2   Solenoid Transducer

The experimental data in this investigation was obtained from the test apparatus shown in Fig. 3.1, which consists of a broadband solenoid-based transducer and a fixture that provides static uniaxial stresses by means of dead weights. The transducer houses one cylindrical sample of dimensions up to 0.5"-diameter by 4.5"-length and is configured for d_{33} actuation mode with the longitudinal axis of the sample, magnetic field, and uniaxial stress aligned collinearly.

Sample ID	Rod no.	$A_s(1^a)$	$A_f(1)$	$M_s(1)$	$M_f(1)$
dls-1-136	1,top	42	65.9	55.3	32.4
	1,bottom	43.7	62.5	54.8	33.1
dls-1-125	4,top	33.1	87.7*	77.7	-
	4,bottom	37.5	54.4	45.4	20.0
dls-1-61	1,top	49.5	64.1	54.2	43.0
	1,bottom	43.0	69.8	61.0	40.7
dls-1-42	1,top	49.8	111.1*	106.7**	60.8
	1,bottom	+	100.2	90.0**	60.4
	2,top	+	113.6*	108.4	76.9
	2,bottom	76.6++	103.6	94.4	65.6
	3,top	80.7++	118.5	108.8	77.2
	3,bottom	+	104.4	95.6	73.6

Table 3.2: Characteristic temperatures in °C for the tested samples

Sample ID	Rod no.	$A_s(2^b)$	$A_f(2)$	$M_s(2)$	$M_f(2)$	T_c (heating)	T_c (cooling)
dls-1-136	1,top	-	-	-	-	101.1	98.0
	1,bottom	-	-	-	-	100.6	98.2
dls-1-125	4,top	-	-	-	-	87.7	87.0
	4,bottom	-	-	-	-	96.9	94.6
dls-1-61	1,top	-	-	-	-	96.7	94.5
	1,bottom	-	-	-	-	97.0	95.4
dls-1-42	1,top	-	-	-	-	111.1	106.7
	1,bottom	52.7	+	4.7	-23.9	100.2	90.0
	2,top	47.4	+	-11.6	-49.5	120.2	114.9
	2,bottom	49.2	67.0++	-4.6	-23.2	103.6	99.4
	3,top	53.7	71.4++	-21.2	-51.2	124.6	119.5
	3,bottom	48.4	+	-4.5	-26.4	112.2	107.6

[a]High temperature martensite transformation, [b] Low temperature martensite transformation, *A_f=T_c, *M_s=T_c, +$A_f(2)$ and $A_s(1)$ overlap, ++$A_f(2)$ and $A_s(1)$ overlap on one cycle only.

Table 3.3: Characteristic temperatures in °C for the tested samples.
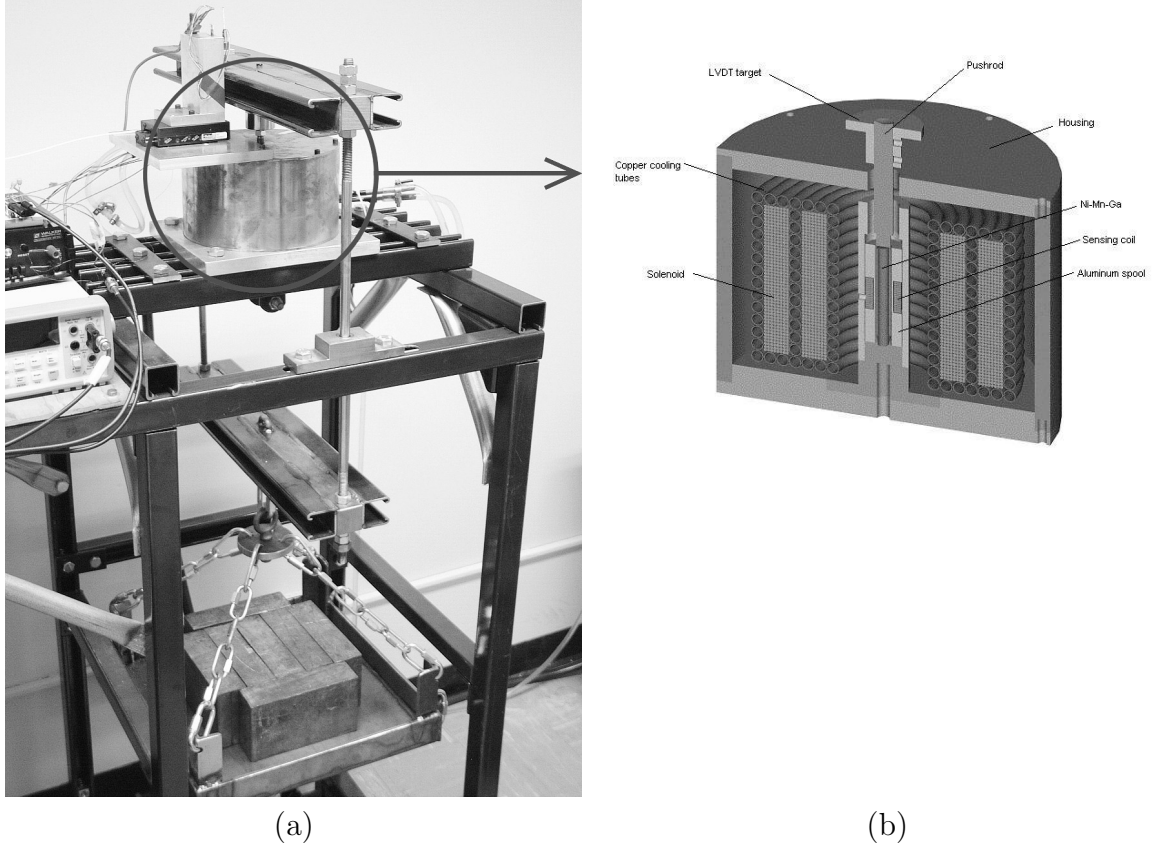
Figure 3.1: (a) Fixture employed for testing Ni-Mn-Ga samples with a collinear magneitc field-stress pair (b) Three dimensional sectioned view of the main transducer showing the interior.

The transducer consists of several parts made from magnetic and non magnetic materials for efficient flux flow. As illustrated in Figs. 3.1(b) and 3.2, the housing comprises a cylindrical housing and top and bottom plates made from 1018 steel. A 1018 magnetic steel base is screwed to the bottom plate and a bottom cap made from stress proof 1144 steel is fixed to the magnetic steel base. A 6061 T6 hollow aluminum spool and sensing solenoid sit inside a sample holder made of 304 stainless steel. The sample holder has internal threads at the bottom and is screwed to the

65

external threads of the bottom cap. A linear motion bearing is press fit on the top of the sample holder to support the motion of the pushrod with minimum friction and for closing the magnetic circuit formed by the Ni-Mn-Ga sample, top and bottom plates and caps and the transducer housing.

The drive fields are provided by a water-cooled solenoid consisting of AWG15 insulated copper wire wound in 28 layers with approximately 48 turns per layer. A cooling/heating circuit of 0.25 in-diameter copper tube is interspersed within the solenoid and high performance epoxy Epotek T7109 provides structural support to the assembly. Water is circulated in the system at a rate and temperature regulated by means of a water mixer. The temperature at different locations in the transducer is monitored by Omega thermocouples connected to a 10-channel Omega signal conditioner. For all of the tests, the sample temperature was maintained at 14°C. The solenoid is driven by two Techron 7790 amplifiers connected in series which produce an overall voltage gain of 60 and maximum output current of 56 A at the rated coil resistance of 3.7 Ω (11.6 kW). The magnetic induction is measured with a pickup coil made from AWG33 grade insulated copper wire wound several layers around the aluminum spool and connected to a Walker Scientific MF-5D integrating fluxmeter which directly converts the change in voltage across the sensing coil to magnetic induction.

Since the Ni-Mn-Ga samples are more than an inch shorter than the height of the solenoid, two magnetic stress proof 1144 steel pieces of equal length were attached with wax to the top and bottom of the samples, thus aiding in positioning the sample symmetrically at the center of the solenoid's longitudinal axis. Compressive loading is applied to the samples through a pushrod made of 1144 stress-proof magnetic steel connected to a steel cross bar with an interface piece of non-magnetic 304 stainless

steel in between to prevent the magnetic flux lines from leaking out. A second cross bar connected to the top cross bar by means of vertical non-magnetic steel rods provides a means for hanging a set of interconnecting steel trays which hold lead bricks. The vertical rods slide in low-friction linear motion bearings which are rigidly attached to the fixture frame. The number of trays and lead bricks connected to the transducer's load path can be varied such that the compressive force on the sample is adjusted from zero up to a maximum of 1.5 kip (6.6 kN) in virtually continuous increments. A PCB 208C04 force transducer is located between the cross bar and the interface piece of non-magnetic steel, and is used to monitor the compressive force applied to the Ni-Mn-Ga sample. The strain is measured by a Lucas Shaevitz MHR-025 linear variable differential transducer. Fig. 3.2 shows the cross section of the transducer without the loading fixture. The input and output signals are generated by and recorded through a Data Physics SignalStar Vector 550 dynamic signal analyzer that is interfaced through a PC.

3.2.1   Water-Cooled Solenoid

It is noted that in order to produce larger magnetic fields from a solenoid, increasing the number of windings per unit length is more effective than increasing the coil current. This is due to the Joule heating being proportional to the square of current, while the field is directly proportional to current. Consequently, if the current flowing in the solenoid is doubled, then the Joule heating increases four times. However, if the number of windings is doubled, the resistance gets doubled and the Joule heating increases only two times. Both the methods result in a doubling of the field. This
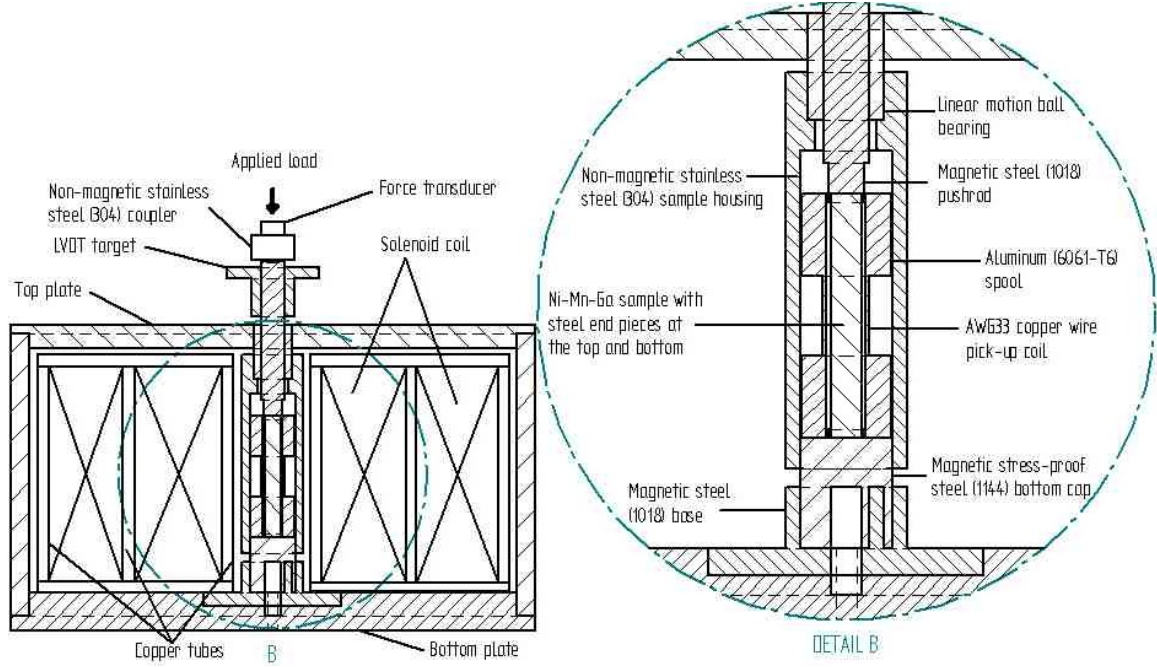
Figure 3.2: Cross section of the water-cooled transducer used for testing of the Ni-Mn-Ga samples.

design criterion has been employed in this investigation to prevent excessive heating of the transducer.

The solenoid is made of AWG15 insulated copper magnet wire and was prepared on an aluminum bobbin. The solenoid sits in between layers of copper cooling tubes which were also initially set into the configuration by wrapping them on a bobbin. The copper cooling tubes are 0.25 in in diameter and wound in three vertical layers and two horizontal layers (top and bottom). When setting the cooling tubes into the required shape on the bobbin, the tubes were filled with dry sand to prevent them from cracking while being bent into the spiral shape. The first layer of magnet wire was wrapped around the innermost layer of copper cooling tube, which was covered

68

with a layer of solder to form a smooth cylindrical surface. This is a crucial step in the fabrication of the transducer as the key to a good solenoid that produces an axially symmetric magnetic field depends on the uniformity of the subsequent windings. A layer of high performance Epotek T7109 epoxy was applied after every two layers of the solenoid coil for a strong bond as well as to enhance the thermal conductivity between the solenoid coils and the cooling tubes. The solenoid was cured in a hot air oven after the twelfth layer of winding and the second layer of cooling tubes was then wound. This was followed with another sixteen layers of magnet wire. The final layer of cooling tubes was wound, and the finished solenoid was cured thereafter.

The solenoid coil thus, had 28 layers of magnet wire with an average of 48 turns on each layer which gave a total resistance of 3.7 Ω to the solenoid. The solenoid can generate up to 8.1 kOe at maximum current of 56 A and voltage of 210 V across the solenoid terminals. Under quasi-static operations, this magnitude of current can produce considerable Joule heating which might damage the insulation on the magnetic copper wire, which can withstand 200°C. Water was, therefore, circulated at 6.25 liters/min through the cooling tubes to maintain a constant nominal temperature during testing of 14°C inside the transducer. The temperature of the system was monitored with four K-type thermocouples. Two of the thermocouples were placed outside the transducer casing, on the surface of the inlet and outlet of the innermost (first) layer of copper tubes. Another thermocouple was placed on the inner surface of the innermost layer of the copper tubes and the last thermocouple was placed on the outer surface of the non-magnetic steel housing. Both the latter thermocouples were placed roughly at midway along the height of the transducer. An Omega 10-channel temperature display unit was used to monitor the readings from each of the

thermocouples. A certain amount of time was provided after each test run to allow the system to return to the operating temperature as a precaution to avoid disparity in the data collected consecutively.

3.2.2 Magnetic Circuit

The transducer was designed and constructed with the goal to obtain a calibrated and repeatable means for applying magnetic fields and stresses onto the Ni-Mn-Ga samples. From a magnetism point of view, the main focus of the design was to achieve maximum magnetic flux lines to pass through the samples with minimum flux leakage.

The top and bottom plates and the outer casing are made of 1018 steel which serve as a smooth path with minimum reluctance for the flux lines. The magnetic steel bottom cap is made of stress proof 1144 steel to prevent the relief of any stress, and hence, deformations during test operation. The top surface of the magnetic steel bottom cap, on which the sample rests, was machined with a shallow cup-like structure to allow samples to sit flat and perfectly aligned with axis of symmetry of the transducer.

An aluminum spool is placed to support the sensing or pickup coil to measure the magnetic induction in the sample. This coil is made from AWG33 insulated copper wire wound in two layers around the narrow portion of the aluminum spool. The turns per turn area calibration of the sensing coil was calculated to be 104 turns per turn cm^2. Since the samples are more than an inch shorter than the drive solenoid, two magnetic stress proof 1144 steel pieces of equal length were attached to the top and bottom of the samples (with a little wax and kapton tape) for positioning the sample symmetrically at the center of both the drive solenoid and the sensing coil. The

sensing coil is longer than the Ni-Mn-Ga samples to avoid leakage from the steel end pieces into the coil's electromagnetic induction path. The sensing coil is connected to a Walker Scientific MF-5D integrating fluxmeter which converts the change in voltage across the sensing coil into magnetic induction reading. The signal from the sensing coil is also directly fed to the data acquisition system and mathematically converted into magnetic induction. The integrating fluxmeter utilizes the relation given by equation (1.11). The 1018 steel pushrod moves through a linear motion precision bearing which is made of magnetic steel and also helps to create a complete path for the magnetic flux lines between the sample and transducer casing. The entire transducer is placed on a load fixture with a 0.7 in thick aluminum 6061-T6 plate in between. The aluminum plate is used to prevent the magnetic flux lines from diverting towards the fixture which would result in flux leakage. A 0.125 in depression, slightly larger than the diameter of the transducer was milled on the aluminum plate to secure the position of the transducer for precise load alignment.

3.2.3   Magnetic Circuit Calibration

The magnetic field intensity produced by the transducer at maximum drive current was determined employing three different techniques and the effective magnetic field per current was then estimated from the average of the three techniques. The three methods are: (i) low frequency experimental measurements, (ii) magnetostatic finite element analysis and (iii) Montgomery's thick solenoid equation. Magnetodynamic effects were neglected throughout these analyses because the scope of the material characterization is limited to low frequency sinusoidal excitations of 0.1 Hz.

For the experimental determination of the solenoid rating, a Walker Scientific MG-4D Gaussmeter with an HP 245S axial Hall probe was used. Hall probes come in axial and transverse models for measuring axial or transverse fields, respectively. As the name suggests, the Gaussmeter gives a measure of the magnetic induction in units of Gauss of the medium in which the Hall probe is placed though the aim is actually to measure the magnetic field. The fact that the permeability of free space in the CGS units is unity is employed in these measurements. Since $B=\mu_o H$ for free space or air and $\mu_o=1$ in CGS system of units, $B = H$ so the readings in Gauss given by the Gaussmeter would be equivalent to the same number of Oersteds which is the measure of the field. Therefore, all the measurements using the Hall probe were performed without the different internal components of the transducer so that the near ideal environment of just free space would be created.

Two types of measurements were performed with the Hall probe always along the longitudinal axis of the drive solenoid. In the first type of measurements, voltage levels were varied with the Hall probe at different fixed distances from the bottom of the solenoid. In the second type, the voltage was kept constant at different levels and the distance of the probe from the bottom of the solenoid was varied.

Fig. 3.3 shows the field intensity observed along the longitudinal axis at various heights from the bottom of the solenoid at different DC voltage levels and without the top and bottom magnetic steel plates. It is seen that the maximum field intensity is almost at the midpoint along the height of the solenoid and the field decreases at the ends in agreement with the theoretical field intensity behavior of solenoids. The graph on the left is plotted with the actual experimental data and the graph on the right is just the corresponding spline approximation of the same data points. It is noted that

the reference voltages shown represent the output from the data acquisition system which are 60 times smaller than the true voltage across the solenoid. Since the active sample is positioned at the center and midpoint along the height of the solenoid on the longitudinal axis, the rating is calculated based on the intensity at the midpoint rather than considering the distribution along the length that would be occupied by the active sample. It is thus, assumed that the magnetic field strength is constant along the length of the active sample. This is a fairly good approximation as will be seen from the magnetic field distribution curve from the finite element analysis simulation.
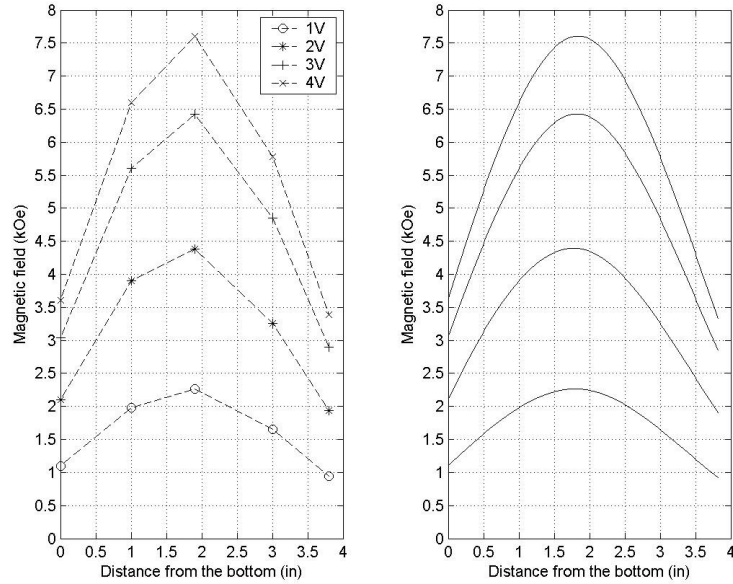
Figure 3.3: Magnetic field at different DC voltage levels along the height of the solenoid.

Fig. 3.4 shows the magnetic field intensity along the longitudinal axis of the solenoid at different heights when a constant DC voltage of 60V (1V output from the data acquisition system) is applied across the coil terminals. In this case, the bottom magnetic steel plate is present. The presence of the steel plate, which has a much higher permeability than air, causes the magnetic flux to concentrate resulting in a higher magnetic induction near the bottom. Comparing Figs. 3.3 and 3.4 for the 1V case (output from the data acquisition system), it is observed that even by introducing just the bottom plate, there is a big improvement in the magnetic induction and correspondingly the magnetic field concentration inside the transducer. Taking the average rating from the four different voltages from Fig. 3.3, a rating of 132.45 Oe/A is obtained at the mid-height of the solenoid and from Fig. 3.4, a rating of 160 Oe/A is obtained. Since in practice both the upper and lower steel plates would be present along with the interior components of the transducer, the true rating would be slightly higher than these values. The FEA gives a rating value that seems more reasonable.

Finite element analysis of the transducer's magnetic circuit was performed using FEMM 3.2, a 2-D specialized freeware package capable of very accurate magneto-static calculations. The analysis performed here considers 2-D axisymmetry about the longitudinal axis of the solenoid. The current density was assigned as the only input in the analysis and was calculated from actual dimensions and input voltage. The maximum current flowing in the solenoid coil is 56 A and the cross sectional area occupied by the coils is 44.6×10^{-4} m^2 which was calculated from the geometry of the coil. The ideal number of turns that could be accommodated was calculated to be 1500 but due to losses arising from uneven packing of the coil and the space taken
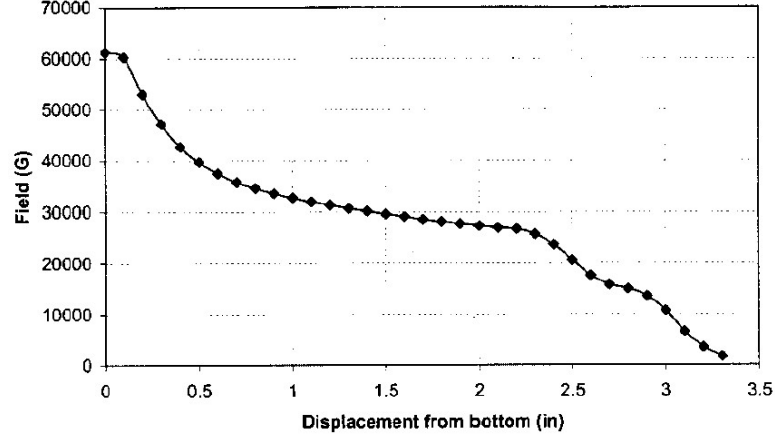
Figure 3.4: Variation of the magnetic induction at different heights from the bottom of the solenoid for 60V true voltage.

up by the wire isolation and epoxy compound, the effective number of turns of the coil was estimated to be 1325. The current density was then calculated by dividing the product of the number of turns and current in each winding by the cross sectional area of the windings. The value of the current density was 16.64 MA/m^2. Since the permeability of Ni-Mn-Ga is not readily available, a specimen of known permeability was placed in the active sample position in the finite element geometry. An AISI 1018 cylindrical sample was used for this purpose since the data for this material was readily available in the software database. Fig. 3.5 shows the magnetic induction and the flux line contours in the transducer when a 0.25 in diameter 2 in long AISI 1018 is substituted in the position of Ni-Mn-Ga and the steel end pieces. The figure shows flux lines bowing away from the longitudinal axis of the transducer which indicates flux leakage. The curved line outside the transducer is the defined boundary beyond which the flux lines are assumed to not escape.
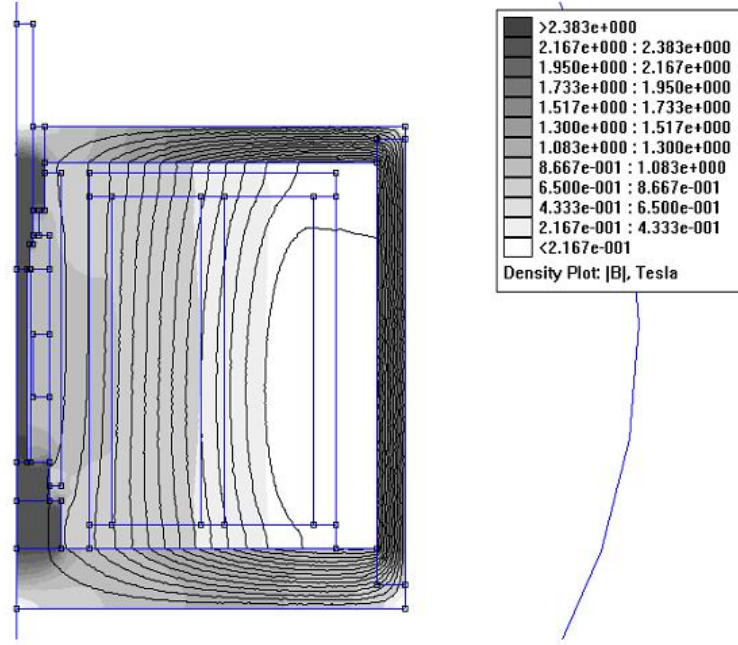
Figure 3.5: 2-D axisymmetric FEA output showing the magnetic flux density distribution and flux line contours in the transducer with AISI 1018 as the test sample.

Fig. 3.6(a) shows the distribution of magnetic field along the length of the AISI 1018 sample. The zero on the x-axis is the bottom of the steel sample and since the total length of the sample is 2 in (5.08 cm), the magnetic field intensity at the midpoint along the length of the steel sample is of primary interest,i.e., at 2.54 cm. Since the actual Ni-Mn-Ga samples are only an inch (2.54cm) long, constant magnetic field along the length of the sample is assumed. With this assumption, a value of 175 Oe/A for field per current rating of the coil is obtained. Fig. 3.6(b) shows software output representing the variation of magnetic flux density along the length of the 1018 steel specimen.

76

Figure 3.6: 2-D axisymmetric FEA calculation of (a) magnetic flux density and (b) magnetic field intensity along the the centerline of the AISI 1018 sample.

In order to test the consistency of the field per current rating of the solenoid, a different material with a known permeability and saturation magnetization was chosen for the simulation. The simulation with AISI 1018 rod was done with maximum current flowing through the solenoid because steel saturates at a field of about 300 kA/m. Vanadium permendur reaches saturation at about 2.39 T and in a field strength of 79 kA/m, so the second simulation was performed by placing a rod of vanadium permendur of the same size in the active sample position. A current density corresponding to a current one twelfth of the maximum current (56 A) was assigned to the solenoid cross sectional geometry so that the applied field would produce an induction in the material with about the same magnitude as its saturation induction.

From Fig. 3.7, it is seen that due to less current flowing through the solenoid, the AISI 1018 parts are not saturated but the vanadium permendur part is saturated. The flux lines do not bow away from the longitudinal axis of the solenoid as much as

in the case of AISI 1018 because the relative permeability of vanadium is about 6856 and and that of AISI 1018 is about 529. The high relative permeability of vanadium permendur attracts more flux lines towards it and hence more induction for the same magnitude of the field. Figs. 3.8(a)-(b) show the variation of the magnetic induction and field along the length of the sample respectively. Again we observe the values at the middle of the sample length which gives field per current rating of about 188 Oe/A.
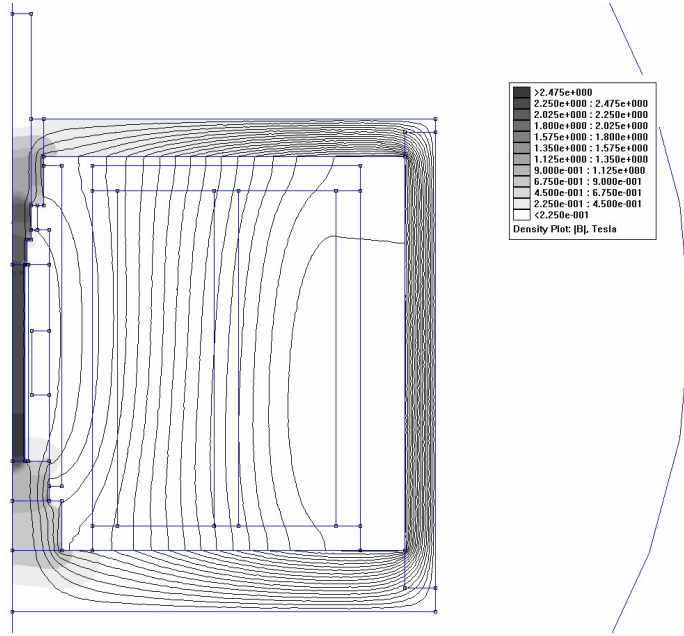
Figure 3.7: 2-D axisymmetric FEA output showing the magnetic flux density distribution and flux line contours in the transducer with vanadium permendur as the test sample.

Finally, the equation for a thick solenoid coil given by Montgomery [14] was also employed to estimate the field per current rating of the solenoid. Equation (1.3)
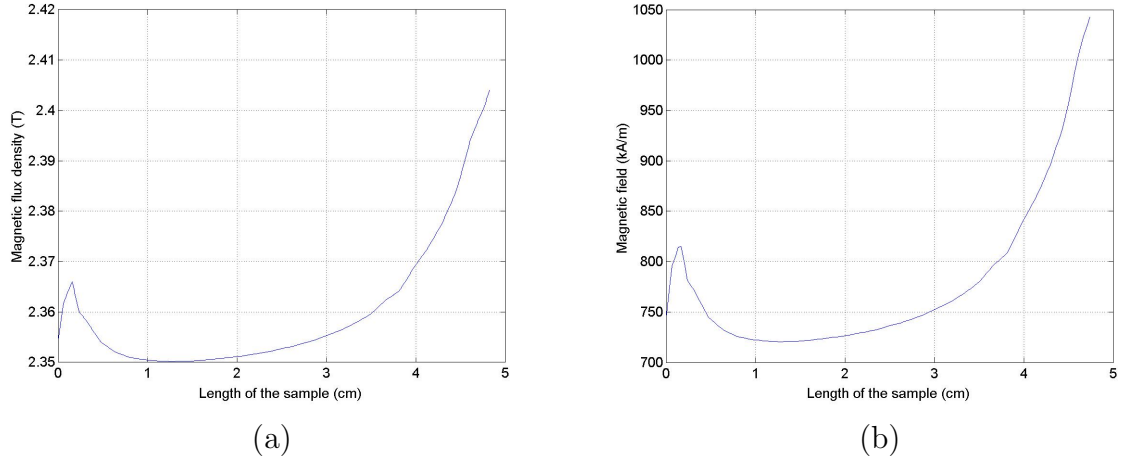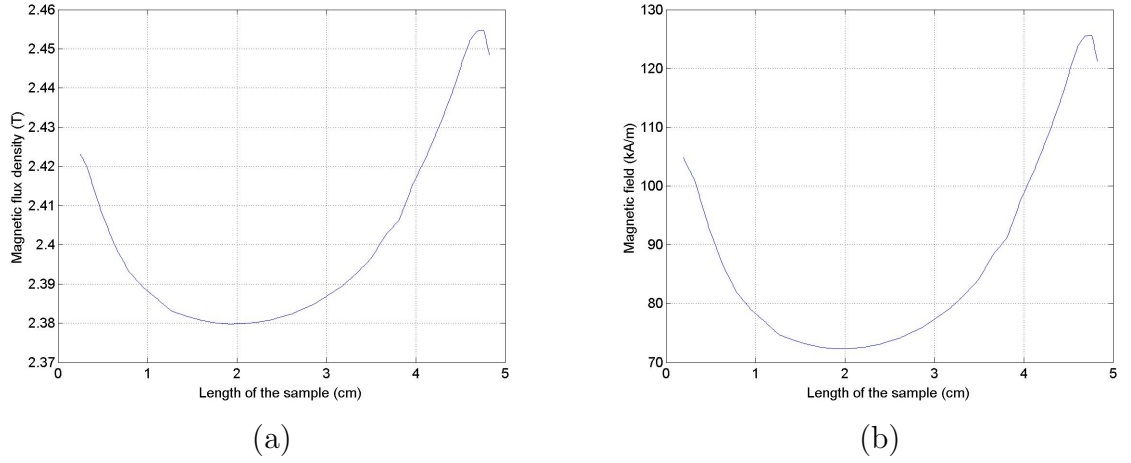
Figure 3.8: 2-D axisymmetric FEA calculation of (a) magnetic flux density and (b) magnetic field intensity along the the centerline of vanadium permendur sample.

incorporates the geometrical features of the solenoid and gives the field at the center of the solenoid. For r_1= 1.06 in, r_2= 3.3 in, L= 3.4 in, i= 56 A and N= 1325, equations (1.1)-(1.5) give H_o=160 Oe/A. It should be noted that this method does not take into account the material properties at the center of the solenoid. The field per current rating of the coil should be higher than this value due to the presence of the various magnetic steel components at the center of the transducer. With the results from all the different methods of solenoid field calibration, a field per current rating of 167 Oe/A was chosen to comply with the different results.

3.3 Loading Fixture

For quasi-static testing with dead weights, a stable fixture with an almost point load application arrangement was necessary to avoid any bending moments on the sample. Since the tests were conducted at very low frequencies but large loads, a

Calibration technique	Rating (Oe/A)	Used rating (Oe/A)
Hall probe (constant voltages varying height)	132.45	
Hall probe (60 V input varying height)	160	
FEA with AISI 1018 rod	175	167
FEA with vanadium permendur	188	
Solenoid geometry equations	160	

Table 3.4: Field per current rating values obtained from different methods and the used rating value.

loading beam arrangement was opted for the application of stress on the sample. The fixture is a table-like structure constructed entirely with Unistrut channels (Fig. 3.1). The fixture was designed to supply loads up to 1500 lbs and was bolted to the floor. The load fixture basically employs a hanging weight arrangement that is centered on the structure. The top and bottom loading bars are made of 1018 steel with Unistrut channels welded on the sides to enhance the section modulus of the bars. The two bars are connected with two 1018 steel rods that are threaded at the ends so that they can be tightened with nuts after engaging them with the two bars. The two steel rods pass through two linear motion precision bearings on each side to prevent the generation of undesired moments on the sample which may arise from the tilting of the loading bars. The two linear motion bearings are supported inside steel block housings that are adjustable along the width of the table. Further, with a considerable length of the two rods threaded at the ends, the distance between the bars may be adjusted. Additional constructive details are provided in Appendix B.

3.3.1 Column Design

The main design considerations for load were involved in the loading bars, the threaded rods connecting the upper and lower loading bars, the load distributor, the eye bolts and the threaded connectors. The P1000 Unistrut channels were used almost entirely in the structure along with a few P3000 channels at positions where strength was not a serious issue. Unistrut channels were used because of the readily available data on beam and column loading.
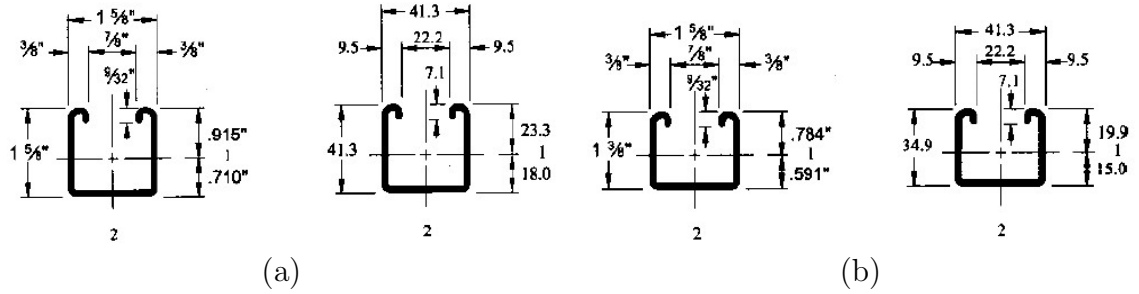
Figure 3.9: (a) Section dimensions of P1000 channel in inches(left) and centimeters (right) (b) Section dimensions of P3000 channel in inches(left) and centimeters (right).

Channel	Section area		Axis 1-1				Axis 2-2			
			I		S		I		S	
	in^2	cm^2	in^4	cm^4	in^3	cm^3	in^4	cm^4	in^3	cm^3
P1000	0.556	3.6	0.185	7.7	0.202	3.3	0.236	9.8	0.290	4.7
P3000	0.504	3.25	0.12	5	0.154	2.52	0.204	8.5	0.253	4.15

Table 3.5: Section properties of Unistrut channels.

Table 3.5 gives the values of some important parameters of P1000 and P3000 that were used for the design of the fixture. Since the aim was to load the active samples up to 1000 lbs, there were two starting design considerations: (1) the height of the loading fixture to provide adequate space for the loading trays and (2) avoid buckling of the fixture. The compressive stress due to a load P on a column of cross sectional area A is,

$$\sigma = \frac{P}{A} \tag{3.1}$$

The height of each leg of the fixture was chosen to be 50 in and the the critical load was calculated. The critical load is the load at which a column fails by buckling and can be well below the yield stress of the material. The slenderness ratio of a column plays a very important role in the calculation of the critical load. It is given by,

$$S_r = \frac{l}{k} \tag{3.2}$$

where l is the length of the column and k is the radius of gyration. For a short column, $S_r < 10$. The radius of gyration k is defined as,

$$k = \sqrt{\frac{I}{A}} \tag{3.3}$$

where I is the smallest area moment of inertia (second moment of area) of the column cross section (about any neutral axis) and A is the area at the same cross section. The Euler-column formula for the critical load is,

$$P_{cr} = \frac{\pi^2 EI}{l_{eff}^2} \tag{3.4}$$

where E is the Young's modulus of the material. Using equations (3.2) and (3.4), the critical unit load may be expressed as,

$$\frac{P_{cr}}{A} = \frac{\pi^2 EA}{S_r^2} \tag{3.5}$$

Fig. 3.10 shows the column failure lines in which equations (3.1) and (3.5) have been plotted against the slenderness ratio. The compressive yield strength of the material S_{yc} is used as the value for σ in equation (3.1) and the critical unit load from equation (3.5) is plotted on the same axis as the material strength. The envelope OABCO seemed to be a safe region for column unit loads, however, experiments demonstrated that columns often failed in the loading region ABDA near the intersection B of the two curves. A parabolic curve was fitted between point A and tangent point D which is the intersection of the Euler curve (equation (3.5)) and a horizontal line at $S_{yc}/2$. The slenderness ratio $(S_r)_D$ at point D is given by,

$$(S_r)_D = \pi \sqrt{\frac{2E}{S_{yc}}} \tag{3.6}$$

The equation of the parabola between points A and D is,

$$\frac{P_{cr}}{A} = S_y - \frac{1}{E}\left[\frac{S_y S_r}{2\pi}\right]^2 \tag{3.7}$$

If $(S_r)_D \geq S_r$, equation (3.5) is used otherwise equation (3.7) is used. For the P1000 free-fixed channels, $l_{eff} = 2.1l$, k=1.5 cm and S_r=181.98. $(S_r)_D$=127.7 using the value for tensile yield stress S_{yt} instead of compressive yield stress S_{yc}. The value for $(S_r)_D$ would be even smaller if S_{yc} is used since $S_{yc} > S_{yt}$. So, $S_r > (S_r)_D$. Therefore, using equation (3.4) with E=200 GPa and I=7.7$\times 10^{-8}$ m^2 (smallest area moment of inertia is the one about axis 1-1) from Table 3.5, taking a factor of safety of 2, P_{cr}=2398.5 lbs.

From the column loading data (see Appendix C) it was seen that a P1000 column could withstand loads upto 2500 lbs when loaded at the slot face which closely agrees with the value calculated. The choice for the height of the channel was safe because
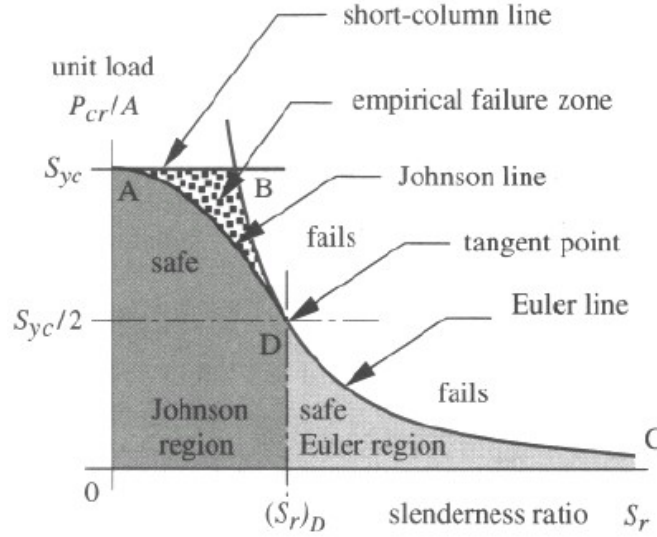
Figure 3.10: Construction of column failure lines [16].

each leg would be subjected to only 250 lbs when a total load of 1000 lbs would be applied.

3.3.2 Connecting Rods and Thread Design

The connecting rods linking the upper and lower loading bars were also designed for 1000 lbs. The two connecting rods are threaded at the ends so that they sit in the holes of the upper and lower loading bars. The two connecting bars are held in position with the loading bars with appropriate nuts. Since the two connecting rods would always be in tension when loaded, design considerations were performed with the tensile strength data. The tensile stress in any specimen is also given by equation (3.1) where P is now the tensile force applied and A is the cross sectional area of the specimen. A constraint was selected for the principal stress σ_1 to not exceed one fourth the value of tensile yield stress S_{yt}. With S_{yt}=360 Mpa for AISI 1018,

84

the factor of safety is $N=S_{yt}/\sigma_1=4$ resulting in $\sigma_1=128.67$ MPa. Substituting this value of σ_1 in equation (3.1), we get diameter $d=0.30$ in. Therefore, two connecting rods of diameter 0.5 in were chosen. The next step was to design the threads on the connecting rods which would be subjected to shear load. One possible shear-failure mode involves stripping of threads out of the nut or off the screw which is dependant on the relative strengths of the nut and screw materials. If the nut material is weaker, it may strip its threads at its major diameter and if the screw is weaker then it may strip its threads at the minor diameter. If both the nut and screw are of the same material, then thread stripping may occur at the pitch diameter. Here, we will assume that the load is shared equally among the threads of the connecting rods for a total load of 1000 lbs. The stripping area for A_s for one screw thread is the area of the cylinder of its minor diameter d_r which is given by,

$$A_s = \pi d_r w_i p \tag{3.8}$$

where p is the thread pitch and w_i is the factor that defines the percentage of the pitch occupied by the metal at the minor diameter. A similar equation can be written for the stripping area of a single thread of a nut at its major diameter d.

$$A_s = \pi d w_o p \tag{3.9}$$

where w_o is a similar factor as w_i but for the major diameter.

The values for w_i and w_o are set by the United National Standard (UNS) screw threads. For a 0.5-13 UNC screw threads, $w_i=0.8$, $d_r=0.4001$ in, $p=0.07692$ in. This gives a stripping area $A_s=0.0775$ in^2 and a shear stress $\tau_s = P/2A_s=44.63$ MPa on one thread. If three nuts of effective height 0.43 in are engaged, total screw threads engaged would be $13\times0.43\times3\approx17$. The total strip area would be multiplied by 17 and,

85

therefore, τ_s=2.63 MPa which is a low and safe working value. A similar calculation can be performed with the nut threads except with w_o=0.88 and d=0.5 in. For the engagement of 17 threads, τ_s=0.955 MPa which is also a safe working value.

3.3.3 Loading Beam Design

The upper and lower loading beams are the most important structures in the fixture which demand minimum bending and deflection to prevent the two connecting rods at its ends from moving closer toward the center. If the two connecting rods move closer to one another due to the bending of the beams, they exert extra force on the linear motion guide bearings which results in bearing damage and a smooth vertical motion would not exist from the active sample strain. This situation would also give rise to an opposing force on the movement of the active sample. Simple schematics for the loading on the upper and lower beams have been illustrated in Fig. 3.11(a) and (b) respectively.
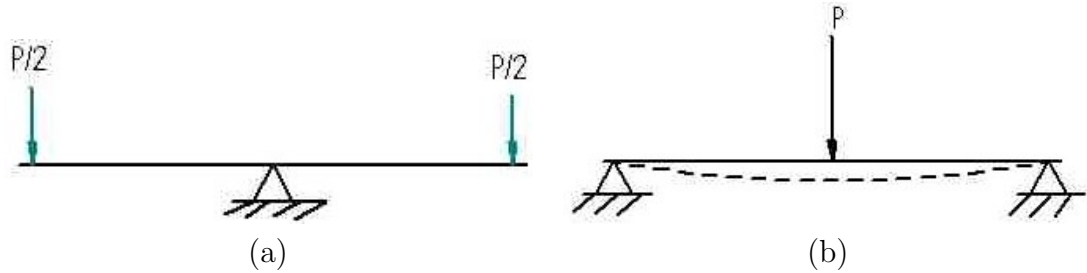

Figure 3.11: (a) Schematic of upper loading beam (b) Schematic of lower loading beam .

The upper beam can be thought of as a combination of two cantilever beams on either side. An assumption is made that a plane in the cross section of the beam

exists at the point of support which acts as if it were fixed to a rigid support. The bending stress for any beam is given by,

$$\sigma = \frac{My}{I} \tag{3.10}$$

where M is the moment along the length of the beam, y is the distance measured perpendicular to the neutral axis toward the edges of the beam and I is the area moment of inertia about the neutral axis. The length L for the beams is taken as the distance between the two 0.5 in diameter holes that are 20.375 in apart.
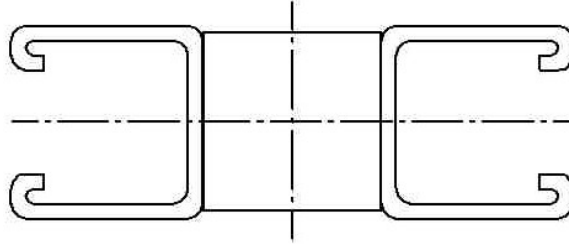

Figure 3.12: Cross section of the upper and lower loading beams.

Fig. 3.12 shows the cross section of the loading beams. The neutral axis is the horizontal axis or the axis 2-2 for the P1000 channels. For both the upper and lower loading beams, the maximum bending moment would occur at the midpoint along the length of the bar at the top (tension) and bottom(compression) edges. The moment at the midpoint along the length is given by $M=(P/2)\times0.5L=288.17$ Nm, y=0.02m and $I=2\times(I$ of each P1000 channel about axis 2-2)+(I of the square cross section bar)=0.371×10^{-6}. Using equation (3.10), we get σ_{max}=16.03 Mpa. The end deflection δ can be computed from $\delta=PL^3/24EI$=0.17 mm. The actual deflection

would be slightly more than this value due to the holes present in the beams and the stress concentration factor due to the small hole at the center has not been considered.

The bending stress analysis for the lower beam would be similar to the upper beam except that the bending stress value would be increased by the stress concentration factor for the hole of diameter 0.4375 in at the midpoint of the beam. For the lower loading beam, h=1.5 in and d/h=0.292 which would give a stress concentration factor $K_t \cong Ae^{[b(d/w)]}$=2.16 using Fig. 3.13. The maximum bending stress for the lower loading beam is then σ_{max}=34.6 Mpa.
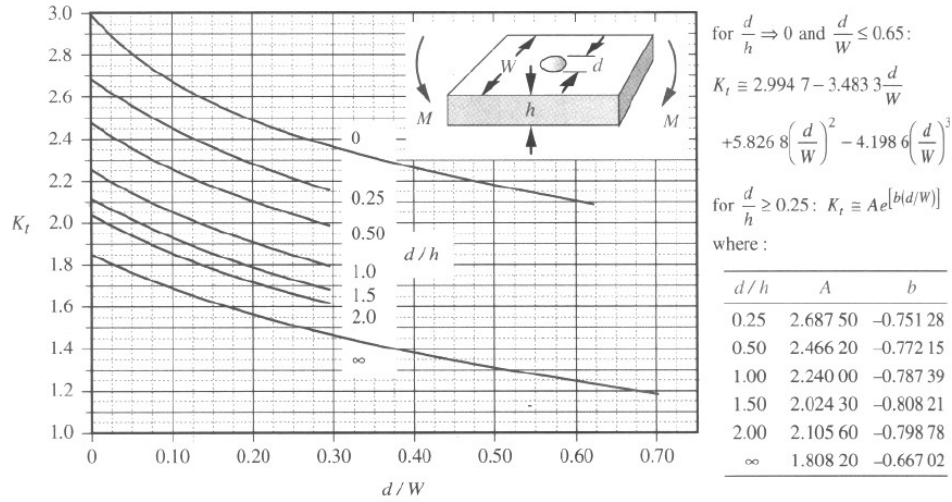

Figure 3.13: Geometric stress concentration factor K_t for a bar with transverse hole in bending [16].

A complete ANSYS analysis was also performed on the two loading beams for the deflection and Von-Mises stress which is included in Appendix D. A comparison is made between the single square section bar and the same bar with the P1000 channels

attached to the sides for a total applied load of 1000 lbs. We see that the design is highly improved with the addition of the C channels.

3.3.4   Load Distributor Design

The flat circular load distributor was designed using ANSYS (see Appendix D) by monitoring the Von-Mises stress, the total vertical deflection and the change in shape. The four chained links of threaded connectors run at an angle of about 45° to the vertical from the load distributor. Since the holes on the load distributor were drilled perpendicular to the surface of the distributor, the contact area between each threaded connector and the distributor is very small and can be taken as almost a point contact. Therefore, a point force was assumed at these contact areas. The ANSYS analysis shows high stress areas at the small contact points but the rest of the area is in the safe region. The vertical deflection is also very small with little change in shape.

3.3.5   Eye bolts, Threaded Connectors and Weights

The eyebolts are the main connecting devices between the loading beams and the loading trays. Two eyebolts were used, one on the lower loading beam and the other on the load distributor. The eye bolts were chosen based on the load bearing capacity information which was readily available on the manufacturer's product specification sheet. The two shoulder pattern eyebolts are made of forged steel with a maximum load capacity of 1800 lbs when the threaded shank length of 1.38 lbs is fully engaged. The threaded connectors were also chosen according to the maximum load bearing capacity. All threaded connectors are 0.25 in in diameter with a maximum load capacity of 880 lbs except the one connecting the two eyebolts which is 0.375 in with

a maximum load capacity of 2200 lbs. This big threaded connector is subjected to the total load that is applied. The specifications for the eyebolts and the threaded connectors are given in Appendix C.

The load is applied in the form of lead blocks each with dimensions 7.25"×4"×2" and weighing about 24 lbs. The lead bricks were made from molten lead cast in ingots. The lead bricks were placed on loading trays with each loading tray accomodating up to 300 lbs. The first loading tray is connected to the load distributor through a link of threaded connectors at 45° to the vertical and to the lower trays with threaded connectors welded to the sides of the trays.

3.3.6   Arm Arrangement for 0-50 lbs Loading

The main loading fixture cannot be used for loading between 0-50 lbs due to the weight of the loading beam arrangement which is itself almost 50 lbs. In order to know the exact behavior of the samples under loading, strain and magnetization data were necessary for lower loads also. Testing the samples at low loads would provide the twinning region for strain which is an important parameter that could provide an answer to the magnitude of strain produced.

The loading arm arrangement consists of a simply supported beam resting on a fulcrum at one end and on a steel ball at the other end which is placed on top of the push rod. The purpose of the steel ball is to create a point contact for the applied stress and prevent the generation of any moments on the sample. The fulcrum arrangement with a wedge support at the other end provides a line contact and reduces the friction forces which may otherwise be considerable if ball bearings were to be used. The height of the arm arrangement is adjustable for incorporating a force

transducer in between the pushrod and the arm. An addition was made to the simple loading arm arrangement for the constant bias voltage with the addition of a bolt and belleville spring washers. The belleville spring washers were used as the main force generating components with the bolt providing the compression on the sample. The belleville washers were placed at the midpoint along the length of the loading arm so that approximately half the force applied on the bolt at the center was transmitted to the active sample.

3.4 Additional Instrumentation, Amplifiers and Data Acquisition

A 208C04 ICP type PCB Piezotronics force transducer is screwed at the center of the bottom surface of the top loading beam and a non-magnetic stainless steel piece acts as a coupler between the pushrod and the loading arrangement. A 484B11 single channel signal conditioner is used with the force transducer. The load fixture comprises an extended platform which is used for supporting the instruments used for the tests. The strain in the active samples was measured with a Schaevitz MHR025 LVDT with a sensitivity of 1.26 V/mils with the core placed on the top surface of the midpoint of the top loading beam. A separate support was made for the LVDT from aluminum 6061-T6 blocks that was placed on a linear precision slider stage. The LVDT is connected to the LVDT circuit board and the position of the core is adjusted using the voltage reading from an Agilent 34401A multimeter. The LVDT stage is fixed on the top surface of the transducer with a flat piece of aluminum plate in between to prevent the leakage of magnetic flux.

The transducer was driven with two 4 kW Techron 7790 amplifiers arranged in series that produced an overall average voltage gain of 60 with a maximum current

of 56 A flowing in the transducer circuit at the rated solenoid resistance of 3.7 Ω. The two amplifiers, with the nomenclature as "master" and "slave" can be connected in either the current control mode or the voltage control mode. A heavy duty lever switch was employed to switch the main power supply for the amplifiers.

Data acquisition was accomplished using a Data Physics DAQ board with Dynamic Mobilizer software running on a PC. Due to the noise in the system, low sampling rate was used and the tests at 0.1 Hz were run for a time window of 25.166 seconds to get a significant wavelength of the periodic signal.

CHAPTER 4

RESULTS

4.1 Introduction

The Ni-Mn-Ga samples employed in this study (see Section 3.1 for composition specifications) were tested under sinusoidal magnetic fields of frequency 0.1 Hz and various loading conditions from almost zero load up to blocking loads. Magnetic and mechanical measurements include magnetic induction and strain, from which various magnetic and magneto-mechanical properties were calculated. Since the transducer is made of ferromagnetic materials and therefore, exhibits magnetostriction effects, magnetostriction data on AISI 1144 steel is presented first. For purposes of contrasting the magnetoelastic behavior of Ni-Mn-Ga with a conventional ferromagnetic material, strain and magnetization data for nickel 200 is provided as well.

4.2 Data Processing

A few points need to be explained beforehand in order to avoid ambiguity regarding the figures presented in the results. The field-induced strain curves plotted against the field values are the reversible strains which have been obtained after excluding the first cycle of the sinusoidal current signal and the corresponding portion

of the strain signal from the LVDT. Since the summing circuit used to nullify the DC offset of the output signal from the DAC inverts the signal, the final signal is inverted with respect to the the one generated by the DAC system. Hence, after excluding the first cycle of the current signal, the remaining signal still starts with a negative half cycle. All the figures with cyclic field plots (microstrain vs field and magnetization vs field) have been plotted using a single current cycle after excluding the first cycle. Another point to be noted is that in all the strain vs field graphs, the portion of the curve in the negative region of the field shows slightly more strain than the one in the positive region of the field. This is not due to the material behavior but due to the Joule heating of the solenoid. When a peak voltage of 3.5V is output from the DAC system, the gain (60) of the amplifiers creates a voltage of 210V across the terminals of the solenoid and since each test is run for about 25 seconds, a considerable amount of heating occurs in the solenoid. The heat increases the resistance of the solenoid copper wires which decreases the current and hence, a smaller field is produced. Since more heating occurs in the second half cycle of the sinusoidal field, the peak field value is lower and lesser strain is produced. The decrease in field follows an exponential envelope.

The tests under load were carried out using the loading fixture for loads greater than 50 lbs and the loading arm for loads between 0 and 50 lbs. When using the loading arm with the belleville washers, the sample does not experience constant force due to the cyclic contraction of the sample in the cyclic field. The force acting on the sample decreases as it contracts and returns to the starting value when the sample gains its original length. In the figures showing the maximum strain versus applied stress, a slight off-trend feature is seen in the strain decay between 0-50 lbs

(0-7.03 MPa) and that above 50 lbs. This is because of the points being plotted against the initial force values which are not exactly the true force values during the actuation of the sample as explained above.

4.3 AISI 1144 Steel Experimental Results

Magnetic steel is known to exhibit appreciable amount of magnetostriction though very small as compared to the field-induced strain produced by the Ni-Mn-Ga samples. Therefore, to get an accurate measure of the field-induced strain produced by the Ni-Mn-Ga samples, the magnetostriction of steel has to be subtracted for each loaded as well as unloaded test. Besides the magnetostriction of the end steel pieces, there would be some magnetostriction due to all the magnetic steel components present in the path of the magnetic flux, i.e, from the magnetostriction of the bottom plate, magnetic base, bottom cap and the push rod. An aluminum 6061-T6 sample of the same size as the Ni-Mn-Ga samples was positioned inside the transducer in the same way as the active samples and tests were run for the same magnitude of the magnetic field, loaded and unloaded conditions. Aluminum 6061-T6 being non-magnetic, does not produce any magnetostriction and the strain produced is entirely due to the magnetostriction of magnetic steel components in the transducer. This strain is then subtracted from the strain obtained with the active sample in position (with the steel end pieces).

Fig. 4.1 shows the magnetostriction observed in the magnetic steel components of the transducer including the end pieces with the aluminum piece in place of the Ni-Mn-Ga samples. The total effective length of the steel components was taken as the sum of the length of the two end pieces and half the length of the pushrod inside
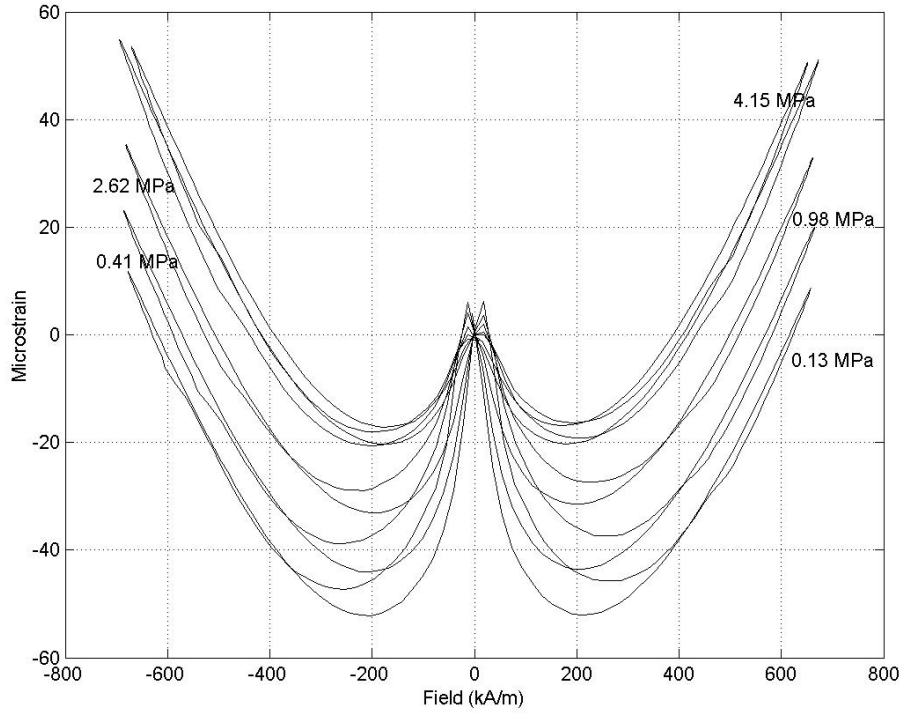
Figure 4.1: Magnetostriction of steel end pieces and other magnetic steel components in the transducer at 0.1 Hz.

the transducer (since the entire length of the pushrod in the transducer would not be subjected to the maximum field strength). Steel extends at low fields, undergoes contraction as the field is increased and at higher fields, starts extending again. The tendency of steel to extend again at higher fields affects the strain versus field curves of the active sample at the point of peak magnetic field. Another interesting feature to note is that as the load is increased, steel tries to extend more instead of contracting. The typical "W" shape for steel magnetostriction is clearly seen in the figure. Generally, the magnetostriction of steel decreases with increase in carbon content.

The subtraction of steel magnetostriction from the sample data must be done carefully by making a basis for subtraction, i.e. level the strain curve of the sample and that of steel on the same reference. For this purpose, the point at which the sinusoidal current is zero is considered. The same point is then located in the time trace of strain for steel and the active sample. This point is then set as the zero for both the curves and the subtraction is performed. The idea for this method of subtraction is based on the fact that the strain curve for the steel components must fit in the strain curve for the active sample when positioned in the transducer.

4.4   Nickel 200 Experimental Results

A few tests were also run with a 2 in long 0.25 in diameter nickel 200 rod. Nickel 200 is one of the purest forms of nickel and the nickel that is used in the manufacture of the Ni-Mn-Ga samples is about 99.99% pure. Thus, it would be relevant to include the magnetostriction of nickel 200.

Nickel produces negative magnetostriction [1] which means that the application of magnetic field causes it to contract along its length and the strain saturates at low fields. From Fig. 4.2, it is seen that the strain saturation occurs at about about 62 ppm. This is obtained with a current of about 20.3 A flowing through the solenoid at a corresponding field of about 269.78 kA/m

The magnetization curve in Fig. 4.3 shows that saturation is close to 260 kA/m which is typical for nickel at a field value of about 225 kA/m. The magnetization curve shown above is for a current of 16.22 A flowing through the solenoid. The basic idea of presenting the data for nickel is to show that even though nickel is weakly magnetostrictive and gallium and manganese are not magnetostrictive at all, a proper
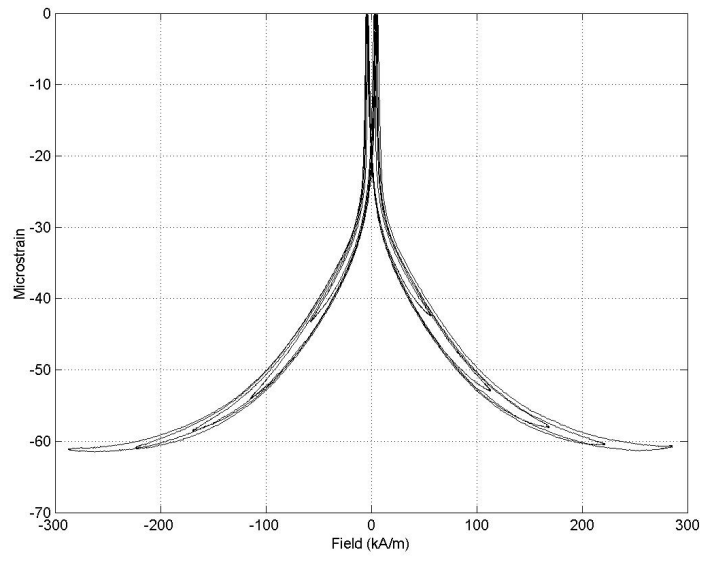
Figure 4.2: Magnetostriction of Ni 200 at 0.1 Hz different amplitude sinusoidal fields.
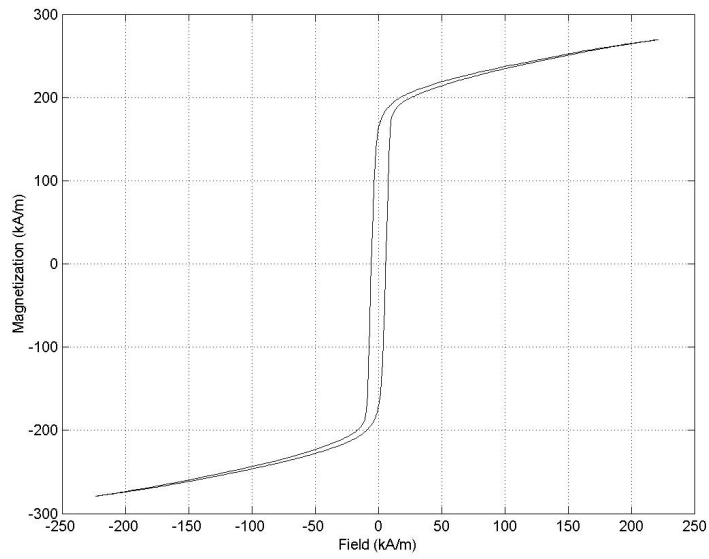

Figure 4.3: Magnetization of Ni 200 at 0.1 Hz sinusoidal field.

98

composition of these three elements can initiate a crystal structure with completely different magnetic and mechanical properties producing large field-induced strains.

4.5 Ni-Mn-Ga Experimental Results

The off-stoichiometric Ni-Mn-Ga samples were tested under quasistatic magnetic fields primarily at 0.1 Hz. As mentioned in Section 1.1, the samples were activated using a collinear compressive stress and field as opposed to the conventional drive configuration of orthogonal compressive stress-field pair. The collinear drive configuration is shown again in Fig. 4.4. It was observed that with the collinear compressive stress-field pair, the strain produced in the samples was negative, i.e., the samples contracted on the application of magnetic field. The strain is produced in a single direction (always negative) with respect to the original length unlike in materials such as electrostrictives which may show both positive and negative (up to some extent depending on the amount of pre-poling) strain. All the samples were tested as cast
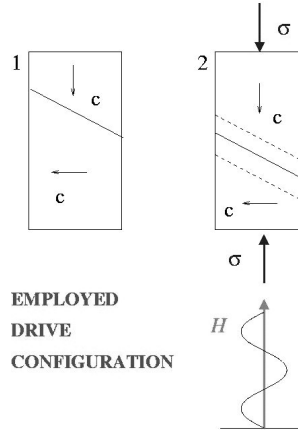
Figure 4.4: Solenoid based drive configuration.

without any prior "training" through field cycling or thermal treatments. Mechanical training is usually the standard procedure adopted before the testing of these shape memory alloys.

4.5.1 Results for dls-1-136-1

The dls-1-136-1 sample is the sample that produced the highest field-induced strain. The sample produced a negative strain of 6379 ppm under zero load (only the pushrod which weighed 39 g) at a peak field of 8.1 kOe (650 kA/m). Fig. 4.5 shows the curve obtained by plotting strain against the sinusoidal magnetic field. It is seen that the sample contracts when activated by a magnetic field and the strain produced by the sample is in a single direction with respect to the original length, i.e., for both the positive and negative half cycles of the magnetic field, only negative strain is observed.

The crossover point occurs at 855 ppm which is the point corresponding to zero magnetic field. The existence of the crossover point may be partly due to the magnetic remanence of the sample which sustains a certain magnitude of strain even when the field is zero. However, more complicated effects related to twin boundary motion relaxation may be possible. The strain and field share a largely non-linear relation at higher fields but is almost linear at low fields. The piezomagnetic coefficient d_{33} was calculated at increasing and decreasing fields and the maximum values obtained were 2.7114×10^{-7} m/A and 7×10^{-8} m/A. So there is more strain per field when the field is increasing than when the field is decreasing. The maximum value for d_{33} in the increasing field is obtained near the point of zero field. This can be observed in Fig. 4.6. When the field increases, d_{33} first decreases as the point of zero strain is
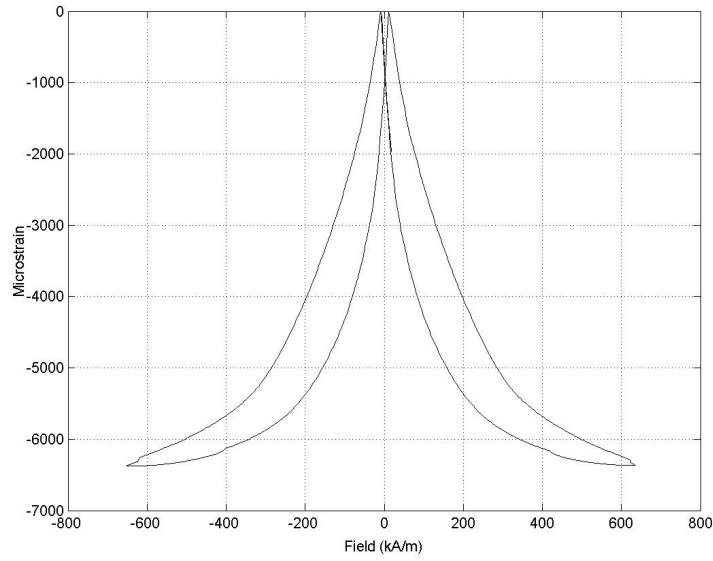
Figure 4.5: Strain vs magnetic field curve for dls-1-136-1 at zero load and 0.1 Hz.

approached and after the point of zero strain, it increases and then finally approaches zero at the point of strain saturation.

Fig. 4.7 shows the magnetization plotted against the field. The magnetization is seen to saturate at about 381 kA/m (48.31 emu/gm) which is the highest amont the samples tested. The coercive field is also very low at about 8.83 kA/m and the remanent field is about 183.03 kA/m (0.23 T). The maximum differential permeability was found to be 38.16 from the induction versus field curves.

Fig. 4.8 compares the strain curves produced from tests conducted at three different low frequencies 0.1, 0.5 and 1 Hz. A very clear increase in the crossover point is seen with the increase in frequency. The increase in the crossover point with increase in frequency besides being due to just increasing remanence, may also be due to the

101
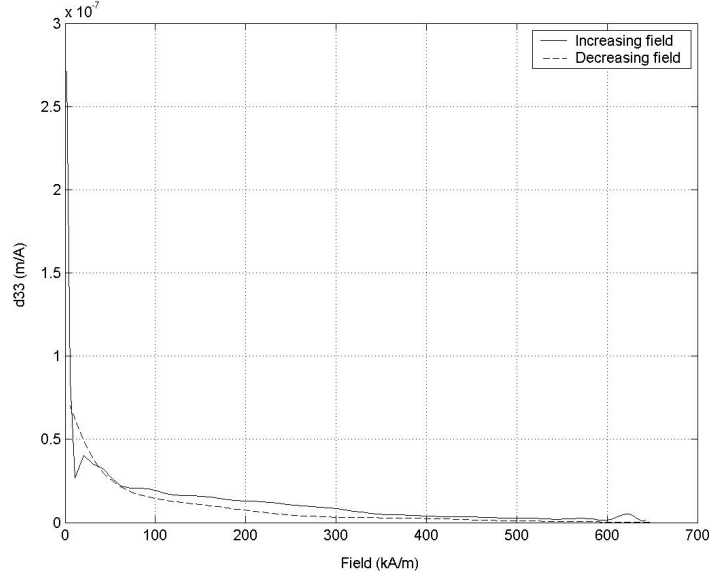
Figure 4.6: Variation of piezomagnetic coefficient d_{33} with magnetic field for dls-1-136-1 at zero load and 0.1 Hz field.

frequency dependant relaxation of the twin boundary motion. The increase in rema-nence implies greater sustained magnetization and hence, larger sustained strain at zero field. At each frequency the maximum d_{33} has a greater value in increasing field than in decreasing field. The increase in coercive field can also be observed with the increase in field.

The magnetization curves in Fig. 4.9 also show a prominent difference with in-crease in frequency. The remanence and coercivity increase with frequency increasing the total hysteresis. The magnetic loss, therefore, increases with frequency. Tests were conducted on the dls-1-136-1 sample at various loads up to 414 lbs (58.23 MPa)
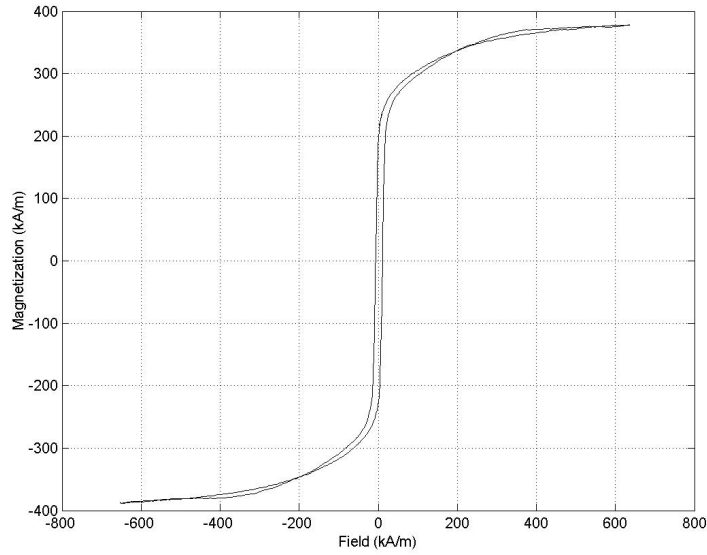
Figure 4.7: Magnetization vs magnetic field curve for dls-1-136-1 at zero load and 0.1 Hz.

to see the effect on field-induced strain. Sinusoidal magnetic field of 0.1 Hz and amplitude 8.1 kOe was applied to the sample at each load. The results are shown in Figs. 4.10 and 4.11.

The strain is seen to be very sensitive to load and decreases drastically with increase in load. The first applied load is 0.9 lbs (0.13 MPa) and the strain produced is 3290 ppm which is almost half of the value at zero load, i.e, 6379 ppm. This shows that the work producing capacity of this sample is very low. Data was also collected for magnetization at different loads but the change in magnetization was insignificant with the change in applied load as illustrated in Fig. 4.12. This seemingly contradicts the law of approach of anhysteretic magnetization [9] observed in ferromagnetic materials under increasing compressive or tensile stress.
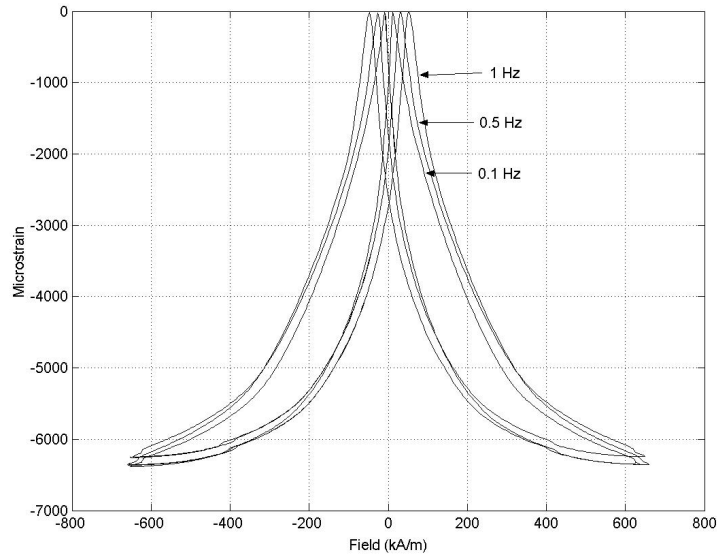
Figure 4.8: Strain vs magnetic field curves for dls-1-136-1 at 0.1, 0.5 and 1 Hz under zero load.
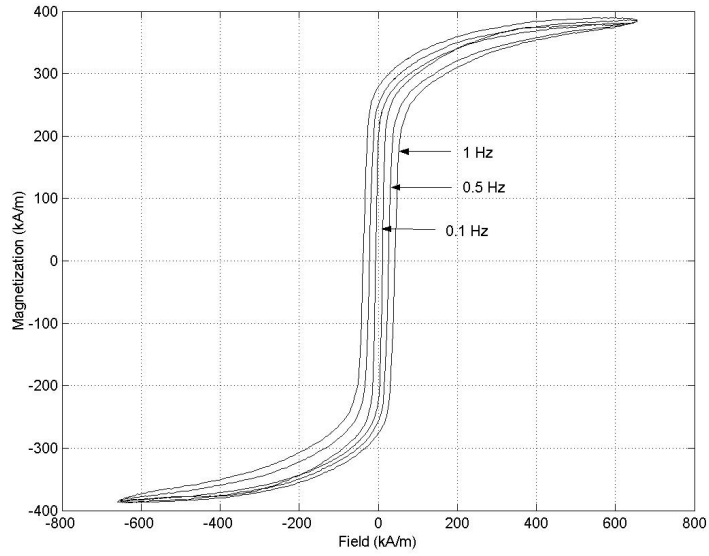
Figure 4.9: Magnetization vs magnetic field curves for dls-1-136-1 at 0.1, 0.5 and 1 Hz under zero load.
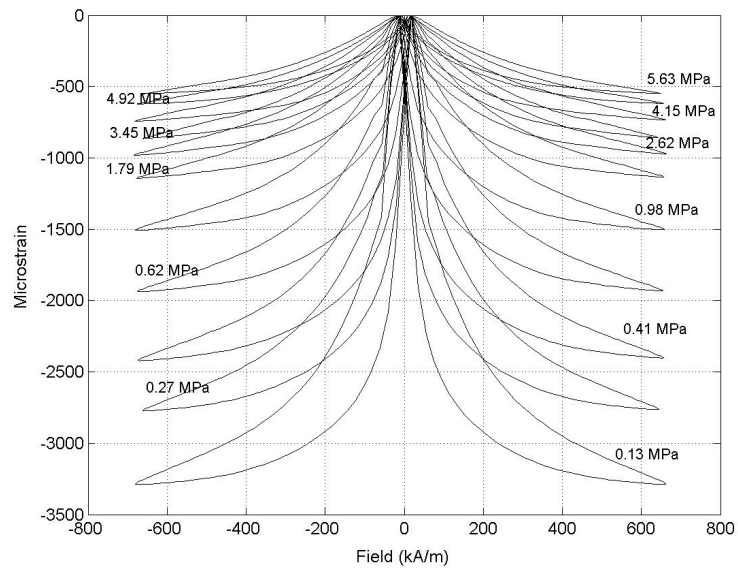
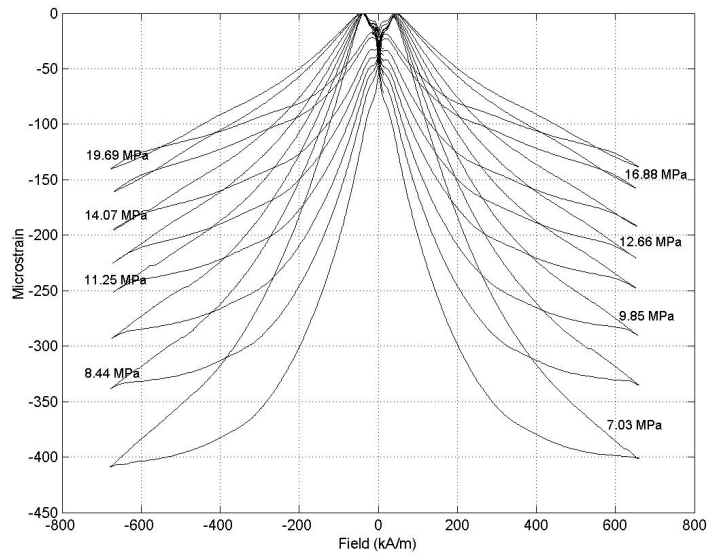Figure 4.10: Strain vs magnetic field curves for dls-1-136-1 at 0.1 Hz and different loads up to 40 lbs.

Figure 4.11: Strain vs magnetic field curve for dls-1-136-1 at 0.1 Hz and different loads starting from 50 lbs.
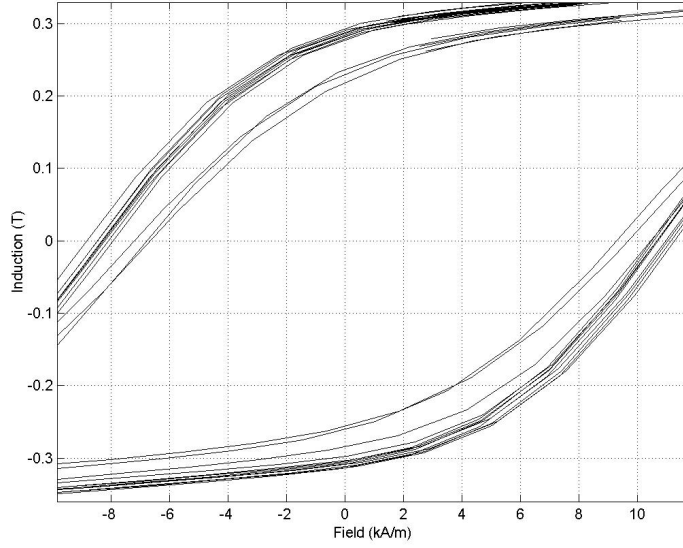
Figure 4.12: Magnetization curves for dls-1-136-1 at 0.1 Hz magnetic field under different loads.

The maximum value of d_{33} at each applied stress is shown in Fig. 4.13 for both increasing and decreasing fields. Maximum value of d_{33} occurs at zero applied stress for both increasing and decreasing fields and the value decreases with applied stress. Maximum d_{33} is always higher for increasing field than for decreasing field at each applied stress.

The maximum field-induced strain for each load is plotted against the applied stress in Fig. 4.14. The rapid reduction in strain even with small changes in load at low loads is an interesting feature of the sample. The rate of decrease in strain is gradual after about 15 MPa. The figure infers the low work capability of this sample even at small loads.
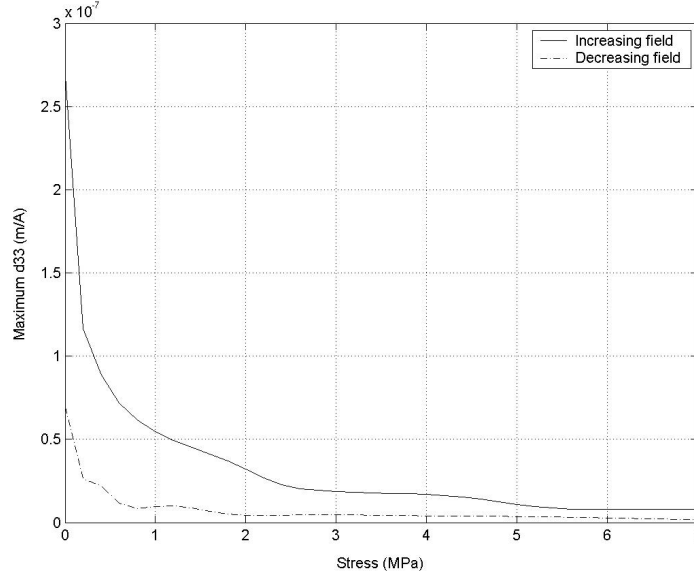
Figure 4.13: Maximum piezomagnetic coefficient d_{33} vs applied stress for dls-1-136-1.

The dls-1-136-1 sample was subjected to a major loop compression test starting at zero magnetic field and increasing levels of DC magnetic field which were generated using a DC power supply. The DC magnetic field values start from 32.33 kA/m and then in multiples of 54 kA/m up to a maximum value of 378 kA/m. It should be noted that the maximum value of the applied DC magnetic field does not saturate the sample. Fig. 4.15 shows the major compressive stress-strain loops for the different values of DC magnetic fields. Along the line of zero compressive stress, the loops for each DC field has a certain offset showing the initial contraction of the sample due to the field before the application of stress. The maximum load subjected to the sample was 95 lbs (13.36 MPa). It is observed that the stress-strain hysteresis decreases with increasing DC field and there is a certain amount of non-closure for each loop. The
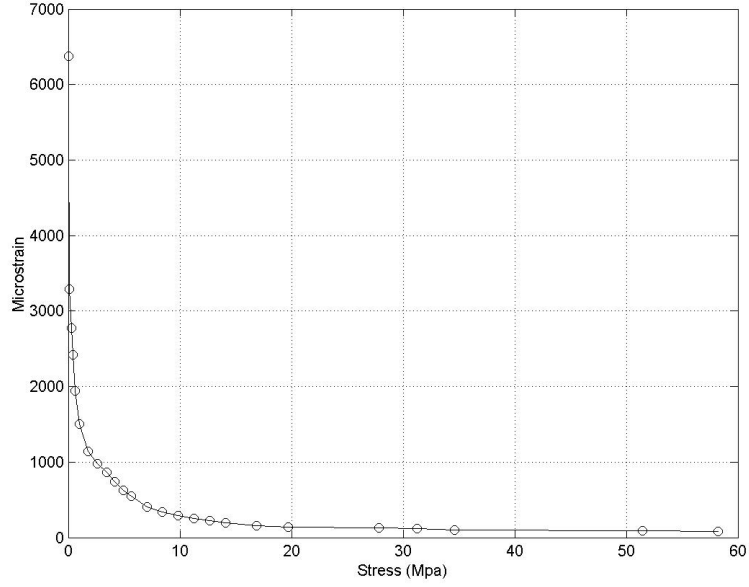
Figure 4.14: Maximum field-induced strain at 0.1 Hz drive vs applied stress for dls-1-136-1.

non-closure of the loops may be due to the remanent magnetization that retains a certain magnitude of contraction even after the stress is completely removed. Another feature of these loops is that as the stress is increased, the material gets dominated by the mechanical effects as compared to the lower stress region where the magnetic effects dominate.

Fig. 4.16 is a reproduction of Fig. 4.15 showing only the loading portion of the curves with all the initial contractions at the various field levels set to zero, i.e. removing all the initial strain offsets of the loading curves of Fig. 4.15. It is observed that the curves become steeper with increasing DC field and the difference between the curves becomes smaller with increasing field. The curve for the zero field shows

108
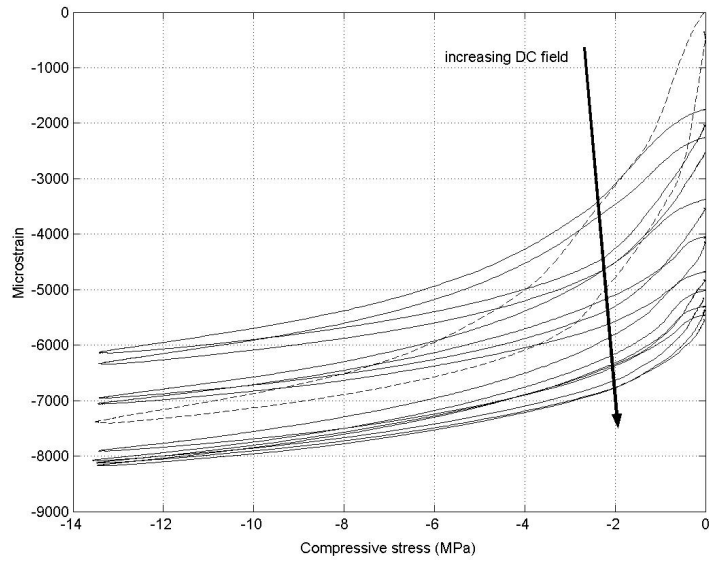
Figure 4.15: Strain vs compressive stress loops at different levels of applied DC magnetic field for dls-1-136-1 with the dash line showing the loop for zero field.
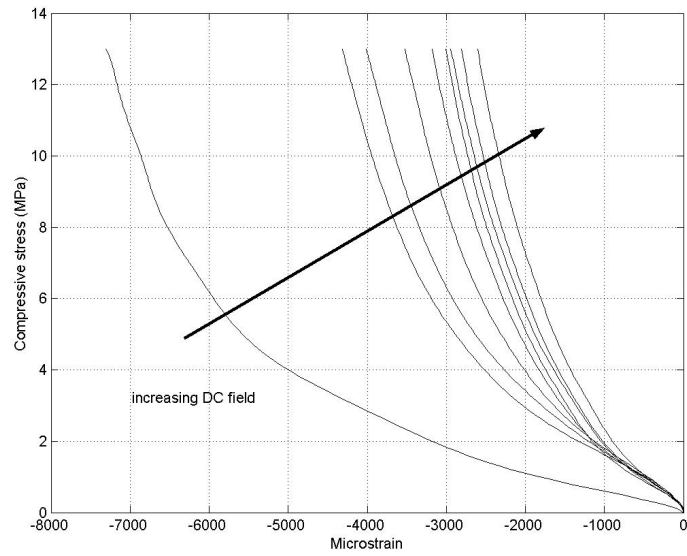

Figure 4.16: Loading curve of compressive stress-strain loop at different DC magnetic fields for dls-1-136-1.

neither a well defined starting twinning stress σ_s nor a prominent finish twinning stress σ_f for the applied range of compressive stress but it can be seen that $\sigma_f > 10$ MPa and $\sigma_s < 0.1$ MPa.

The variation of Young's modulus with compressive stress at different DC field levels is shown in Fig. 4.17. The modulus increases with increase in stress and DC field. There seems to exist a minima for the Young's modulus at each DC field level between 1-2 MPa. So the Young's modulus is higher at the beginning of the compression and slowly decreases reaching a minimum after which it again increases. This is typical of shape memory alloys and is due to the softness of the material in the martensite twinning region but comparatively higher stiffness before and after the twinning region.

Fig. 4.18 shows second order quadratic fits for the variation of Young's modulus with DC field at fixed compressive stress levels which are obtained from Fig. 4.17 by extracting the Young's modulus values at different DC fields but at fixed compressive stress values. The Young's modulus changed by 186% and 65% at 3 MPa and 12.2 MPa respectively for the range of applied DC field. This further verifies the increase in the stiffness of the specimen with increasing compressive stress and field.
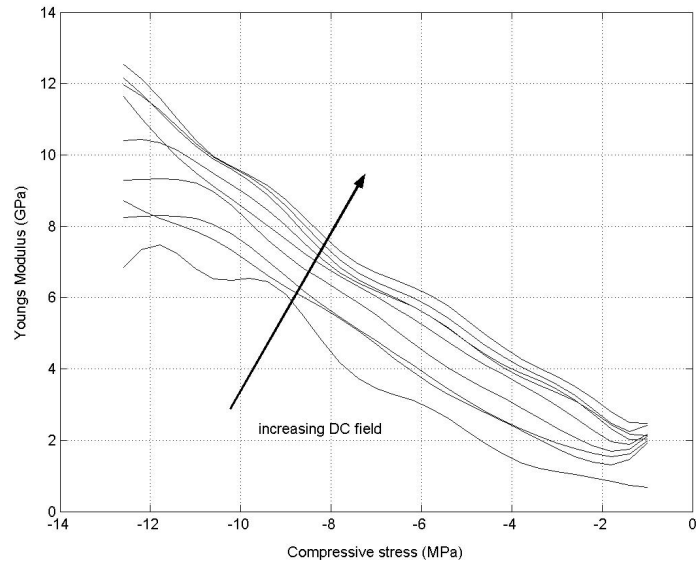
Figure 4.17: Variation of Young's modulus with compressive stress at different DC fields.
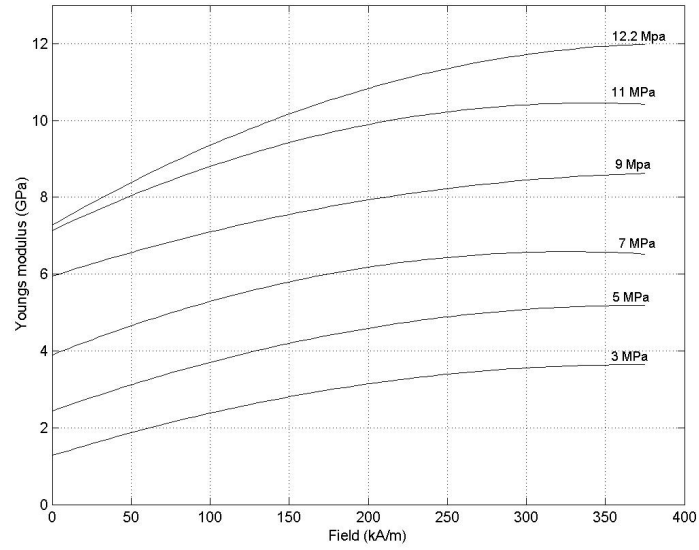

Figure 4.18: Variation of Young's modulus with applied DC magnetic field at different compressive stress levels.

4.5.2 Results for dls-1-125-4

The dls-1-125-4 is the specimen with the highest percentage of manganese and gallium (dls-1-136-1 also has the same percentage of Ga) but with the lowest valence electrons per atom of 7.591. The maximum negative strain produced by this sample is 4300 ppm at 0.1 Hz sinusoidal magnetic field of amplitude 8.1 kOe under zero load. Fig. 4.19 shows the strain plotted against the magnetic field under zero load. The crossover point occurs at 621 ppm and the d_{33} is 9.2769×10^{-8} and 3.0847×10^{-8} for increasing and decreasing fields respectively. The piezomagnetic coefficient is greater in the increasing field than in the decreasing field similar to the trend observed in dls-1-136-1.
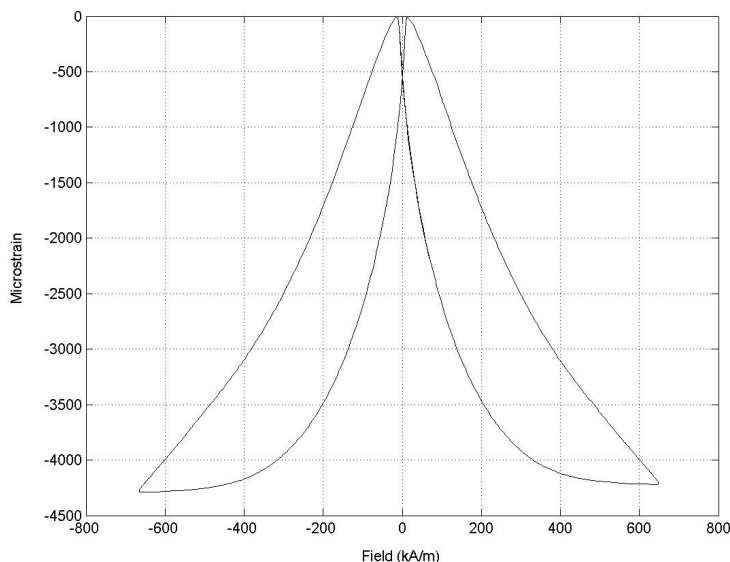
Figure 4.19: Strain vs magnetic field curve for dls-1-125-4 at zero load and 0.1 Hz sinusoidal magnetic field.

The variation of d_{33} with the applied magnetic field at zero load can be seen in Fig. 4.20 which is similar to dls-1-136-1 except for comparatively lower values. The strain curve of dls-1-125-4 is different from that of dls-1-136-1 at the points of peak field. It is seen that the curve does not approach zero gradient in the increasing field as much as the curve for dls-1-136-1. Hence, d_{33} does not approach zero at points of peak fields which can be readily seen from the figure. In the increasing field, the maximum value of d_{33} occurs at approximately the point of zero field. The magnetization curve in Fig. 4.21 shows a saturation magnetization of about 342.8 kA/m (46.08 emu/gm)which is lower than the value for dls-1-136-1. The remanence and coercivity are about 171.25 kA/m (0.215 T) and 8.25 kA/m respectively.
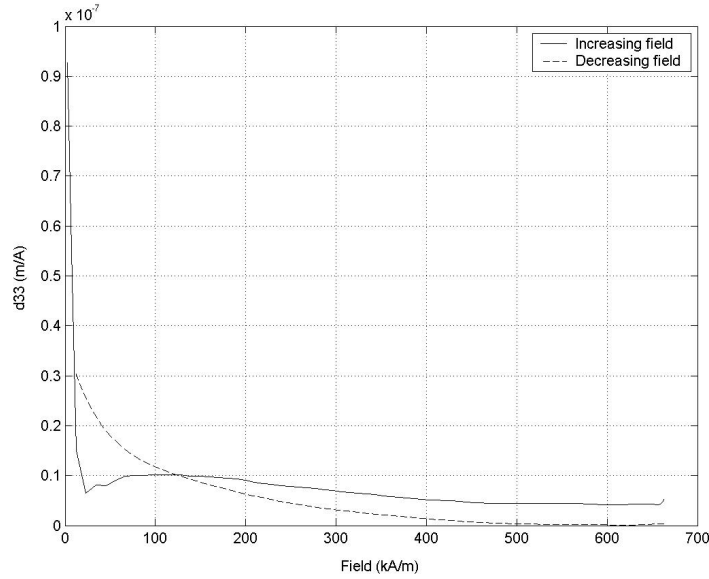
Figure 4.20: Variation of piezomagnetic coefficient d_{33} with magnetic field for dls-1-125-4 at zero load and 0.1 Hz field.
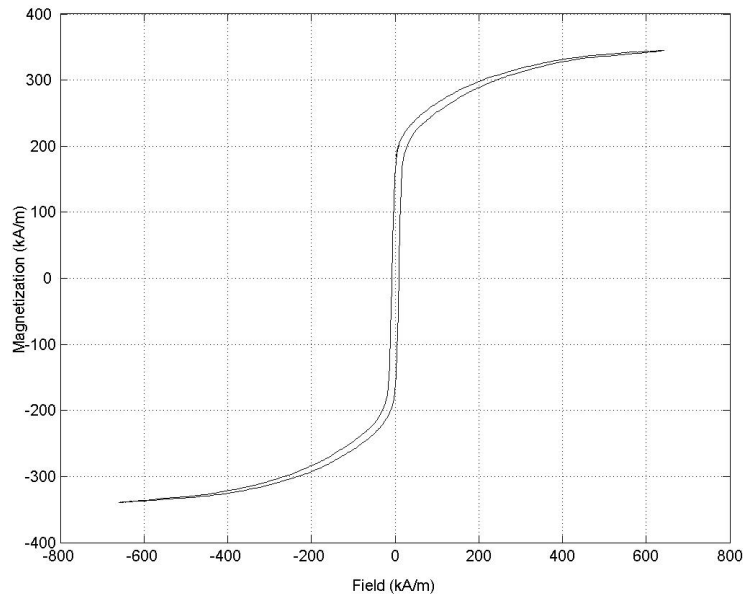
Figure 4.21: Magnetization vs magnetic field curve for dls-1-125-4 at zero load and 0.1 Hz sinusoidal magnetic field.

The sample was run at two other low frequencies of 0.5 and 1 Hz and the comparison of the strain curves for the different frequencies is shown in Fig. 4.22. The crossover point increases with increase in frequency following the same trend as in dls-1-136-1. The piezomagnetic coefficient is also greater in the increasing field than in the decreasing field for all the three frequencies.

The magnetization curves for the three frequencies are shown in Fig. 4.23 and the increase in hysteresis is prominent. The coercivity and remanence both increase with increase in frequency.

The results of the tests conducted at different loads are shown in Figs. 4.24, 4.25 and 4.26. Fig. 4.24 shows the field-induced strain curves for loads between 5-40 lbs
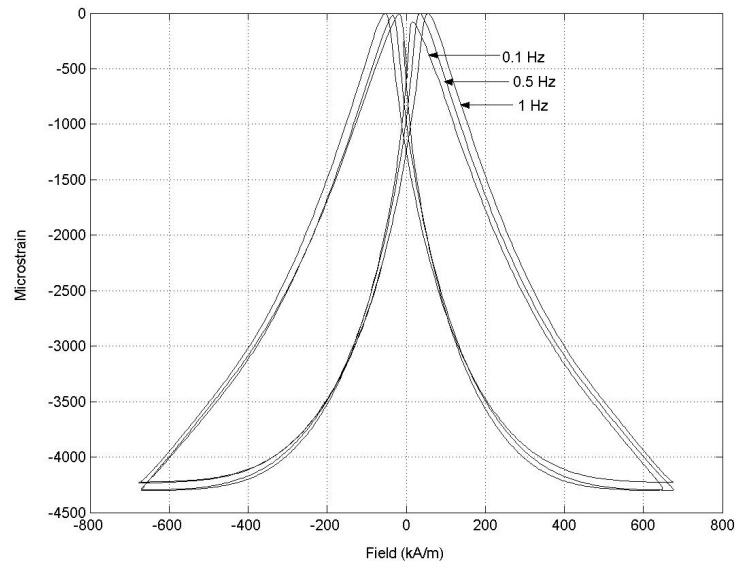
Figure 4.22: Strain vs magnetic field curve for dls-1-125-4 at 0.1, 0.5 and 1 Hz under zero load.
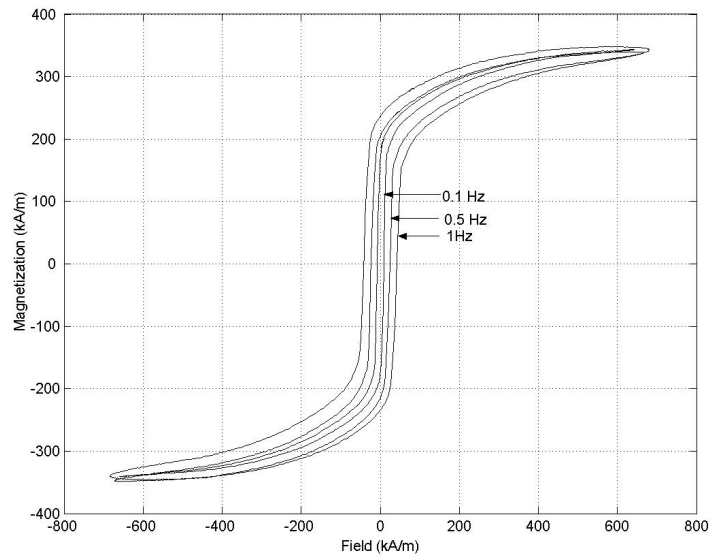

Figure 4.23: Magnetization vs magnetic field curve for dls-1-125-4 at 0.1, 0.5 and 1 Hz under zero load.

(0.7-5.63 MPa) at 5 lb increments. Fig. 4.25 shows the field-induced strain for loads between 50-138 lbs (7.03-19.38 MPa) at 11.8 lb (1.66 MPa) increments and Fig. 4.26 shows the field-induced strain at loads above 150 lbs (21.1 MPa) at 24 lb (3.38 MPa) increments. It is seen that the change in field-induced strain becomes less significant at higher compressive stress and the strain hysteresis effect is also diminishing, i.e. the area engulfed by the strain curve at each compressive stress becomes smaller.

The magnetization curves do not show significant variation with the applied stress. This is shown is Fig. 4.27 for applied stress range 0-65 MPa. The maximum value of d_{33} at different applied stresses is shown in Fig. 4.28 for loads up to 50 lbs (7.03 MPa). The variation of maximum d_{33} for dls-1-125-4 is significantly different from that of dls-1-136-1 due to the lower rate of decrease of d_{33} with stress.
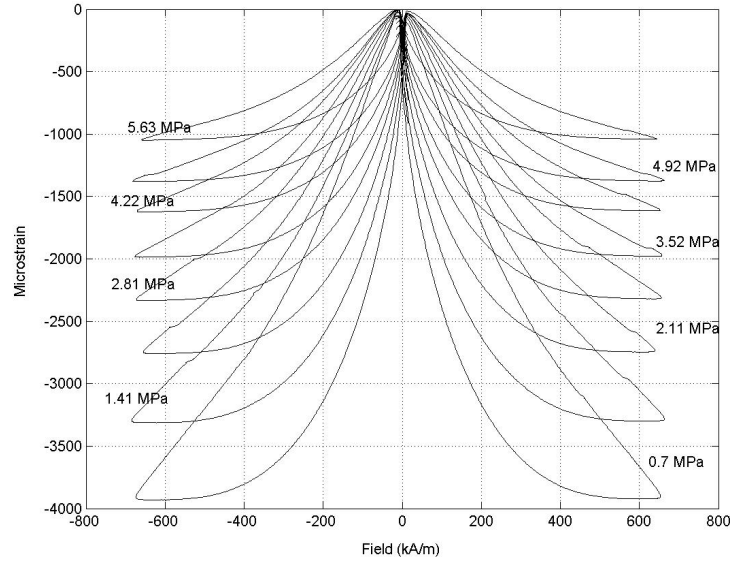

Figure 4.24: Strain vs magnetic field curve for dls-1-125-4 at 0.1 Hz and different loads between 5-40 lbs.
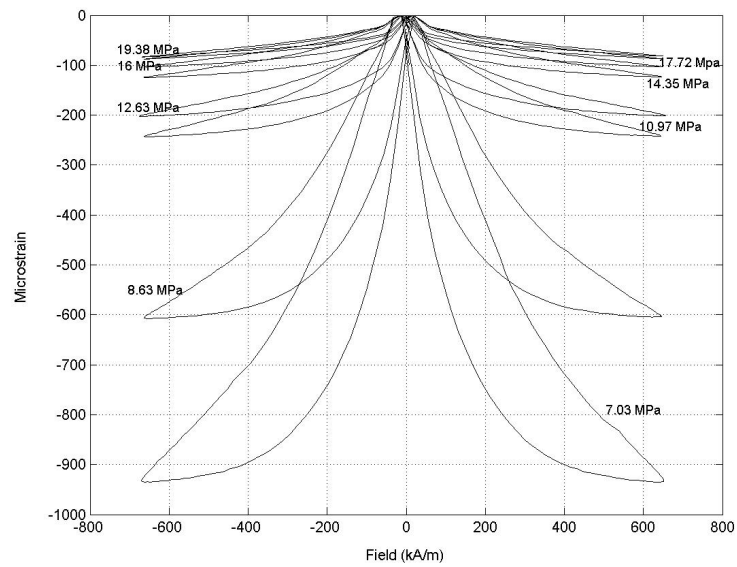
116

Figure 4.25: Strain vs magnetic field curve for dls-1-125-4 at 0.1 Hz and different loads staring from 50-138 lbs.
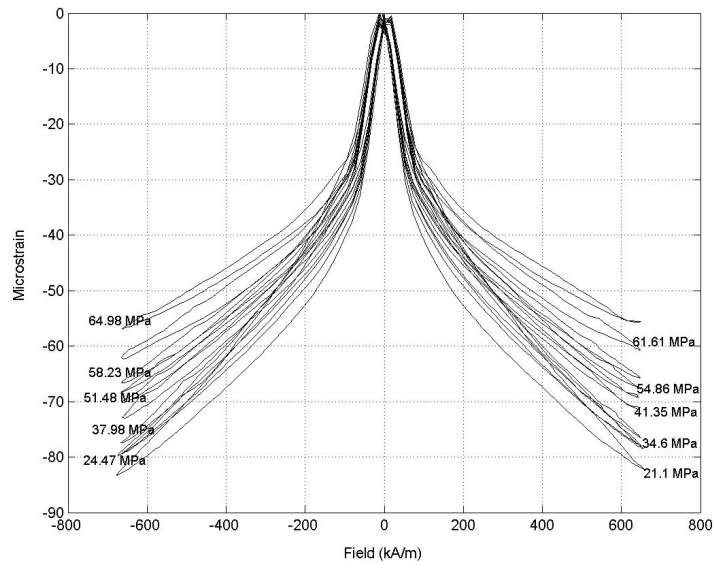

Figure 4.26: Strain vs magnetic field curve for dls-1-125-4 at 0.1 Hz and different loads staring from 150 lbs.
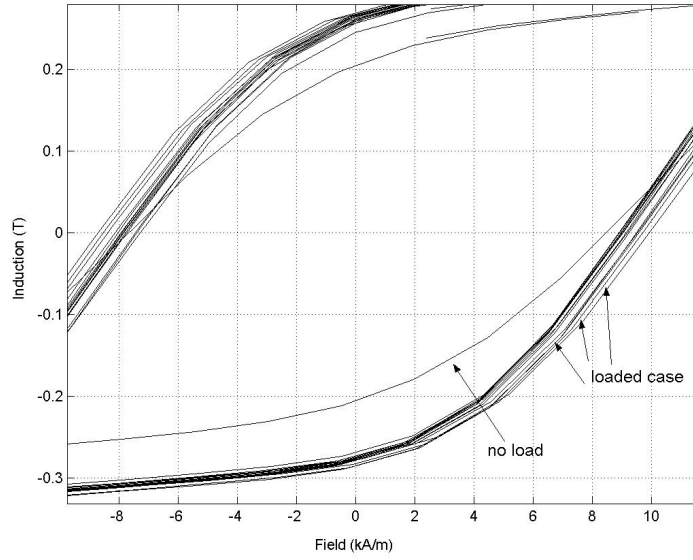
Figure 4.27: Magnetization curves for dls-1-125-4 at 0.1 Hz magnetic field under different loads 0-65 MPa.

Fig. 4.29 shows the peak field-induced strain plotted against the various compressive stress levels. The decrease in strain at lower loads is not as sharp as in the case of dls-1-136-1. The rate of decrease of strain at higher compressive stress is lower than at lower compressive stress levels which is similar to the effect seen in dls-1-136-1. After 15 MPa, the strain decay seems to be very gradual.

The dls-1-125-4 sample was subjected to cyclic compressive stress employing the same method as for dls-1-136-1. The maximum stress applied was 113 lbs (16 MPa). Fig. 4.30 shows the stress-strain loops for different levels of DC magnetic field. The stress-strain hysteresis decreases with increasing DC field with the maximum hysteresis occurring at zero field. The dashed loop corresponding to zero field shows that the sample is almost at its maximum compression at the maximum applied stress
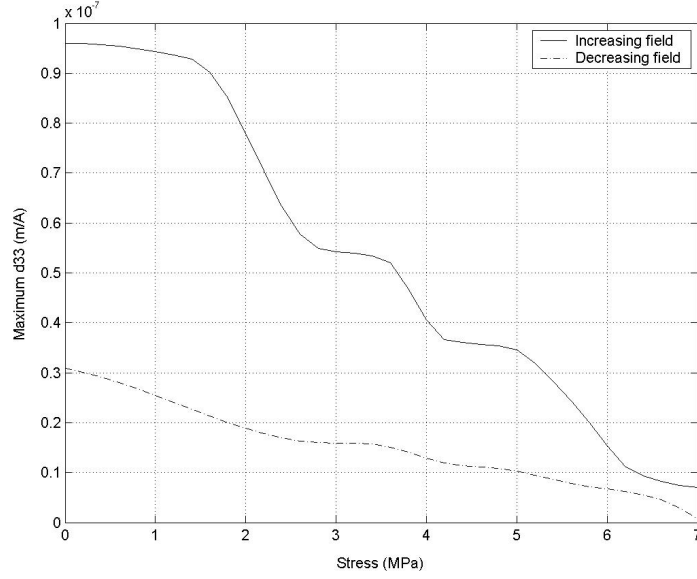
Figure 4.28: Maximum piezomagnetic coefficient d_{33} vs applied stress for dls-1-125-4.

of 16 MPa since the strain is almost constant after 14 MPa. This is different from both dls-1-136-1 and dls-1-61-1 (explained later) where more compression is possible beyond 16 MPa.

The loading portion of the compressive stress-strain loops of Fig. 4.30 is reproduced in Fig. 4.31. It can be inferred from the figure that this sample also becomes stiffer with increasing field and the change in stiffness with DC field at a constant stress becomes less significant at higher fields. From the curve corresponding to zero field, $\sigma_s \approx 0.8$ MPa but $\sigma_f > 12$ MPa.

The variation of Young's modulus with applied compressive stress is illustrated in Fig. 4.32 at different DC magnetic fields which is obtained by taking the slope of the curves in Fig. 4.31. The presence of a modulus minima is clearly seen in the range of
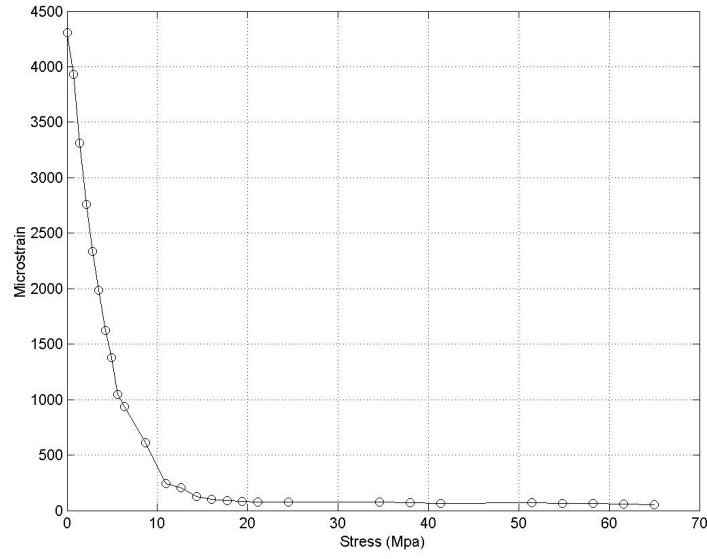
Figure 4.29: Maximum field-induced strain at 0.1 Hz drive vs applied stress for dls-1-125-4.

1-2 MPa at the different DC field levels due to a better defined twinning region than for dls-1-136-1. Fig. 4.33 is obtained from Fig. 4.32 by fitting quadratic curves for the Young's modulus at different DC fields for fixed compressive stresses. Percentage increase of 143% and 66.4% are seen at 3.8 MPa and 13 MPa respectively. It is seen that the Young's modulus increases with both stress and field.
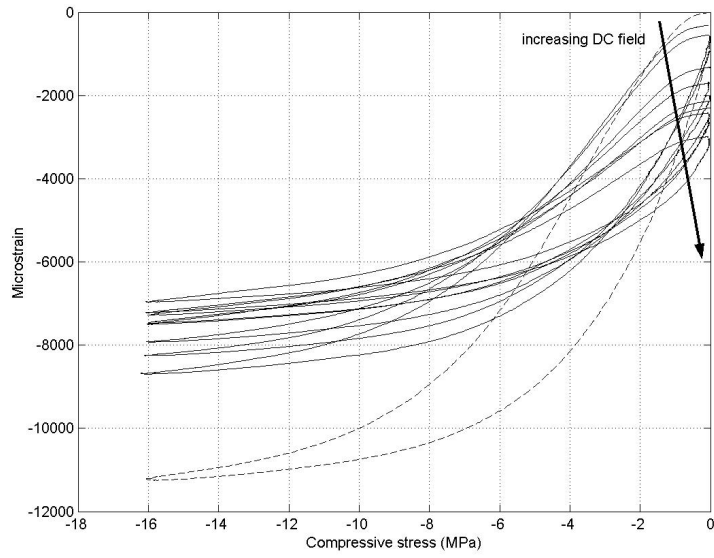
Figure 4.30: Strain vs compressive stress loops at different levels of applied DC magnetic field for dls-1-125-4 with the dash line showing the loop for zero field.
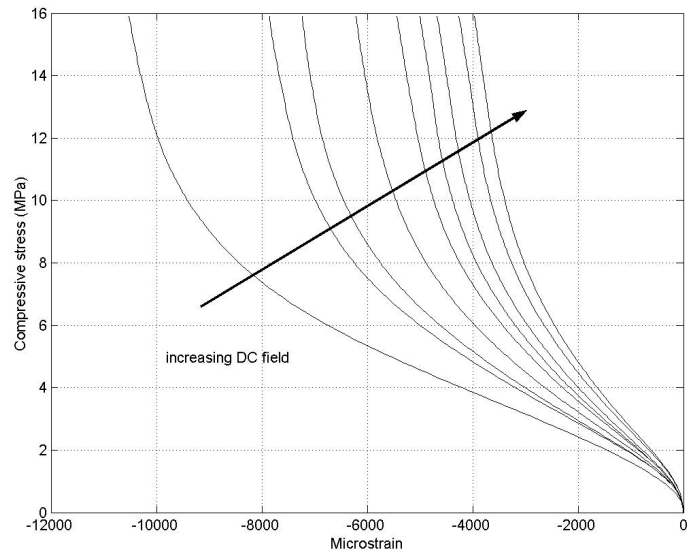

Figure 4.31: Loading curve of compressive stress-strain loop at different DC magnetic fields for dls-1-125-4.
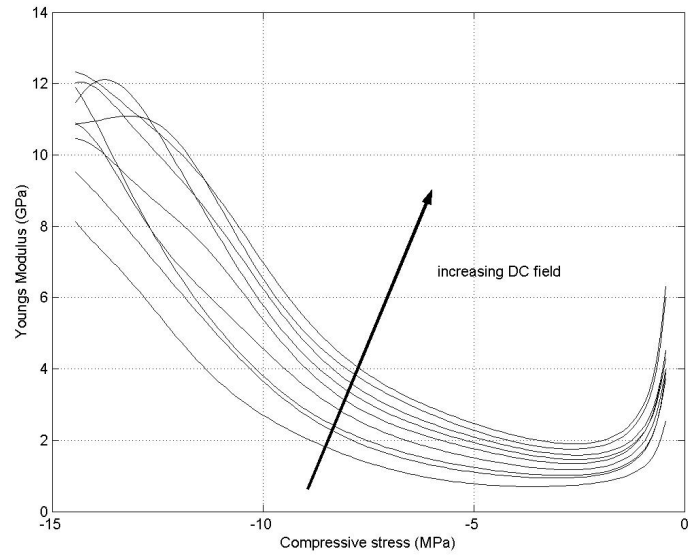
Figure 4.32: Variation of Young's modulus with compressive stress at different DC fields for dls-1-125-4.
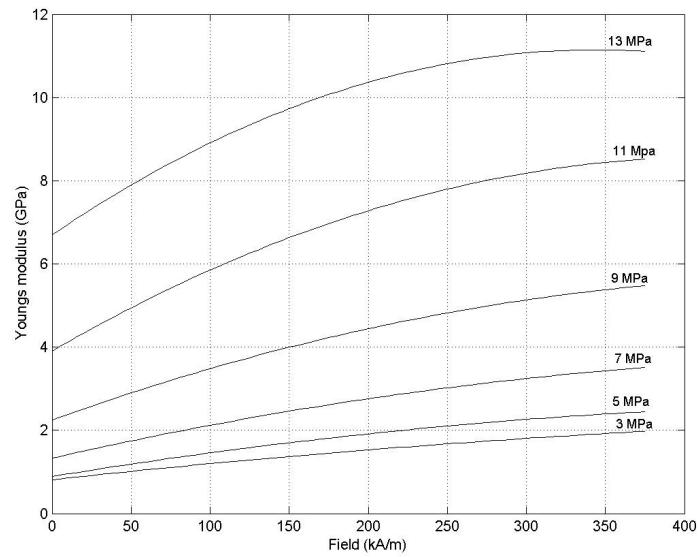

Figure 4.33: Variation of Young's modulus with applied DC magnetic field at different compressive stress levels for dls-1-125-4.

4.5.3   Results for dls-1-61-1

The dls-1-61-1 sample produced a peak field-induced strain of 1192 ppm at no load and 0.1 Hz drive which is shown in Fig. 4.34. The crossover point occurs at 198 ppm and the piezomagnetic coefficient has a value of 3.7653×10^{-8} m/A and 2.0128×10^{-8} m/A for increasing and decreasing fields respectively. It can be inferred that the strain producing capacity per unit field of this sample is comparable in both increasing and decreasing fields unlike dls-1-136-1 and dls-1-125-4 where a considerable difference was noted between the two numbers.

Fig. 4.35 shows the variation of piezomagnetic coefficient d_{33} with the applied field at zero load. The behavior is similar to the ones exhibited by dls-1-136-1 and
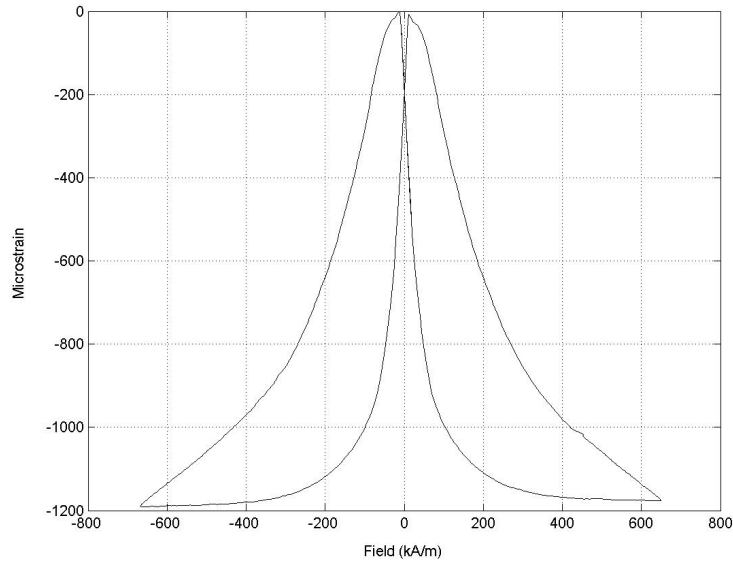

Figure 4.34: Strain vs magnetic field curve for dls-1-61-1 at zero load and 0.1 Hz sinusoidal magnetic field.
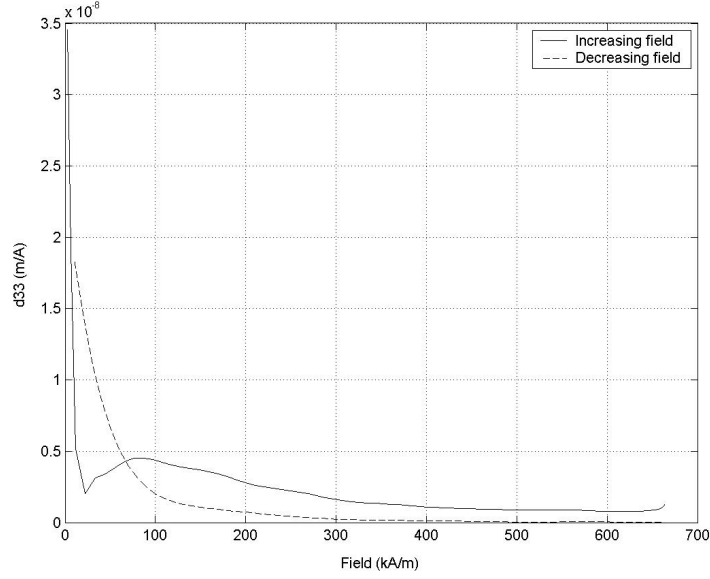
Figure 4.35: Variation of piezomagnetic coefficient d_{33} with magnetic field for dls-1-61-1 at zero load and 0.1 Hz field.

dls-1-125-4 but the values are comparatively lesser for both increasing and decreasing fields. Again the slope of the strain curve at peak field in increasing field does not approach zero as in dls-1-125-4.

The magnetization curve in Fig. 4.36 at 0.1 Hz drive shows a magnetic saturation of about 371.6 kA/m (47.16 emu/gm) with a remanence and coercivity of 222.97 kA/m (0.28T) and 8.87 kA/m respectively.

The comparative results for strain and magnetization at 0.1, 0.5 and 1 Hz are shown in Figs. 4.37 and 4.38. The hysteresis increases with increase in frequency. The increase in coercive field in Fig. 4.37 is also seen in Fig. 4.38 where the points of zero strain shift away from the zero field line. The crossover point increases in
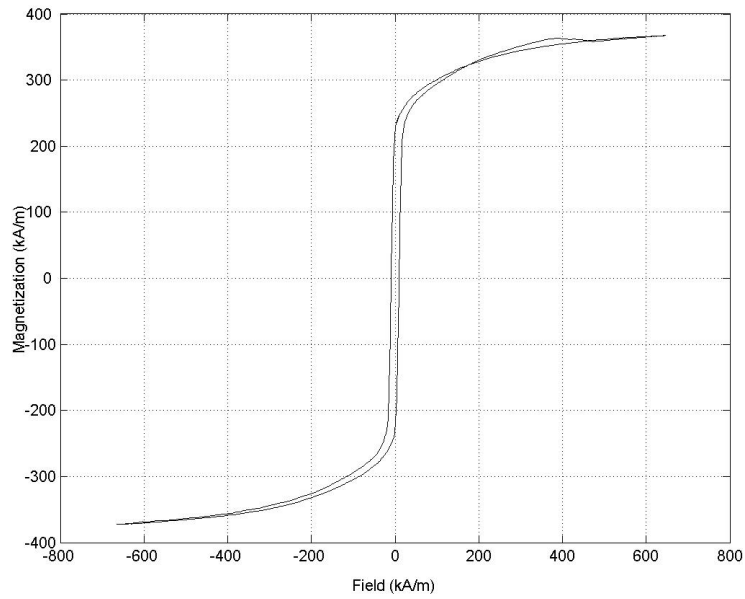
Figure 4.36: Magnetization vs magnetic field curve for dls-1-61-1 at zero load and 0.1 Hz sinusoidal magnetic field.

magnitude with the increase in frequency and the maximum $d33$ coefficient is higher in the increasing field as compared to its value in the decreasing field.

Fig. 4.39 shows the field-induced strain curves for loads between 0-50 lbs . In Fig. 4.40 the field-induced strain is plotted against field for loads between 50- 137.8 lbs at 11.8 lb increments and Fig. 4.41 shows the strain for loads starting at 150 lbs and above at 24 lb increments. A close look at the point of zero strain for all the curves shows that the right half of the curve does not actually reach zero strain. This might be due to an effect similar to that observed in Terfenol-D where the demagnetized sample state is not single valued because of various domain configurations that may exist at the demagnetized state.
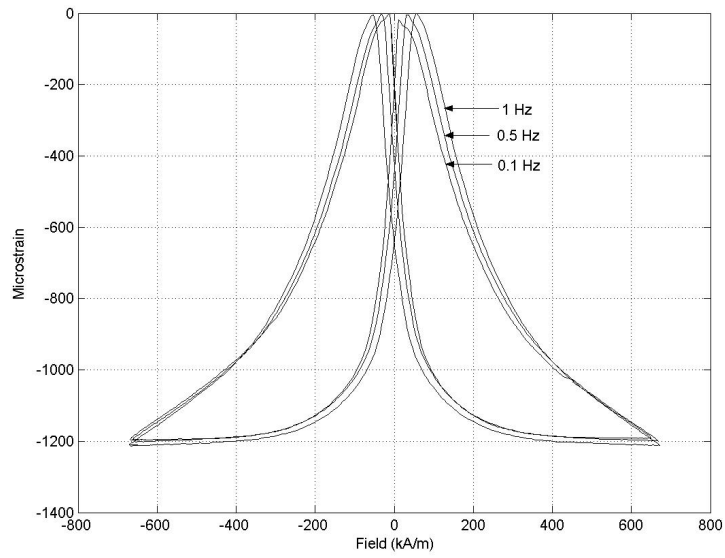
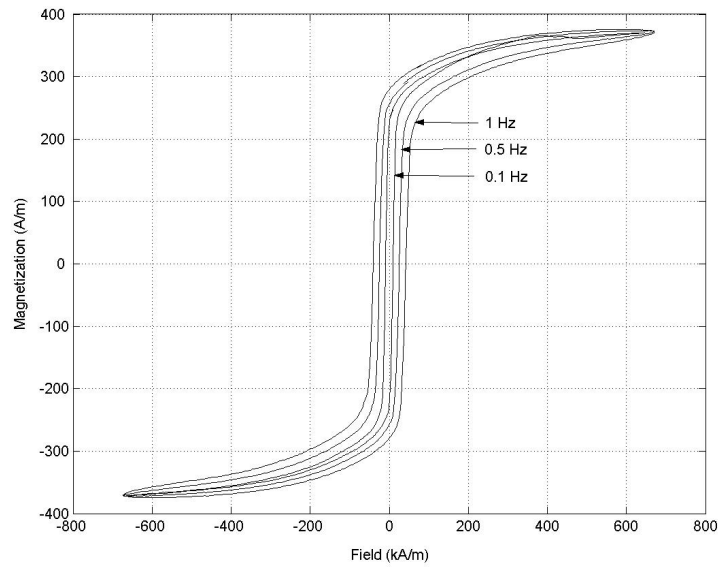Figure 4.37: Strain vs magnetic field curve for dls-1-61-1 at 0.1, 0.5 and 1 Hz under zero load.

Figure 4.38: Magnetization vs magnetic field curve for dls-1-61-1 at 0.1, 0.5 and 1 Hz under zero load.
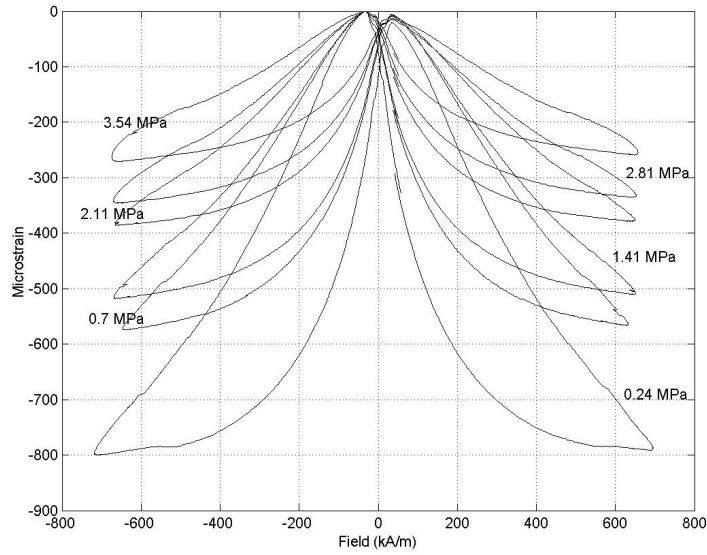
Figure 4.39: Strain vs magnetic field curve for dls-1-61-1 at 0.1 Hz and different loads between 5 and 50 lbs.

Fig. 4.42 shows the magnetic induction curves for the applied stress range 0-51.5 MPa. As in the other two samples, no significant change is seen in induction with change in applied stress. The variation of maximum value of d_{33} with applied stress is illustrated in Fig. 4.43 with the maximum d_{33} value always being greater for the increasing field than for the decreasing field following the same trend as dls-1-136-1 and dls-1-25-4.

The maximum field induced strain at each compressive stress is plotted in Fig. 4.44. It is seen that there is a drastic decrease in strain for the lower compressive stress values and this behavior more closely resembles dls-1-136-1 than dls-1-125-4 in which the rate of decrease is very high at lower stress.
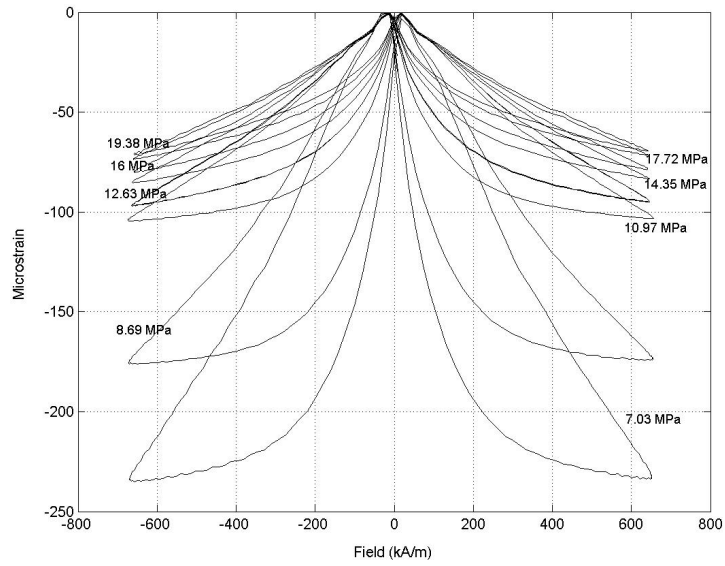
Figure 4.40: Strain vs magnetic field curve for dls-1-61-1 at 0.1 Hz and different loads between 50 and 137.8 lbs.
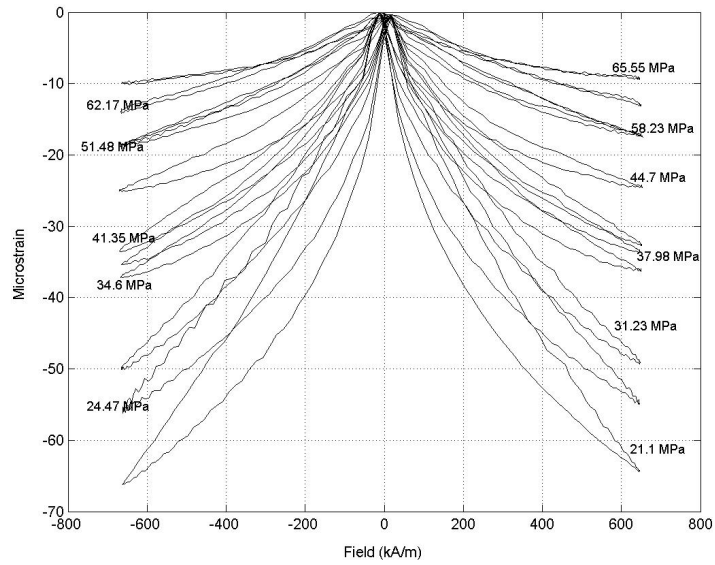

Figure 4.41: Strain vs magnetic field curve for dls-1-61-1 at 0.1 Hz and different loads starting at 150 lbs and above.
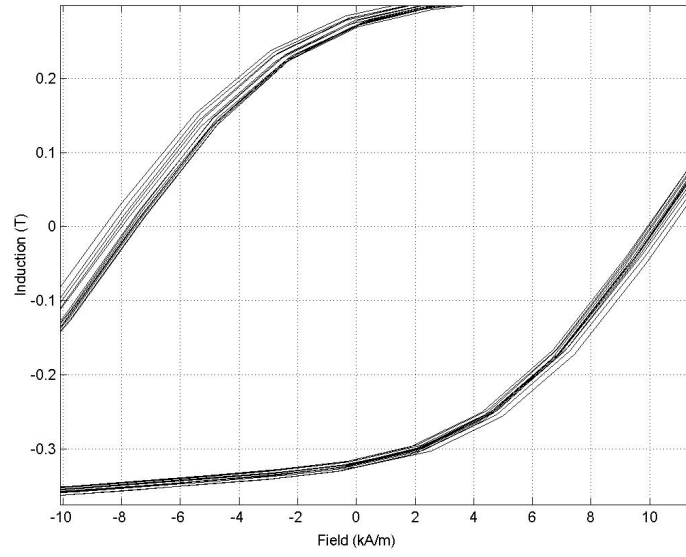
Figure 4.42: Magnetization curves for dls-1-61-1 at 0.1 Hz magnetic field under different loads.
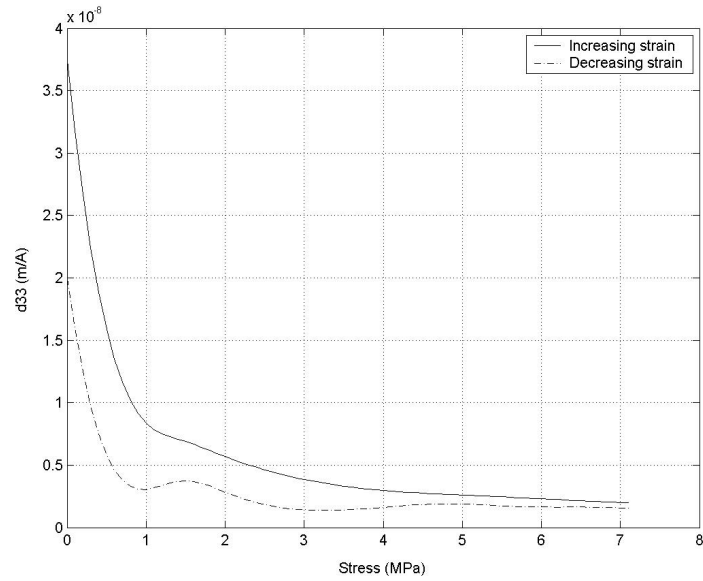

Figure 4.43: Maximum piezomagnetic coefficient d_{33} vs applied stress for dls-1-61-1.

The result of the cyclic compression test is shown in Fig. 4.45 and the maximum hysteresis is associated with the loop corresponding to zero magnetic field. A certain degree of non-closure is seen for the loop corresponding to zero magnetic field. However, loop closure is seen for loops at higher fields.

The loading curves for the stress-strain loops are shown in Fig. 4.46 from which the increase in stiffness with increase in field is clearly seen. The initial negative strain due to the applied DC field has been offset to zero for comparison. The curve corresponding to the zero field shows $\sigma_s \approx 0.5$ MPa but $\sigma_f > 8$ MPa.

Fig. 4.47 shows the variation in Young's modulus with applied stress at different DC fields which is obtained from the slopes of the curves in Fig. 4.46. A modulus minima seems to exist at a comparatively higher range of 2-5 MPa.
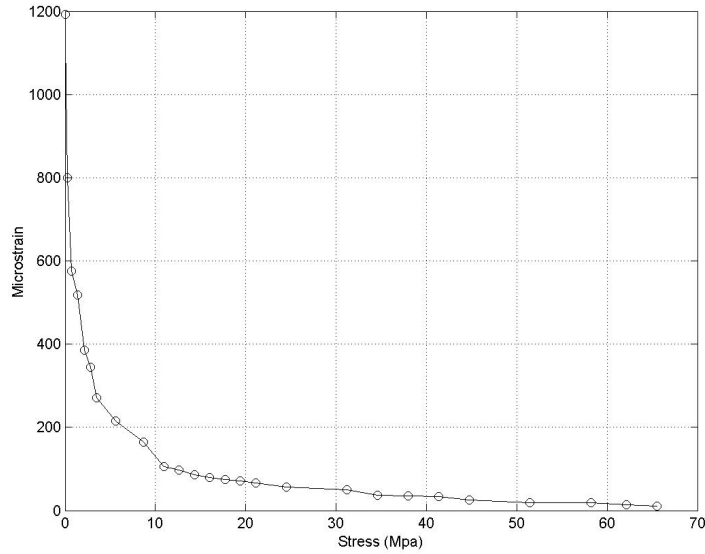
Figure 4.44: Maximum field-induced strain at 0.1 Hz drive vs applied stress for dls-1-61-1.

130
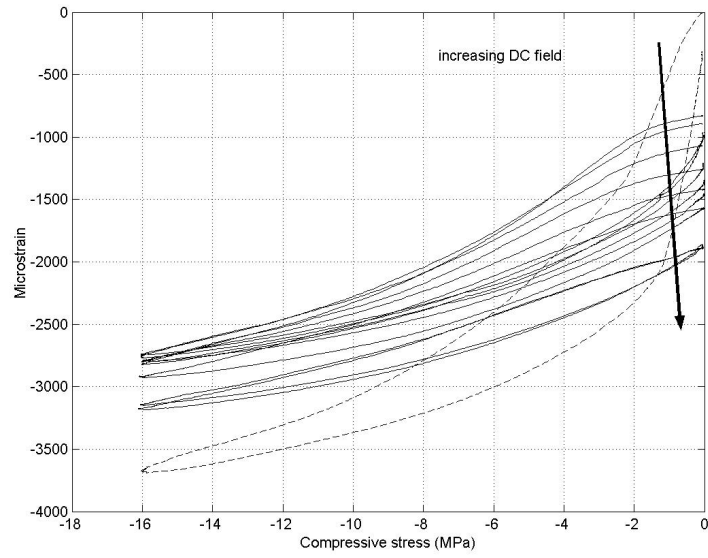
Figure 4.45: Strain vs compressive stress loops at different levels of applied DC magnetic field for dls-1-61-1 with the dash line showing the loop for zero field.
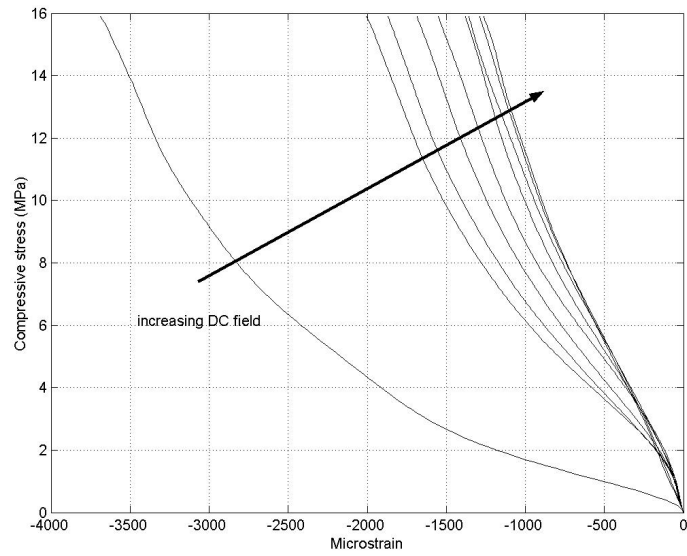
Figure 4.46: Loading curve of compressive stress-strain loop at different DC magnetic fields for dls-1-61-1.
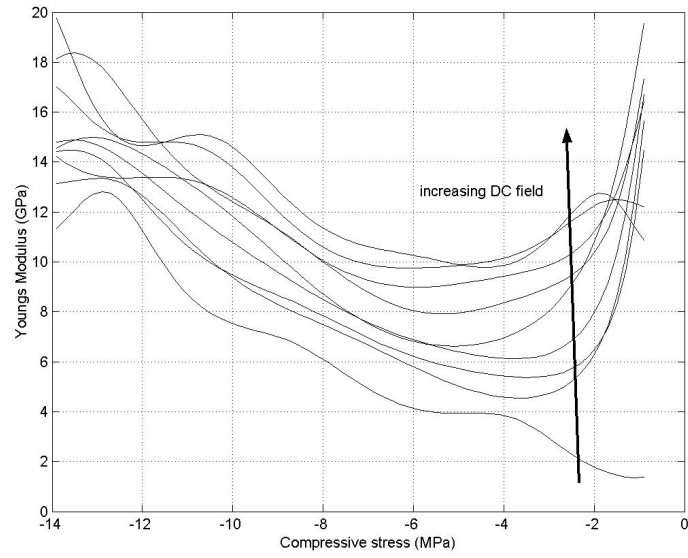
Figure 4.47: Variation of Young's modulus with compressive stress at different DC fields for dls-1-61-1.

Figure 4.48: Variation of Young's modulus with applied DC magnetic field at different compressive stress levels for dls-1-61-1.

The softest region, therefore, occurs at a higher stress in dls-1-61-1. Fig. 4.48 shows the variation of the Young's modulus with DC field at certain fixed stress values. Percentage changes of 139% and 31% in the Young's modulus were seen at 5 MPa and 13 MPa respectively. Following the trend of dls-1-136-1 and dls-1-125-4, the stiffness of the sample increases with applied field and stress.
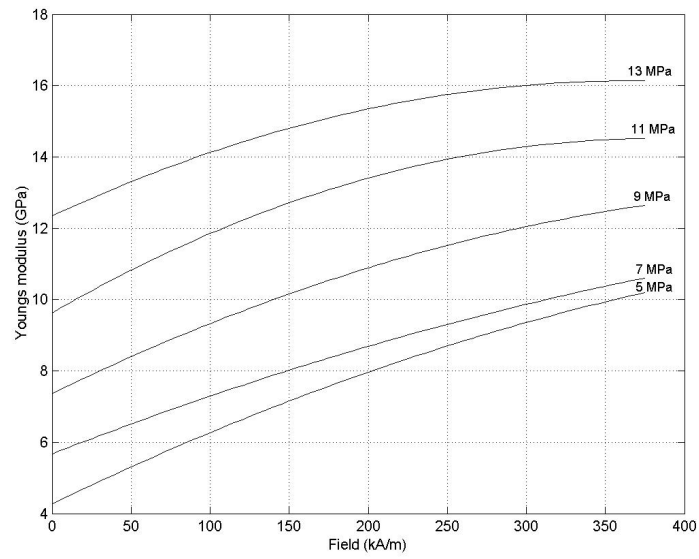
4.5.4   Results for dls-1-42-1, dls-1-42-2 and dls-1-42-3

The dls-1-42 series samples have lesser percentage of Ga by weight as compared to dls-1-136-1, dls-1-125-4 and dls-1-61-1 and the magnitude of the field-induced strain produced by these samples is very weak. The dls-1-42-1, dls-1-42-2 and dls-1-42-3 produced 240, 215 and 177 ppm respectively under zero load. This order of field-induced strain is comparable to the magnetostrain of the steel end pieces used and ,therefore, the percentage error in the observed strain after the subtraction of steel magnetostriction would be higher. The dls-1-42 samples were also subjected to higher loads but due to the error as explained above for weak samples, a clear trend could not be established and the strain graphs have not been presented. The magnetization data for the dls-1-42 samples indicate a saturation magnetizations of 323, 330 and 335 kA/m for dls-142-1, dls-1-42-2 and dls-1-42-3 respectively. It is seen that these three samples do not differ much in their magnetic properties and their capacity to produce field induced-strain. These values of saturation magnetization are significantly smaller than the three samples that produced large strains which might explain the low field-induced strain in the dls-1-42 series. The maximum permeabilities recorded were 32.85, 34.17 and 33.41 H/m for dls-1-41-1, dls-1-42-2 and dls-1-42-3 respectively.

4.6 Magnetization Comparison of the Tested Samples with Samples of Different Composition

This section discusses the mapping of the tested samples based on their composition by superimposing them on previously developed composition maps [10]. The samples are mapped in the saturation magnetization versus valence electrons per atom graph in which the authors have approximated a straight line fit for the data collected. Fig. 4.49 shows the experimantal saturation magnetization for the tested samples plotted as a function of the composition based on the valence electrons per atom. From the figure, it is seen that the tested sample that most closely matches
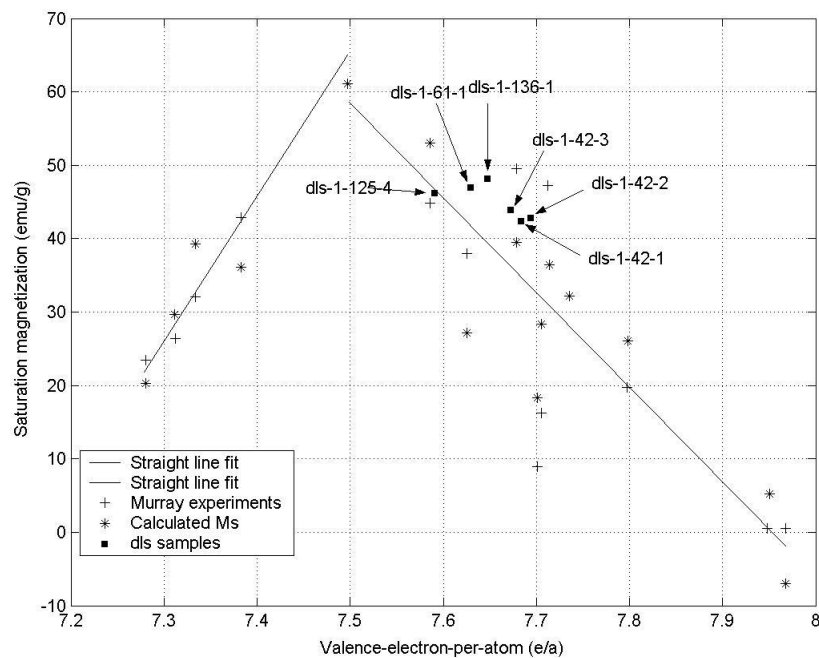

Figure 4.49: Experimental and calculated saturation magnetization mapping for different Ni-Mn-Ga alloys as a function of e/a ratio as well as for the measurement obtained from our experiments.

the straight line fit is the dls-1-125-4. These results on the samples show that the magnetization does not decrease with the increase in the e/a ratio and a specific trend may not be possible to define for the samples.

It is seen that the sample that produced the highest field-induced strain has the highest saturation magnetization value of 48.23 emu/gm while the inactive samples have saturation magnetization values that are less than 42 emu/gm. A sample with the composition in the shaded region of Fig. 1.1 expected to show large field-induced strain would have saturation magnetization value in the range 60-64 emu/gm. A higher saturation magnetization might thus, suggest better field-induced strain.

4.7   Discussion of Results for dls-1-136-1, dls-1-125-4 and dls-1-61-1

The magnitude of field-induced strains in the dls samples $Ni_{50}Mn_{28.7}Ga_{21.3}$ (dls-1-136-1), $Ni_{48.1}Mn_{30.6}Ga_{21.3}$ (dls-1-125-4) and $Ni_{48.99}Mn_{29.98}Ga_{21.03}$ (dls-1-61-1) are considerably smaller than that observed in $Ni_{48}Mn_{30}Ga_{22}$ [12, 13]. Simple mechanical compression test performed on the samples show that the strain produced is about six times smaller than that observed in $Ni_{48}Mn_{30}Ga_{22}$. In accordance with Likhachev's model [13], only those samples with very low twinning stress are good candidates for producing large field-induced strain. This statement follows from the fact that the applied magnetic field generates an equivalent magnetic stress that would have to overcome the twinning stress in order to achieve the same strain effect as a mechanical compressive stress. Fig. 4.50 shows the compressive stress-strain curves for the tested samples (the microstrain has been converted into percentage strain) and Fig. 4.51 shows the result of the mechanical compressive stress test for $Ni_{48}Mn_{30}Ga_{22}$ according to Likhachev.
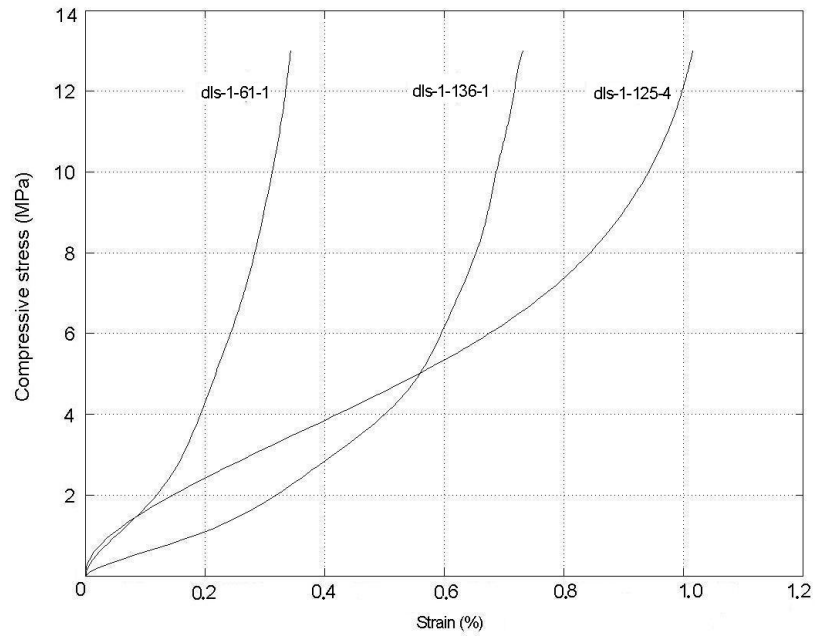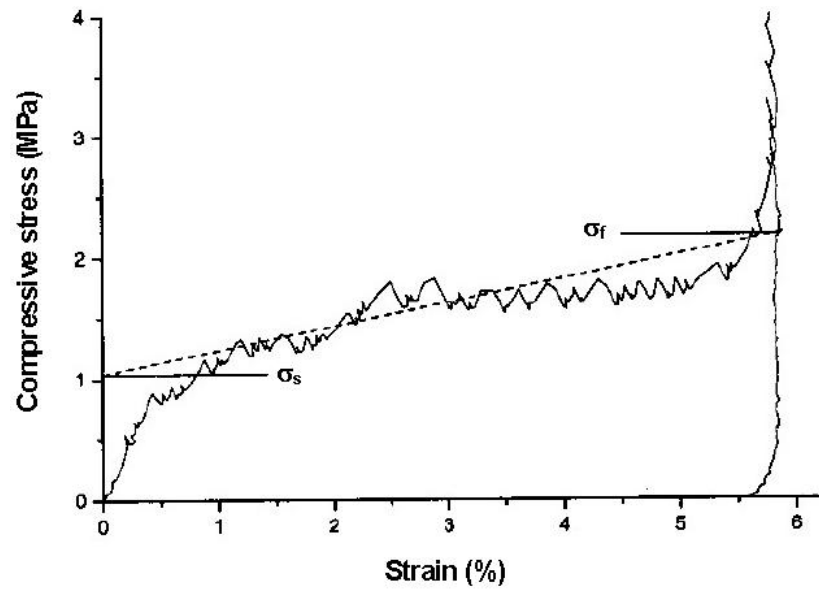
Figure 4.50: Compressive stress-strain curves for dls samples.

Figure 4.51: Compressive stress-strain curve for $Ni_{48}Mn_{30}Ga_{22}$ [12, 11].

In Fig. 4.51, $\sigma_s \approx 1.04$ MPa, $\sigma_f \approx 2.12$ MPa and $\varepsilon_0 = 5.8\%$. From Section 2.2, it was seen that the maximum equivalent magnetic stress that can be produced in $Ni_{48}Mn_{30}Ga_{22}$ is about 2.25 MPa which is greater than σ_f and can easily overcome the twinning stress giving large field-induced strains. In the case of the samples reported in this thesis, value for maximum σ_{mag} is not known. However, if it is assumed that maximum σ_{mag} is close to the value for $Ni_{48}Mn_{30}Ga_{22}$ (assuming a tetragonal martensitic structure), then it can be immediately inferred that this magnitude of the equivalent magnetic stress is insufficient to produce large strains of the order of those obtained from mechanical compression testing. This is because $\sigma_f > 8$ MPa for all the tested samples. Hence, in order to obtain large field-induced strains, the material should have a low twinning stress range and additionally, a greater equivalent magnetic stress as compared to the finish twinning stress. A careful analysis of the stress-strain curve for dls-1-136-1 shows that the maximum mechanical strain in the twinning region might not be greater than 0.8% and the observation of field-induced strain as large as 0.64% may infer that the magnetic driving force in this sample may be greater than that in $Ni_{48}Mn_{30}Ga_{22}$ so that $\sigma_{mag} > 2.25$ MPa. This further implies that the difference in magnetization (the difference in magnetic free energy) between the axial and transverse variants is greater in the dls-1-136-1 crystal structure.

An interesting feature can be observed from the results of cyclic compression tests for the samples. The compressive stress-strain loops demonstrate a very good closure, i.e. appreciable decrease in strain is seen with unloading. This effect is not seen in $Ni_{48}Mn_{30}Ga_{22}$ where during unloading, there is very less strain recovery and a result, greater mechanical hysteresis exists. So for the same magnitude of stress, a greater energy loss would be encountered as compared to the tested samples.

The continuous decrease in magneto-strain with increase in applied stress in collinear drive configuration is a trend that requires some explanation. In absence of external load but only axial field, the theory of variable volume fraction of variants [12, 13, 18] may be applied to the observed sample behavior. Due to magnetic anisotropy, the magnetic force favors the axial variants with the crystallographic easy axis (the short axis) in the direction of the field. So there is a tendency for the formation of more axial variants at the cost of the other variants which means that the contribution to the length from the transverse variants decreases and the rod contracts. When an axial external load is applied, the effect is to bias the variants into the axial variant form and a subsequent contraction follows. But after the application of the stress, more axial variants would be present than other types of variants so the net magnetization difference decreases. This decrease in magnetization difference, decreases the equivalent magnetic stress because as mentioned before, the equivalent magnetic stress strongly depends on the magnetization difference of the favorable and unfavorable variants. This decreased equivalent magnetic stress produces lower reversible strains. As the external stress is increased, the material gets mechanically biased with more axial variants resulting in lesser reversible strain.

The sharper decay in peak strain of dls-1-136-1 (Fig. 4.14) with applied compressive stress as compared to the other samples may be explained using the mechanical compression test result and the explanation in the preceding paragraph. It is seen that below 5 MPa, dls-1-136-1 has the lowest stiffness which means that at lower stress, dls-1-136-1 has a greater volume fraction of axial variants as compared to other samples. Therefore, axial variants nucleate more easily at lower stress in dls-1-136-1 and a

very small fraction of the other variants remain. The magnetization difference, there-fore, decreases rapidly at lower stress generating lower equivalent magnetic stress. Accordingly, the magnitude of the reversible strain decreases drastically.

4.8 Tabular Summary of the Zero Load Tests

Sample	Frequency (Hz)	Crossover point (ppm)	Max. d_{33} (A/m) increasing field	Max. d_{33} (A/m) decreasing field
	0.1	855	2.71×10^{-07}	7×10^{-08}
dls-1-136-1	0.5	1825	5.98×10^{-08}	4.18×10^{-08}
	1	2670	1.11×10^{-07}	2.82×10^{-08}
	0.1	621.4	9.28×10^{-08}	3.08×10^{-08}
dls-1-125-4	0.5	965	4.44×10^{-08}	2.22×10^{-08}
	1	1250	4.78×10^{-08}	1.77×10^{-08}
	0.1	198	3.77×10^{-08}	2.01×10^{-08}
dls-1-61-1	0.5	435	1.81×10^{-08}	1.23×10^{-08}
	1	643	2.33×10^{-08}	7.74×10^{-09}

Table 4.1: Properties computed from the strain vs magnetic field curves at no applied load.

Sample	Frequency (Hz)	Max μ	Coercive field (kA/m)	Remanent field (kA/m)
	0.1	38.16	8.83	207.28
dls-1-136-1	0.5	26.97	24.2	253.77
	1	23.72	40.41	277.66
	0.1	28.26	8.25	171.25
dls-1-125-4	0.5	21.03	22.58	209.92
	1	18.39	40.32	235.94
	0.1	40	8.87	222.97
dls-1-61-1	0.5	28.03	24.19	257.43
	1	24.24	39.91	278.83

Table 4.2: Properties computed from the magnetization vs magnetic field curves at no applied load.

CHAPTER 5

CONCLUDING REMARKS

The goal of this investigation is to provide understanding of and develop proof-of-concept for the strain reversibility in Ni-Mn-Ga samples driven by a collinear magnetic field-stress pair. The conventional actuation method employing orthogonal stress and field has been until now used in experiments to study the magneto-strain effect in the Ni-Mn-Ga system. An important limitation of this drive configuration in applications stems from the use of electromagnets, which are large, heavy and narrowband. The collinear stress-field actuation is implemented by means of a solenoid for the generation of magnetic field, hence it is significantly smaller, lighter and has a broader frequency bandwidth as compared to electromagnets.

A solenoid transducer capable of producing a field on the order of 8.1 kOe was designed and fabricated. This value of the peak field requirement for saturating Ni-Mn-Ga was determined from the literature as well as from preliminary tests carried out in the Smart Material and Structures Laboratory. The transducer design incorporates the necessary requirements for testing the samples under controlled thermal, magnetic and structural regimes. Characterization of the transducer was accomplished through a series of calibration procedures. Three different methods were employed: (a) experimental measurement using a Hall probe, (b) finite element calculations and

(c) analytical equations for thick solenoids. The results yielded remarkably consistent results and an an average rating of 167 Oe/A was established. The loading fixture was designed to load the samples up to 1000 lbs and was fabricated with Unistrut channels. The fixture was designed with the additional criteria of obtaining minimum friction and avoiding bending moments on the samples.

Six samples of varying parent element composition were tested as cast, that is without employing the common practice of material "training" through field cycling and thermal treatment. Further performance enhancements may be achievable through training. The observation of negative field-induced strains as large as 6379 ppm (0.64%) for dls-1-136-1 ruled out the possibility of magnetostriction. Additionally, the magnetization remained largely unaltered for all the samples even when the applied stress was varied. The saturation magnetization for all the samples were in the range of 323 kA/m to 381 kA/m with the highest number being for the sample producing the largest strain. The remanence and coercivity for all the samples were very close and a significant difference was not observed. The maximum value for the piezomagnetic coefficient d_{33} for all the samples was always greater in the increasing field than in the decreasing field with the maximum value in the increasing field occurring between the point of zero strain and the point of zero field. The result of the additional tests run at 0.5 Hz and 1 Hz at zero load showed an increase in magnetic hysteresis and crossover point with increasing frequency. The tests with applied load were conducted at 0.1 Hz sinusoidal magnetic field drive up to blocked load values. For all the samples, a sharp decay in the peak strain was seen at lower applied loads up to about 50 lbs (7.03 MPa) after which the decrease was seen to be more gradual.

The dls samples were subjected to cyclic mechanical compression tests both in zero magnetic fields and with different DC fields. The basic mechanical compression test results conducted at zero field showed that the finish twinning stress σ_f was considerably higher than the range 2-3 Mpa which is the optimum range [13, 12, 11] for achieving large field induced strains in Ni-Mn-Ga. The start twinning stress σ_s was, however, less than 1 MPa for the samples tested. The compression tests in the presence of DC magnetic fields provided information on the variation of stiffness with field. It was observed that all the samples became stiffer with increasing DC field and applied stress, which is phenomenologically in agreement with the ΔE effect oberved in magnetostrictive Terfenol-D. It is emphasized that the stiffness variation in Ni-Mn-Ga is attributed to twin boundary motion, whereas the ΔE effect is due to a completely different physical origin (magnetoelastic coupling.)

The samples were contrasted to material of different compositions tested by several research groups [10] and the information was compiled in a compositional map. The curve fitted Curie temperature contours were not a good fit to the experimental Curie temperatures obtained for the dls samples. The straight line fit for the saturation magnetization against valence-electron-per-atom seemed to be appropriate for dls-1-125-4 but the experimental values for the other samples had a considerable offset from the fit. The empirical composition map for designing Ni-Mn-Ga FSMAs showed that the dls-1-136-1 sample was closest to the shaded area where considerable actuation is expected at room temperature and as seen from the experimental results, the sample produced the maximum field-induced strain.

The ultimate goal of this vein of research is to gain a fundamental understanding and ultimately develop constitutive models of the magnetoelastic and thermoelastic behavior exhibited by these alloys. This investigation represents the first step towards developing such understanding. The results presented here provide necessary information for the development of constitutive models for the behavior of these alloys.
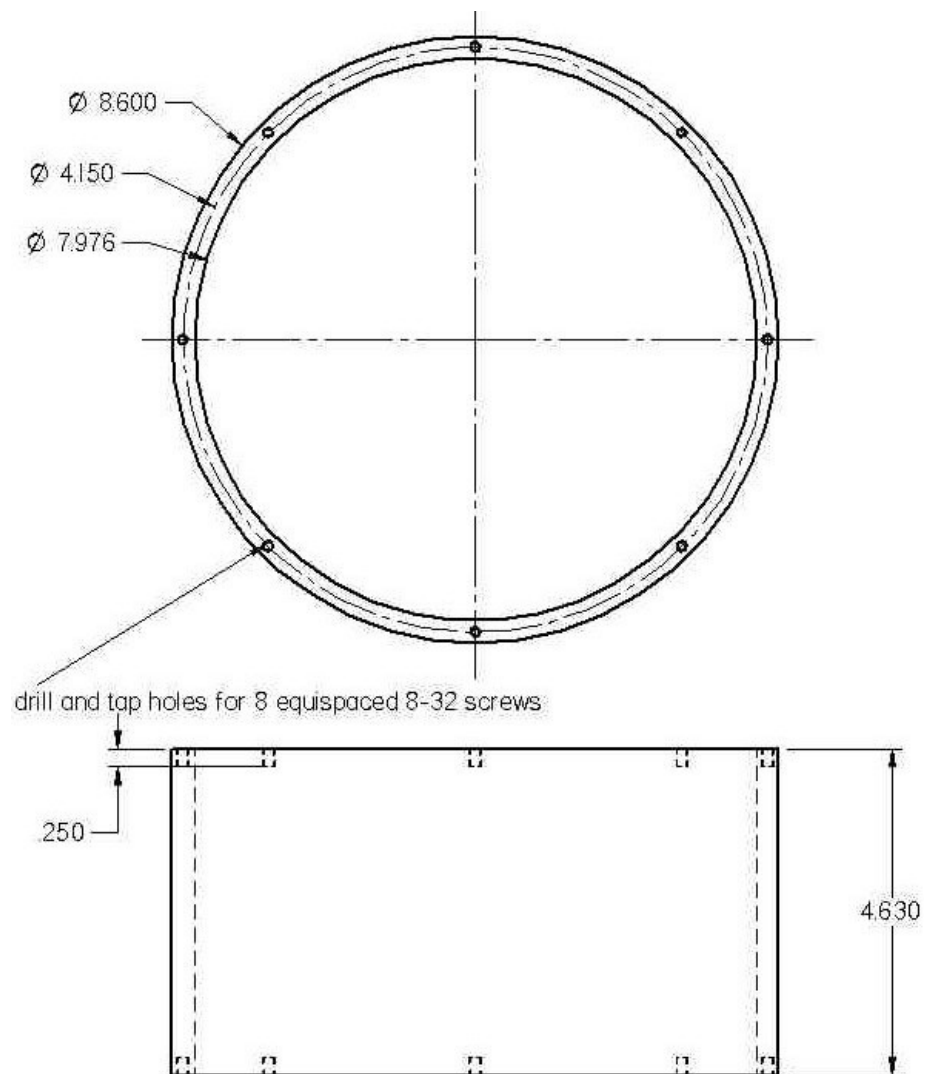
APPENDIX A

WATER COOLED TRANSDUCER DESIGN

Ø 8.600

Ø 4.150

Ø 7.976

drill and tap holes for 8 equispaced 8-32 screws

.250

4.630

Figure A.1: AISI 1018 magnetic steel casing

Ø 8.600

Ø 7.976

Ø 8.300

drill and tap holes for
8 equispaced #8 - 32
slotted head screws

Ø .625
Press fit with bearing

380

.250
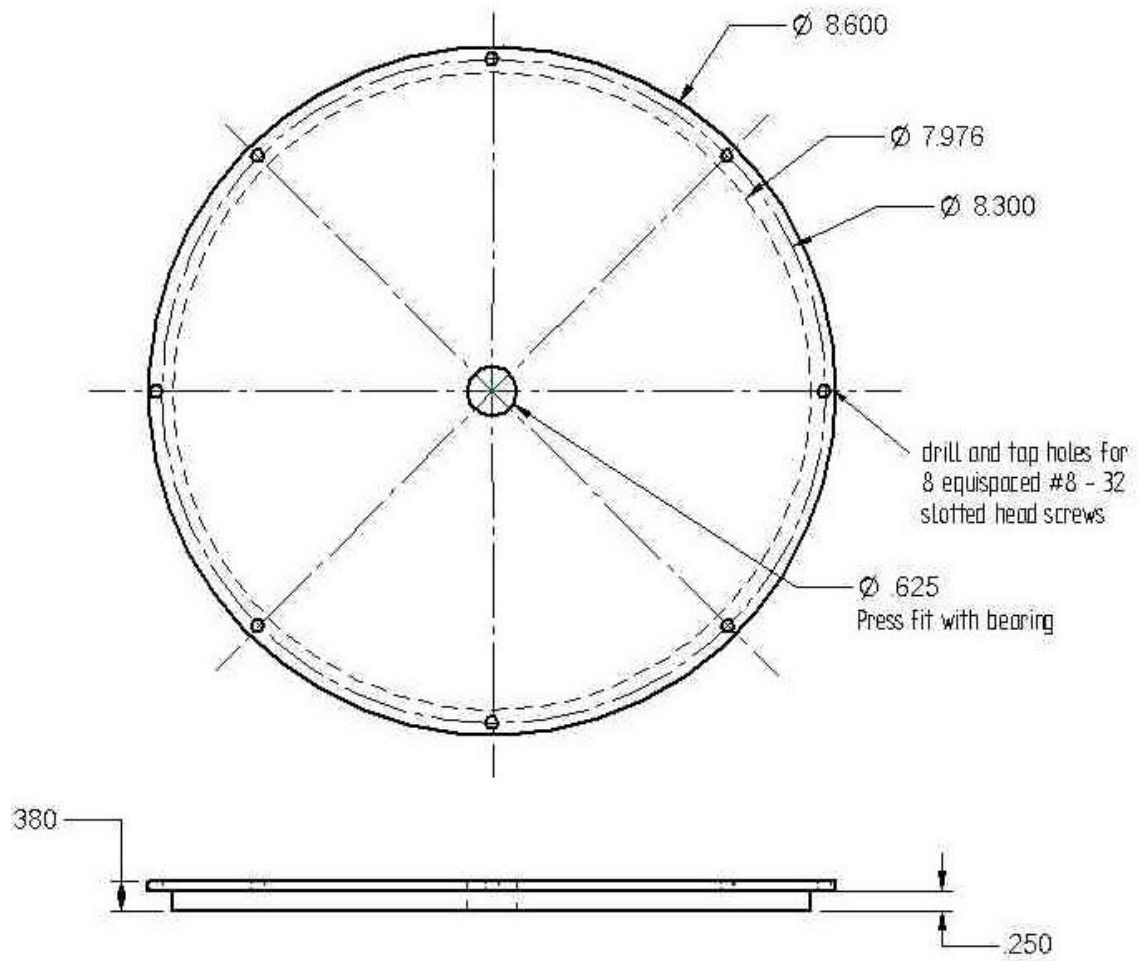
Figure A.2: AISI 1018 magnetic steel top plate
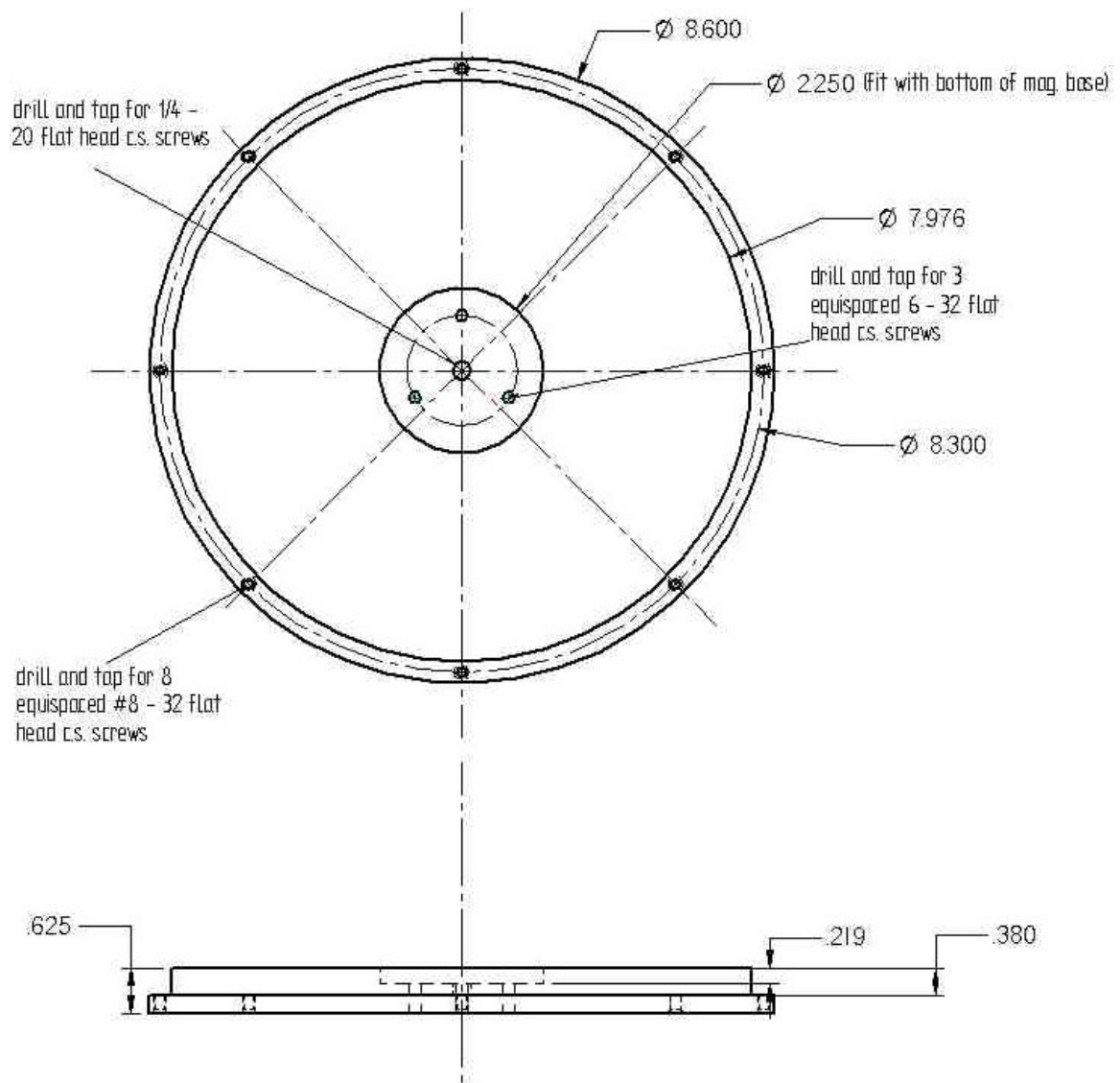
Figure A.3: AISI 1018 magnetic steel bottom plate
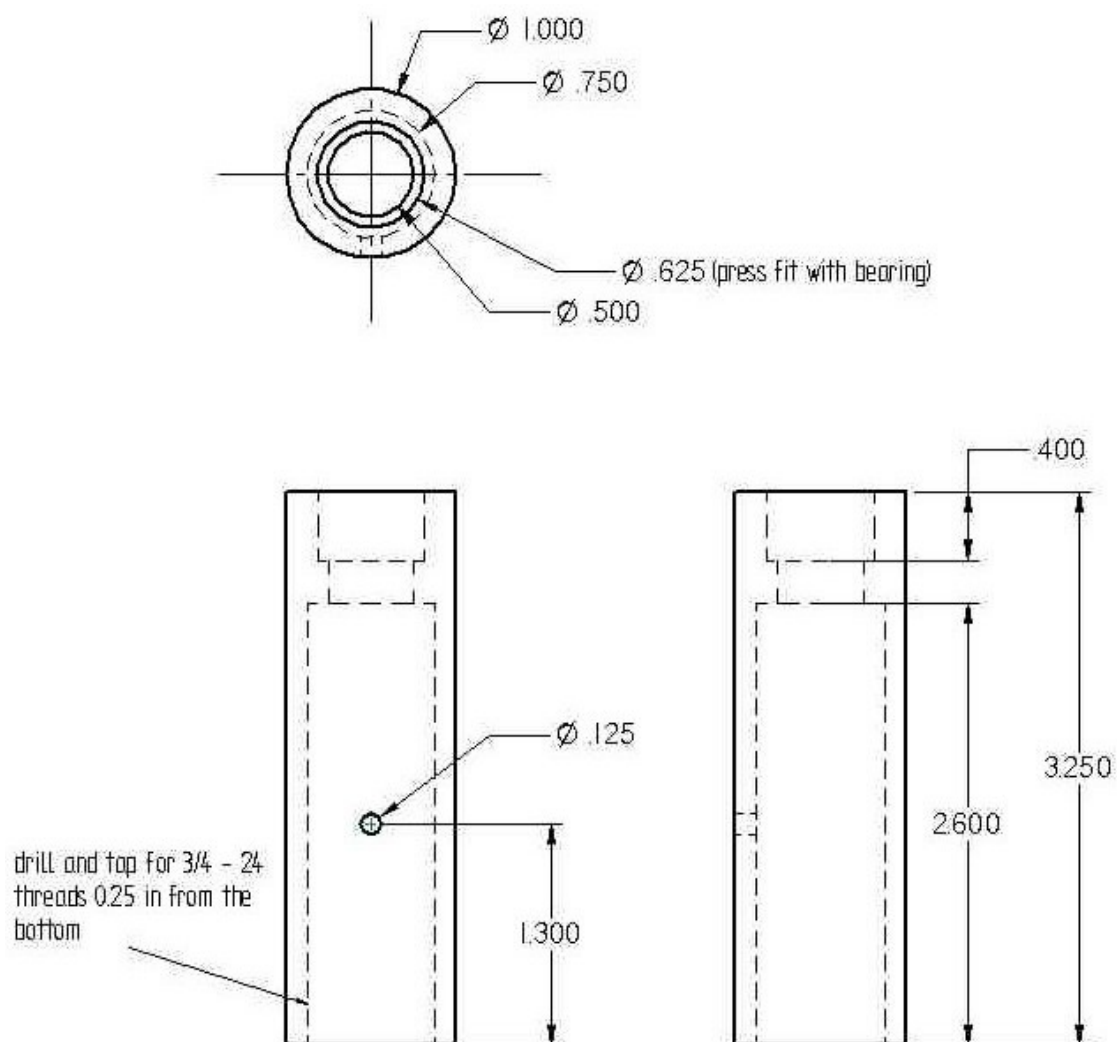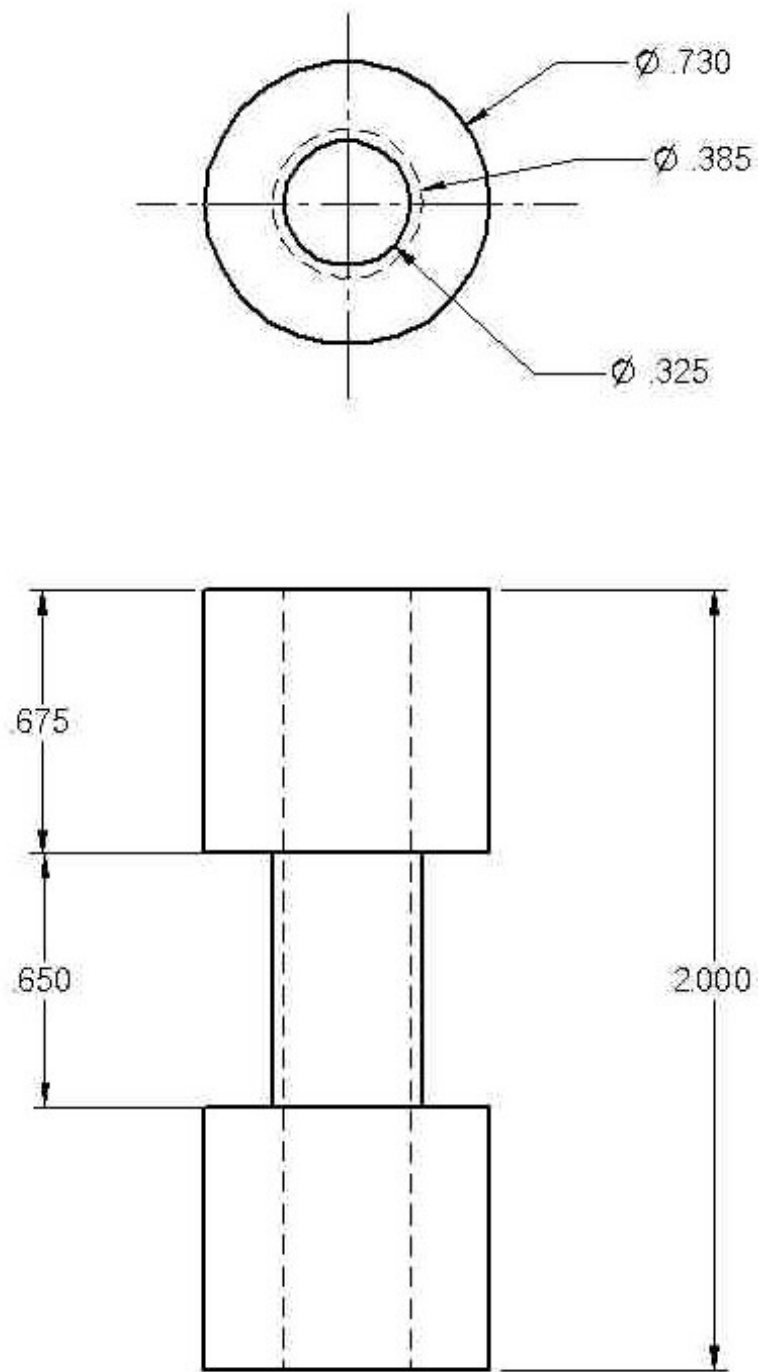
Figure A.4: 303 stainless steel sample housing
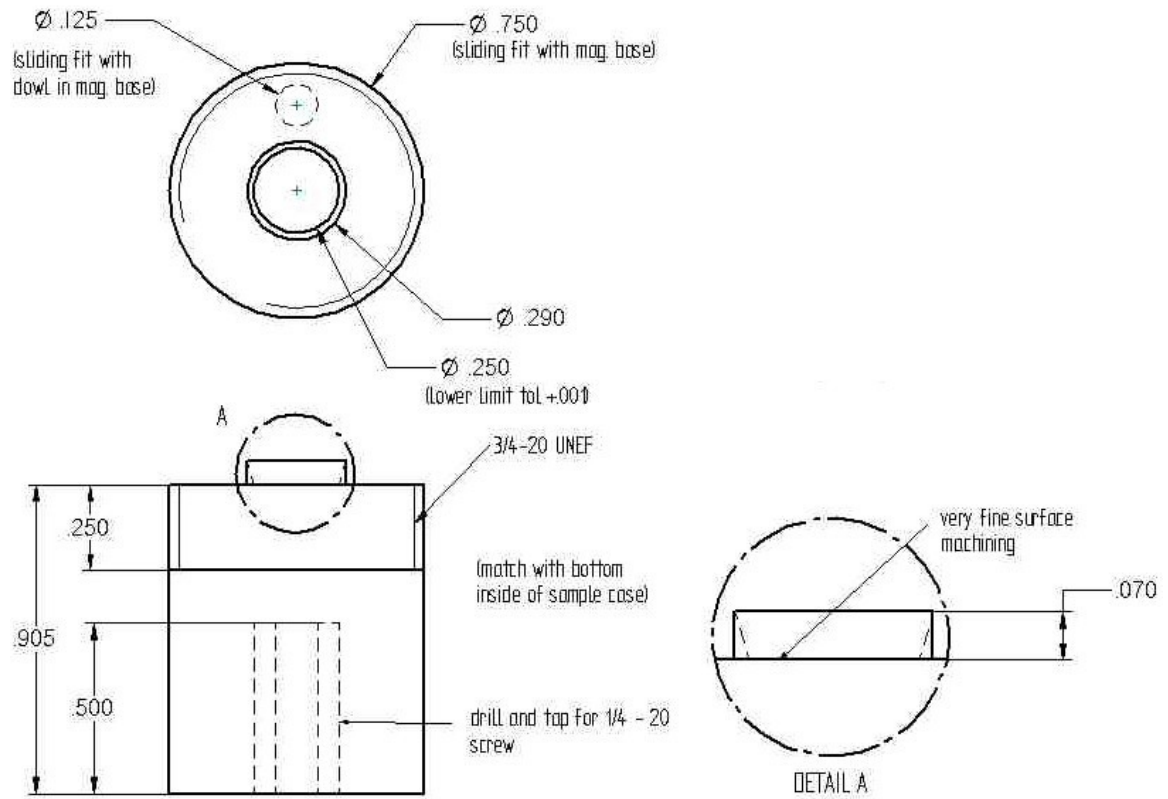
Figure A.5: Aluminum 6061-T6 sensing coil spool

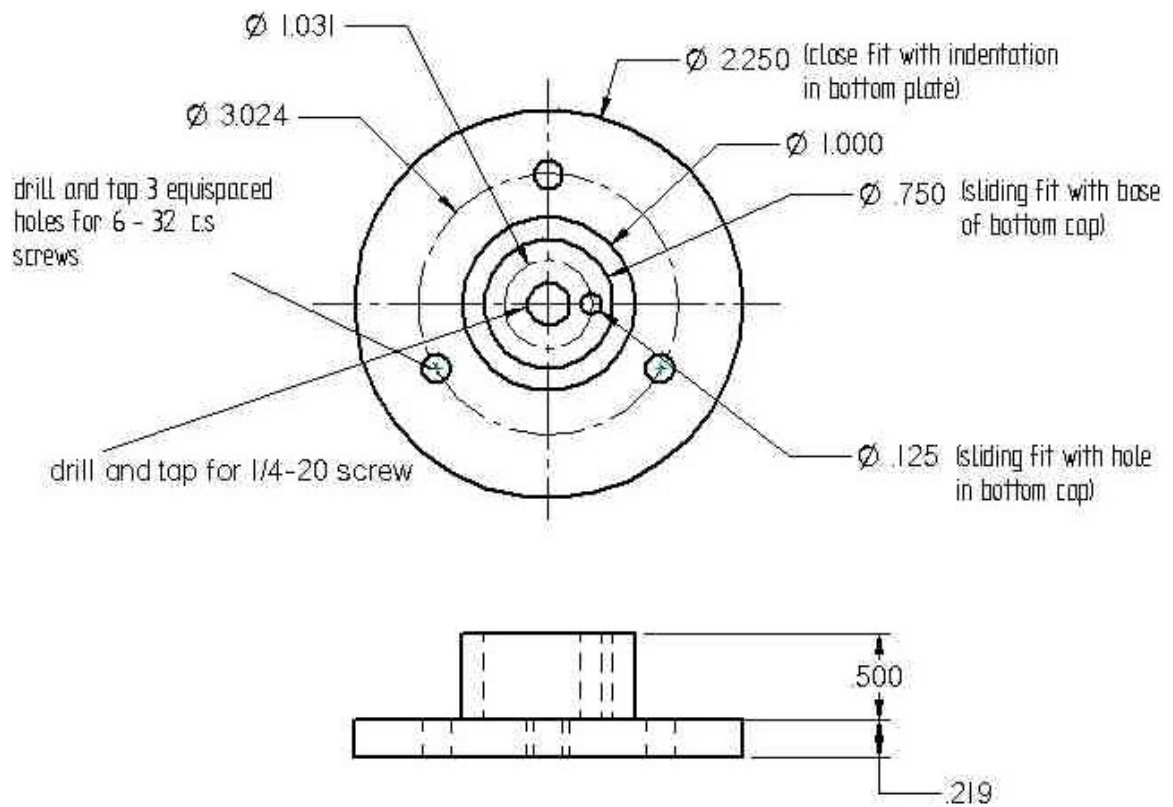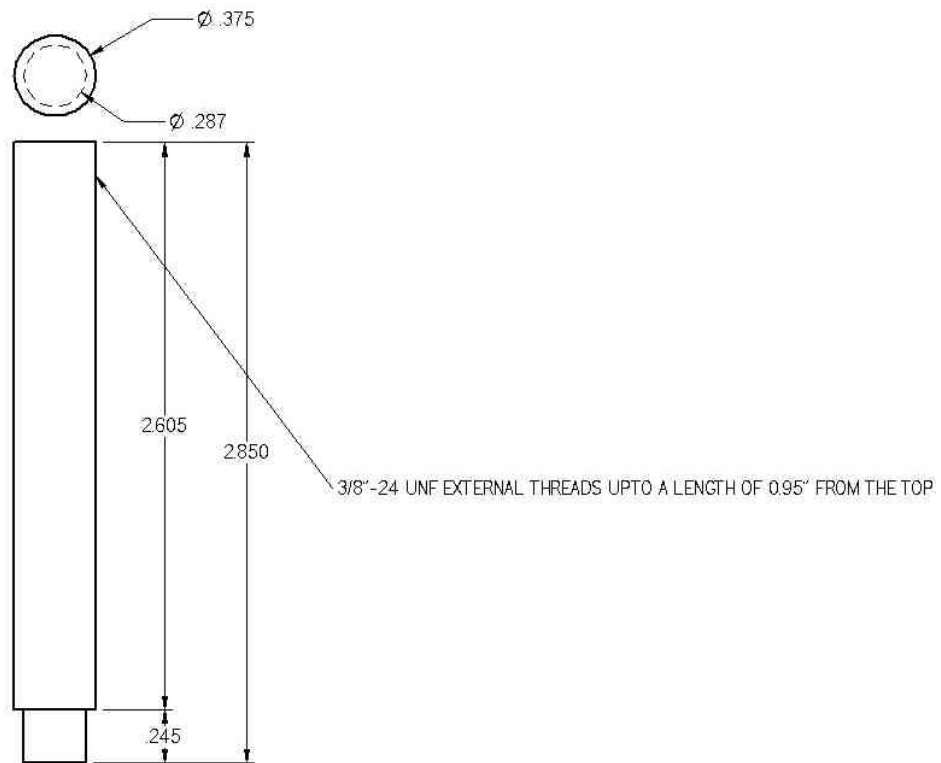Figure A.6: AISI 1144 stress proof magnetic steel bottom cap

Ø 1.031

Ø 2.250 (close fit with indentation in bottom plate)

Ø 3.024

Ø 1.000

drill and tap 3 equispaced holes for 6 - 32 c.s screws

Ø .750 (sliding fit with base of bottom cap)

drill and tap for 1/4-20 screw

Ø .125 (sliding fit with hole in bottom cap)

.500

.219

Figure A.7: AISI 1018 magnetic steel base

Figure A.8: AISI 1144 push rod

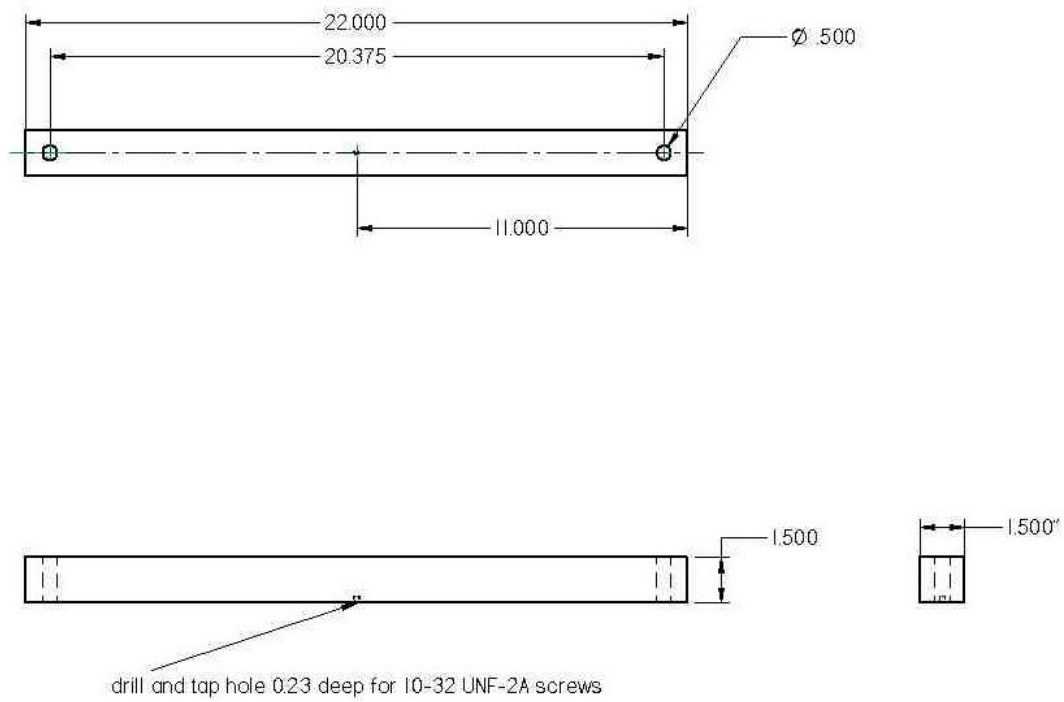# APPENDIX B

LOADING FIXTURE MACHINED COMPONENTS

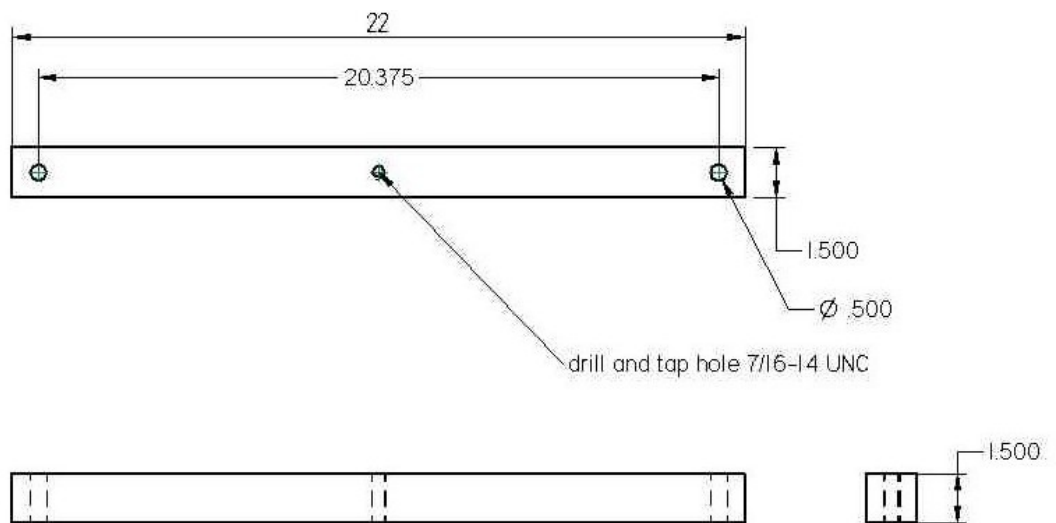Figure B.1: AISI 1018 upper loading beam

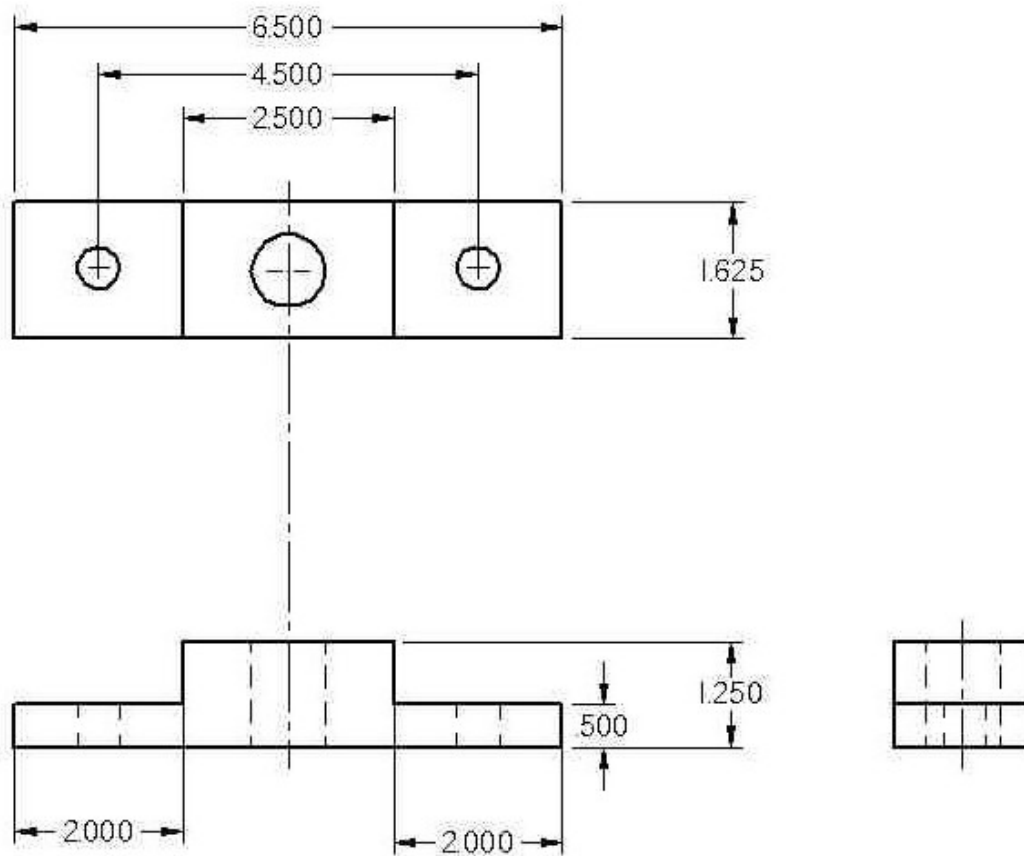Figure B.2: AISI 1018 lower loading beam
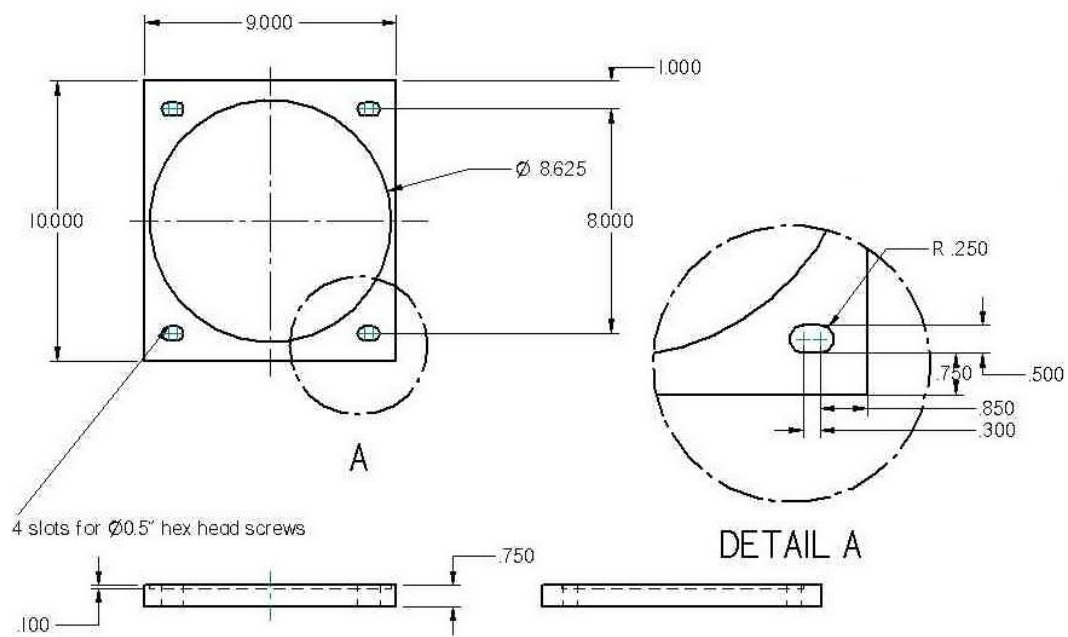
Figure B.3: AISI 1018 linear motion ball bearing housing
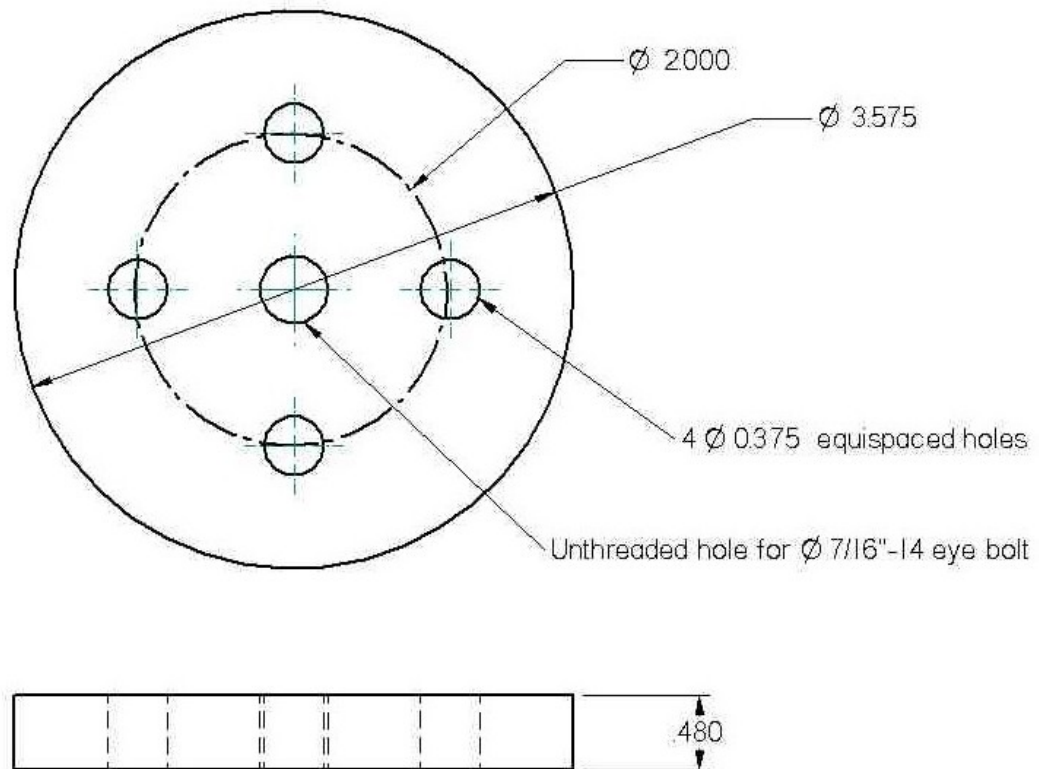
Figure B.4: Aluminum 6061-T6 transducer support plate

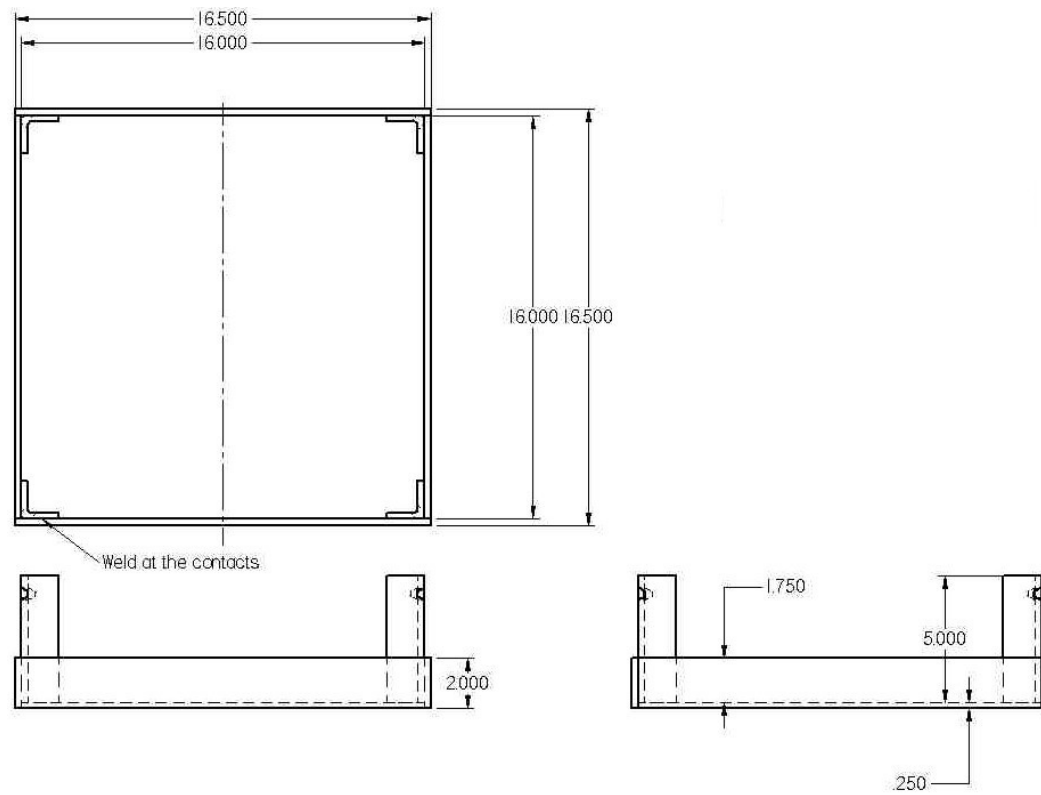Figure B.5: AISI 1018 load distributor plate

Figure B.6: AISI 1018 loading tray
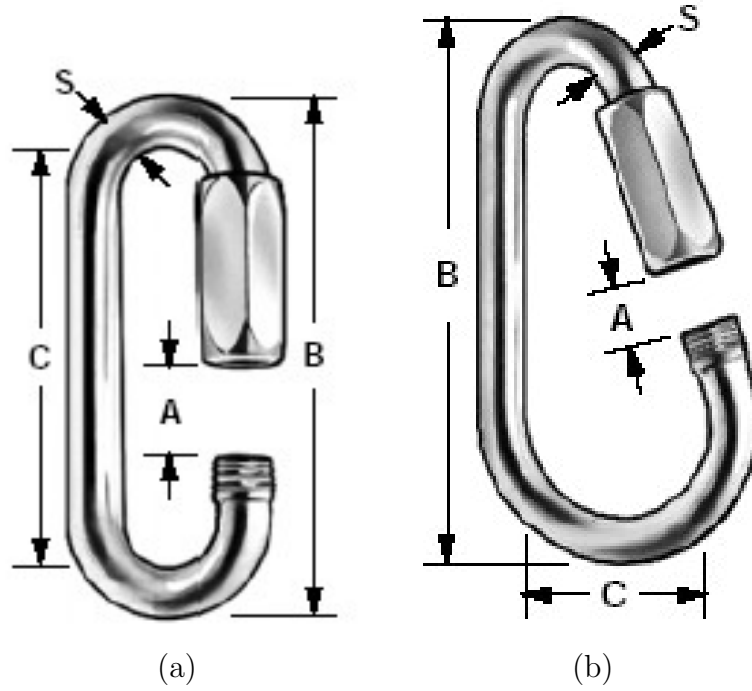
APPENDIX C

PURCHASED PARTS SPECIFICATIONS

Figure C.1: (a) Standard jaw threaded connector (b) Pear shaped threaded connector

Standard jaw				
S	A	B	C	Work load limit (lbs)
0.25"	0.28125"	2.75"	1.75"	880
0.3125"	0.375"	2.9375"	2.3125"	1760
0.375"	0.4375"	3.125"	2.4375"	2200
Pear shaped				
0.25"	0.5625"	3.1875"	0.8125"	440

Table C.1: Size and work load limit of the threaded connectors used

Span In	Max Allowable Uniform Load Lbs	Defl. at Uniform Load In	Uniform Loading at Deflection		
			Span/180 Lbs	Span/240 Lbs	Span/360 Lbs
24	1,690	0.06	1,690	1,690	1,690
36	1,130	0.13	1,130	1,130	900
48	850	0.22	850	760	510
60	680	0.35	650	490	320
72	560	0.50	450	340	220
84	480	0.68	330	250	170
96	420	0.89	250	190	130
108	380	1.13	200	150	100
120	340	1.40	160	120	80
144	280	2.01	110	80	60
168	240	2.74	80	60	40
192	210	3.57	60	50	NR
216	190	4.52	50	40	NR
240	170	5.58	40	NR	NR

Table C.2: Beam loading data for P1000 channel

Unbraced Height In	Maximum Allowable Load at Slot Face Lbs	Maximum Column Load Applied at C.G.			
		K = 0.65 Lbs	K = 0.80 Lbs	K = 1.0 Lbs	K = 1.2 Lbs
24	3,450	10,750	9,900	8,770	7,730
36	3,050	8,910	7,730	6,370	5,280
48	2,660	7,250	5,980	4,660	3,770
60	2,290	5,890	4,660	3,600	2,940
72	2,000	4,800	3,770	2,940	2,380
84	1,760	4,010	3,170	2,460	1,970
96	1,570	3,450	2,730	2,090	1,650
108	1,410	3,020	2,380	1,800	**
120	1,270	2,680	2,090	**	**

Table C.3: Column loading data for P1000 channel

Span mm	Max Allowable Uniform Load kg	Defl. at Uniform Load mm	Uniform Loading at Deflection		
			Span/180 kg	Span/240 kg	Span/360 kg
600	595	2	595	595	595
750	476	3	476	476	396
1,000	357	4	357	334	223
1,250	286	7	285	214	143
1,500	238	10	198	149	99
1,750	204	14	146	109	73
2,000	179	18	111	84	56
2,500	143	28	71	54	36
3,000	119	40	50	37	25
3,500	102	55	36	27	18
4,000	89	71	28	21	14
4,500	79	90	22	17	NR
5,000	71	111	18	NR	NR
6,000	60	160	NR	NR	NR

Table C.4: Beam loading data for P3000 channel

Unbraced Height mm	Maximum Allowable Load at Slot Face kg	Maximum Column Load Applied at C.G.			
		K = 0.65 kg	K = 0.80 kg	K = 1.0 kg	K = 1.2 kg
600	1,397	4,464	4,151	3,746	3,377
750	1,322	4,125	3,746	3,291	2,900
1,000	1,194	3,588	3,154	2,671	2,272
1,250	1,073	3,121	2,671	2,183	1,785
1,500	961	2,726	2,272	1,785	1,443
1,750	857	2,389	1,930	1,492	1,137
2,000	766	2,097	1,658	1,253	870
2,500	616	1,628	1,253	**	**
2,750	543	1,455	1,036	**	**

Table C.5: Column loading data for P3000 channel

APPENDIX D

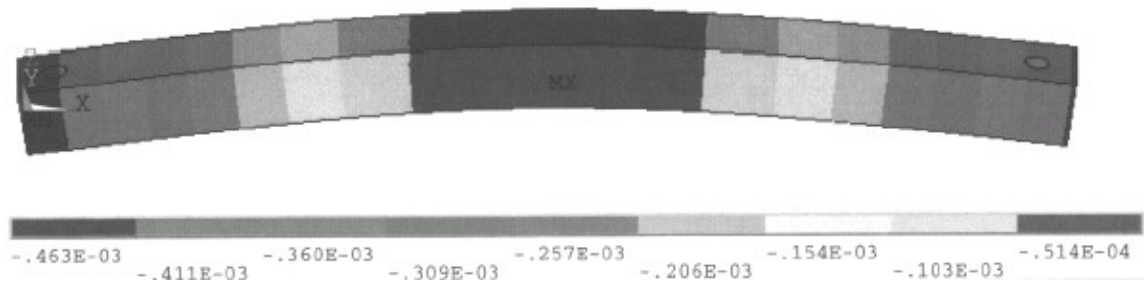# FEM ANALYSIS OF FIXTURE PARTS

Figure D.1: Upper rectangular loading beam vertical deflection.
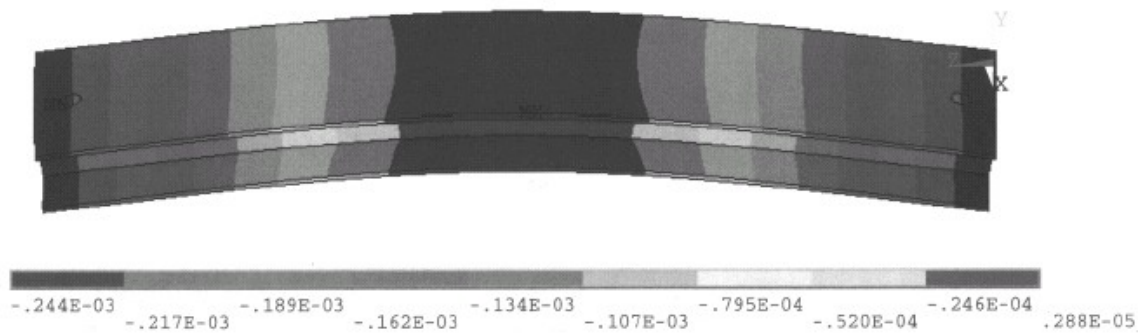

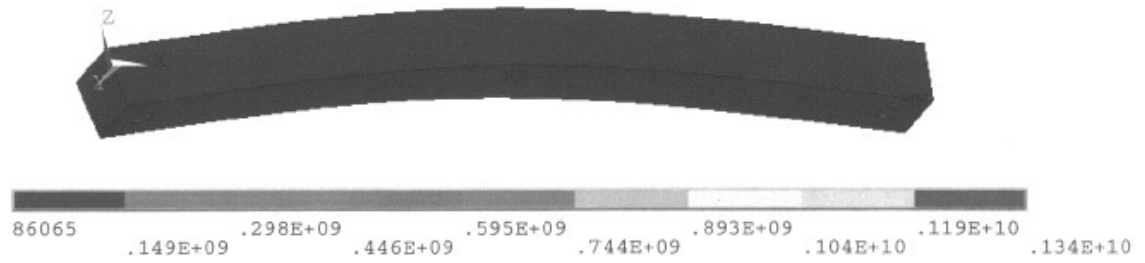Figure D.2: Upper loading beam (with C channels) vertical deflection.

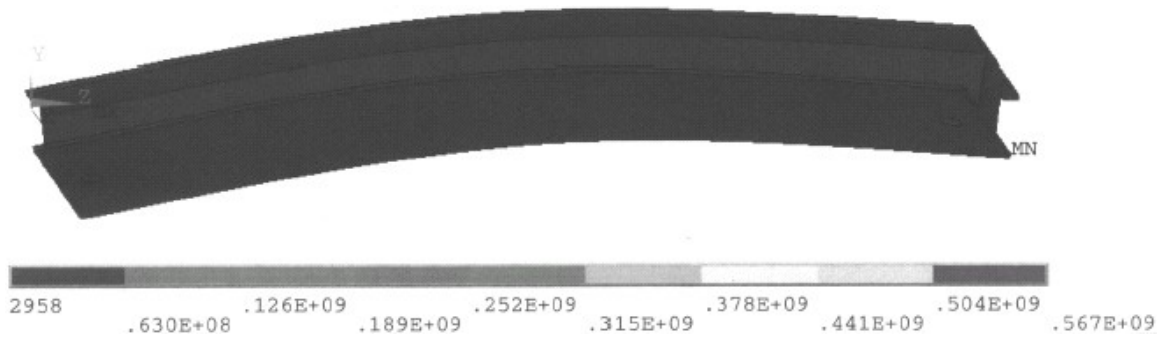Figure D.3: Upper rectangular loading beam average Von-Mises stress level.

Figure D.4: Upper loading beam (with C-channels) average Von-Mises stress level.
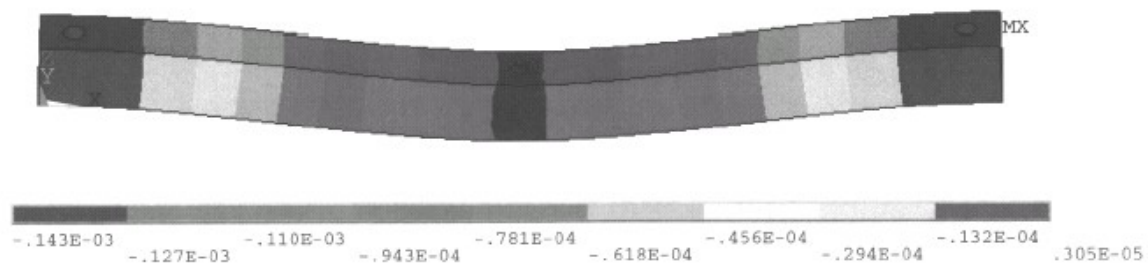
166

Figure D.5: Lower rectangular loading beam vertical deflection.
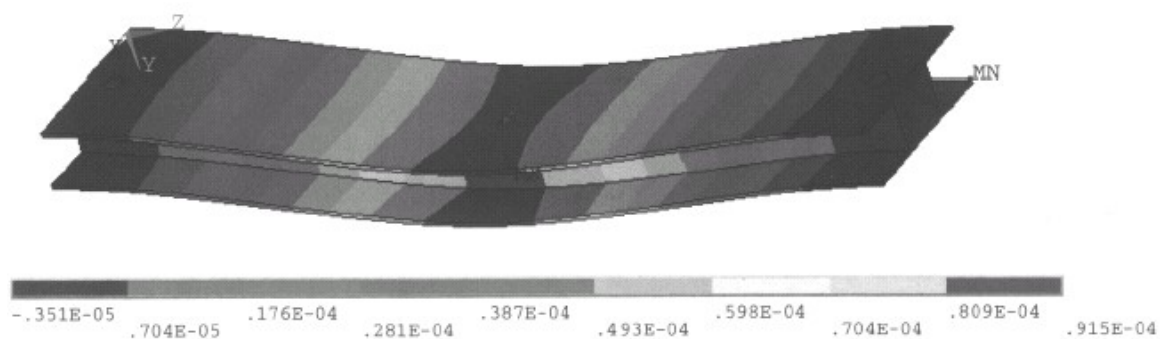

Figure D.6: Lower loading beam (with C channels) vertical deflection.
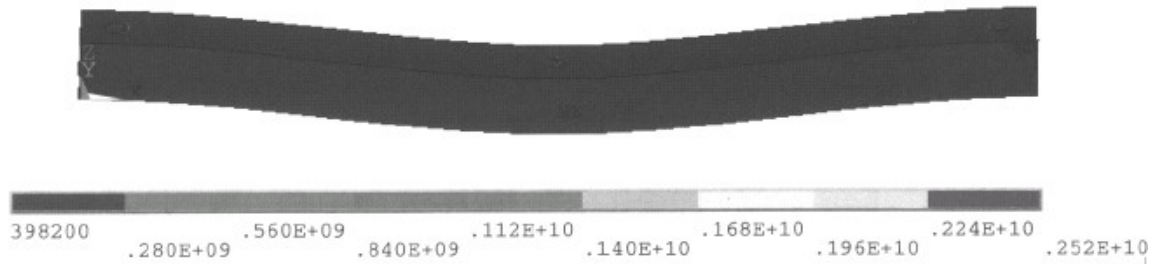
167

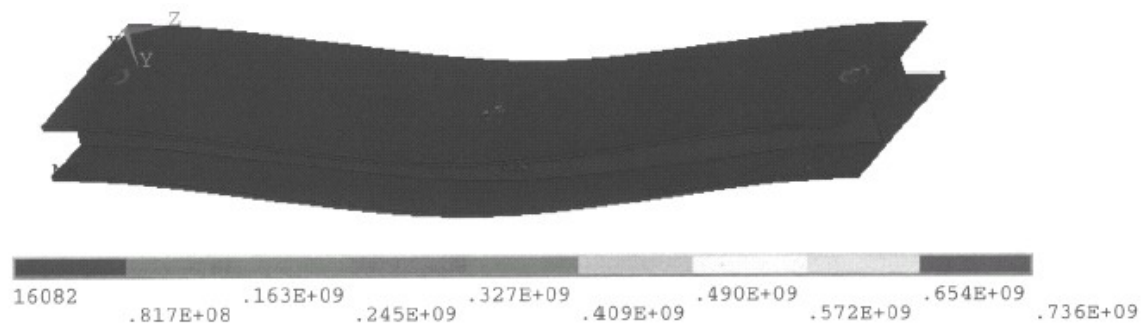Figure D.7: Lower rectangular loading beam average Von-Mises stress level.

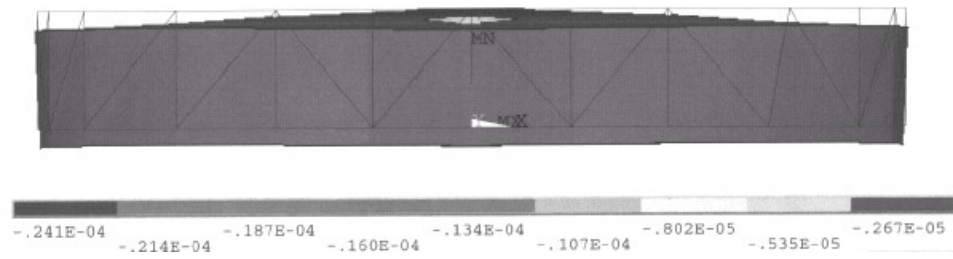Figure D.8: Lower loading beam (with C channels) average Von-Mises stress level.

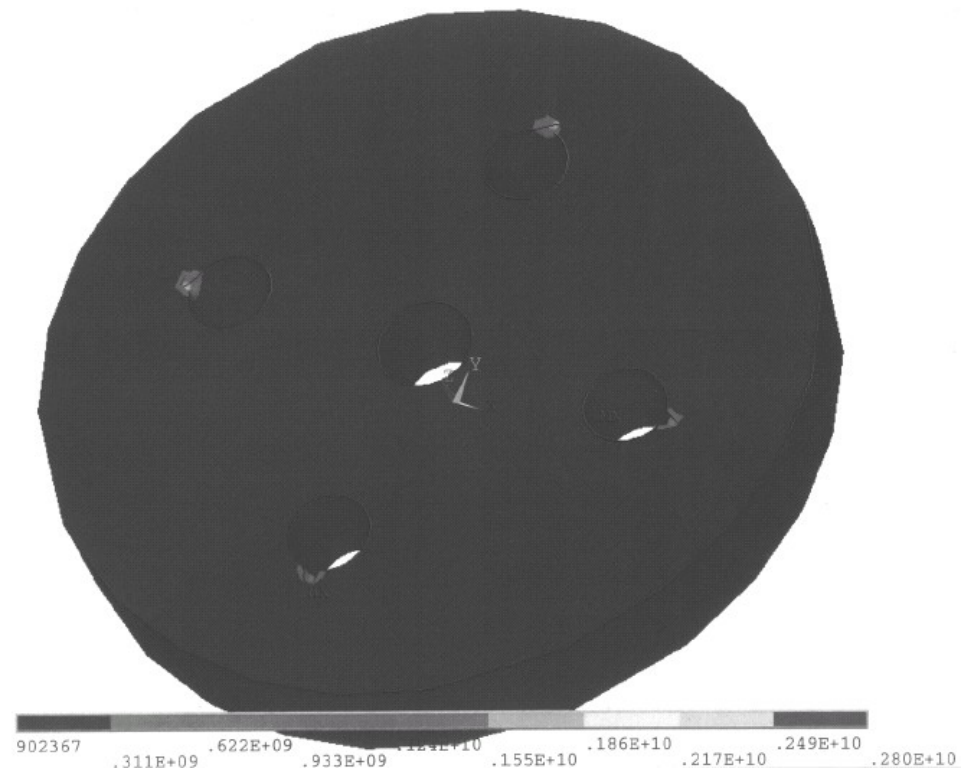Figure D.9: Load distributor vertical deflection.

Figure D.10: Load distributor average Von-Mises stress level.

BIBLIOGRAPHY

[1] Richard M. Bozorth. *Ferromagnetism*. D. Van Nostrand Company, Inc, 1951.

[2] Walter G. Cady. *Piezoelectricity*. McGraw-Hill, 1946.

[3] A.E. Clark and M. Wun-Fogle. "Modern magnetostrictive materials- classical and non-classical alloys". In *Proc. SPIE*, volume 4699, pages 421–436, 2002.

[4] Marcelo J. Dapino. *"Nonlinear and hysteretic magnetomechanical model for magnetostrictive transducers"*. PhD thesis, Iowa State University, 1999.

[5] L.E. Faidley, M.J. Dapino, G.N. Washington, R. Smith, and T.A. Lograsso. "Analytical and experimental issues in Ni-Mn-Ga transducers". In *Proc. SPIE*, 2003.

[6] C.P. Henry, J. Feuchtwagner, D. Bono, R.C. O'Handley, and S.M. Allen. "AC magnetic field-induced strain of single crystal Ni-Mn-Ga". In *Proc. SPIE*, volume 4699, pages 164–171, 2002.

[7] B. Jaffe, W.R. Cook, and H. Jaffe. *Piezoelectric Ceramics*. Academic Press, 1971.

[8] D. Jiles. *Introduction to Magnetism and Magnetic Materials*. Chapman and Hall, First edition, 1995.

[9] D. Jiles. "Theory of the magnetomechanical effect". *Journal of Physics D (Appl. Phys.)*, 28:1537–1546, 1995.

[10] X. Jin, M. Marioni, D. Bono, S.M. Allen, and R.C. O'Handley. "Empirical mapping of Ni-Mn-Ga properties with composition and valence electron concentration". *J. Appl. Phys.*, 91(10):8222–8224, May 2002.

[11] A.A. Likhachev, A. Sozinov, and K. Ullakko. "Influence of external stress on the reversibility of magnetic-field-controlled shape memory effect in Ni-Mn-Ga". In *Proc. SPIE*, volume 4333, pages 197–206, 2002.

[12] A.A. Likhachev and K. Ullakko. "Magnetic-field-controlled twin boundaries motion and giant magneto-mechanical effects in Ni-Mn-Ga shape memory alloy". *Physics Letters A*, 275:142–151, October 2000.

[13] A.A. Likhachev and K. Ullakko. "Quantitative model of large magnetostrain effect in ferromagnetic shape memory alloys". *Eur. Phys. J.*, B14:263–267, 2000.

[14] D.B. Montgomery. *Solenoid Magnet Design*. Robert Krieger, First edition, 1980.

[15] S.J. Murray, M. Marioni, S.M. Allen, R.C. O'Handley, and T.A. Lograsso. "6% magnetic field-induced strain by twin boundary motion in ferromagnetic Ni-Mn-Ga". *Appl. Phy. Lett.*, 77(6):886–888, August 2000.

[16] Robert L. Norton. *Machine Design: An Integrated Approach*. Prentice Hall, Second edition, 1998.

[17] R.C. O'Handley. "Model for strain and magnetization in magnetic shape memory alloys". *Journal of applied physics*, 83(6):3263–3270, March 1998.

[18] R.C. O'Handley, S.J. Murray, M. Marioni, H. Nembach, and S.M. Allen. "Phenomenology of giant magnetic-field-induced strain in ferromagnetic shape memory materials (invited)". *J. Appl. Phys.*, 87(9):4712–4717, May 2000.

[19] V.K. Pecharsky and K.A. Gschneider Jr. "Giant magnetocaloric effect in $Gd_5Si_2Ge_2$". *Phys. Rev. Lett.*, 78(23):4494–4497, June 1997.

[20] C.O. Smith. *The Science of Engineering Materials*. Prentice-Hall, Third edition, 1986.

[21] A. Sozinov, A.A. Likhachev, N. Lanska, and K. Ullakko. "Giant magnetic-field-induced strain in Ni-Mn-Ga seven layered martensitic phase". *Appl. Phys. Lett.*, 80(10):1746–1748, March 2002.

[22] A. Sozinov, A.A. Likhachev, and K. Ullakko. "Crystal structures and magnetic anisotropy properties of Ni-Mn-Ga martensitic phases with giant magnetic field-induced strain". *IEEE Transactions on Magnetics*, 38(5):2814–2816, September 2002.